Probing the IGM with the Lyman-Alpha Forest through Cosmic Time

Fahad Nasir



Thesis submitted to the University of Nottingham
for the degree of Doctor of Philosophy, November 2017

"The Universe is very, very big. It also loves a paradox. For example, it has some extremely strict rules. Rule number one: Nothing lasts forever. Not you or your family or your house or your planet or the sun. It is an absolute rule. Therefore when someone says that their love will never die, it means that their love is not real, for everything that is real dies. Rule number two: Everything lasts forever."

– Craig Ferguson

Supervisors:	Dr. James Bolton
	Prof. Frazer Pearce
Examiners:	Prof. Romeel Dave
	Dr. Meghan Gray

Abstract

The Lyα forest is a series of absorption lines seen in quasar spectra and is a powerful tool for probing the thermal state of the intergalactic medium (IGM) across a wide redshift range. At intermediate redshifts ($2 \lesssim z \lesssim 5$), the statistical properties of the Lyα forest predicted by recent hydrodynamical simulations are in good agreement with a range of spectroscopic data. However, at lower and higher redshifts this is still not the case. Some of the key questions still challenging our understanding at low redshifts are the nature of absorbers, the evolution of the ultraviolet background and the impact of feedback from supernovae and active galactic nuclei (AGN). Furthermore, as a range of reionsation models remain unconstrained and the precise timing of reionsation remains elusive, high redshift Lyα forest data can provide valuable insight due to its sensitivity to the post-reionsation thermal properties of the IGM.

At low redshift, this investigation focuses on understanding the effect of different feedback prescriptions on the properties of the Lyα forest using simulations from the Sherwood simulation suite. The simulations incorporate three different prescriptions for treating cold dense gas and galactic feedback from supernovae and AGN. These implementations have only a small effect on the properties of the Lyα column density distribution function (CDDF) and Lyα line velocity width distribution. Therefore, feedback does not solve the discrepancy between the *Cosmic Origins Spectrograph* (COS) observations of the CDDF at $z \simeq 0.1$ for high column density systems ($N_{\rm HI} > 10^{14}\,{\rm cm}^{-2}$), as well as the line width distribution, which has lines broader then the simulation data. Some of the possible solutions may be feedback that ejects more overdense gas into the IGM, an increase in the temperature of the overdense gas (which is rather fine-tuned so that the gas is able to still contribute to the Lyα forest), or an unresolved turbulent in the IGM.

The low redshift Lyα forest investigation is concluded by performing a series of numerical convergence tests on the quantities most widely employed in absorption line studies at low redshift. The mass resolution of the simulations can significantly impact on the estimated line velocity widths, by overestimating line widths for low mass resolution runs. By contrast, the Lyα CDDF is quite well converged for low column density absorbers.

At higher redshifts, a feasibility analysis to constrain the thermal history of the IGM using cosmological hydrodynamical simulations of the Lyα forest is performed. This problem is approached by utilising the Lyα forest transmitted flux power spectrum at $z \sim 5$. The integrated heating during reionsation has a measurable impact on the power spectrum. The integrated heating is parameterised using the cumulative energy per proton deposited into a gas parcel at the mean background density. A Markov Chain Monte Carlo approach is used to recover the cumulative energy per proton with a statistical uncertainty of ~ 20 per cent (at 68 per cent confidence interval), by making assumptions consistent with current observational data sets. However, systematics may increase the uncertainty to ~ 30 per cent at these redshifts. This method can distinguish between early ($z = 12$) and late ($z = 7$) reionisation in the simulations.

Finally, to expand on this investigation, the first constraints on the cumulative energy per proton using recent Lyα flux power spectrum measurements at high redshift are obtained. A consistent picture of galaxy driven reionsation with reionsation occurring at $z \sim 9$ is found.

Published work

Much of the work in this thesis is presented in the following two papers.

I **Nasir F.**, Bolton J. S., Viel M., Kim T.-S., Haehnelt M. G., Puchwein E., Sijacki D., *The effect of stellar and AGN feedback on the low redshift Lyman-α forest in the Sherwood simulation suite*, 2017. MNRAS, 471, 1056.

II **Nasir F.**, Bolton J. S., Becker G. D., *Inferring the IGM thermal history during reionization with the Lyman-α forest power spectrum at redshift $z \simeq 5$*, 2016. MNRAS, 463, 2335.

III Viel M., Haehnelt M. G., Bolton J. S., Kim T.-S., Puchwein E., **Nasir F.**,Wakker B. P., *Diagnosing galactic feedback with line broadening in the low-redshift Lyman-α forest*, 2017. MNRAS, 467, L86.

Paper I contains the work presented in Chapter 2 and parts in Chapter 3. Paper II contains the work presented in Chapter 4. Paper III is a co-authored paper and is not presented in this thesis.

Acknowledgments

I would like to thank my supervisor, Jamie Bolton, for the continuous support through all these years. I am extremely lucky to have such a great mentor who responded to my queries as quickly and effectively as possible. Thanks again for your support, encouragement and patience. I also want to thank Prof. Frazer Pearce as being my co-supervisor for insightful discussions and providing me the support I needed. I also like to thank all the staff at School of Physics and Astronomy at University of Nottingham.

I must express my gratitude for my lovely wife Gulzaib and my son Saim for the love, encouragement and delicious lunches. I would like to thank all my friends for the interesting discussions and small breaks from work when I needed them. I would like to express my special thanks to Finlay, Jake, Miguel and Mehdi for proof reading with countless pages of complex concepts and giving me excellent feedback.

Finally, I would like to thank the University of Nottingham for funding this research by supporting me with a Vice-Chancellor's Scholarship and giving me the opportunities to attend conferences, meet experts and fantastic people all across the globe.

Contents

List of Figures **iv**

List of Tables **vii**

1 Introduction **1**

1.1 Cosmology and structure formation 1

1.2 Reionisation 3

1.3 The intergalactic medium 5

1.4 Probing the IGM - the Lyman-α forest 6

1.4.1 The Gunn-Peterson trough 8

1.5 Modelling the Lyman-α forest with cosmological simulations 12

1.6 The Lyα forest statistics 14

1.7 The Lyα forest at high redshifts, $z \gtrsim 5$ 19

1.8 The Lyα forest at low redshifts, $z \lesssim 2$ 20

1.9 Thesis overview 21

2 The effect of stellar and AGN feedback on the low redshift Lyman-α forest in the Sherwood simulation suite **22**

2.1 Introduction 22

2.2 Methodology 25

2.2.1 Hydrodynamical simulations 25

2.2.2 Mock Lyα forest spectra 28

2.3 Voigt profile analysis 30

2.3.1 The CDDF 32

2.3.2 The velocity width distribution 35

2.3.3 The evolution of number density of absorbers 39

2.4 Identifying the gas responsible for low redshift Lyα forest absorbers . 40

2.5 Conclusions 45

3 Resolving the low redshift Lyα forest **47**

3.1 Voigt profile fitting 48

3.2 Transmitted flux statistics 50

3.3 Temperature and slope of $T - \Delta$ relation 52

3.4 Conclusions 55

4 Inferring the IGM thermal history during reionisation with the Lyman-α forest power spectrum at redshift $z \simeq 5$ **56**

4.1 Introduction 56

4.2 Modelling the Lyα forest at $z \simeq 5$ 60

4.2.1 Hydrodynamical simulations 60

4.2.2 The broadening of Lyα forest absorbers 63

4.2.3 The line of sight Lyα forest power spectrum 65

4.3 From flux power spectrum to thermal history 69

4.4 Inferring the thermal history during reionisation 72

4.4.1 Markov Chain Monte Carlo analysis 72

4.4.2 Distinguishing between reionisation models with $P_{\rm F}(\rm k)$ . . . 76

4.4.3 Systematic uncertainties 77

4.5 Conclusions and discussion 80

5 First constraints on the integrated thermal history **83**

5.1 Introduction 83

5.2 Observational data 84

5.3 Methodology 84

5.3.1 Hydrodynamical simulations 84

5.3.2 The MCMC 88

5.3.3 Improvements in the method 89

5.4 Results 93

5.5 Conclusions 97

6 Summary and future work **98**

6.1 The impact of feedback on the low redshift Lyα forest 98

6.2 Constraints on the integrated thermal history of IGM with the high redshift Lyα forest 99

6.3 Outlook 100

6.3.1 High redshift quasars 100

6.3.2 21 cm radiation 101
6.3.3 Ultraviolet spectroscopy 102
6.3.4 Radiative transfer in hydrodynamical simulations 102
6.3.5 The ionising background at low redshifts 102
6.3.6 Interplay between circumgalactic medium and IGM 103
6.3.7 Warm dark matter models 103
6.3.8 Future Work 104

Bibliography **106**

List of Figures

1.1 The temperature map of the cosmic microwave background 2

1.2 A large cosmological hydrodynamical simulation in a $100h^{-1}\mathrm{cMpc}$ box from the Illustris TNG project 4

1.3 High resolution spectrum of a quasar at $z = 3.62$, and simulated line-of-sight spectrum predicted by the hydrodynamical simulations 7

1.4 The detection of first Gunn-Peterson trough in the spectrum of a quasar at redshift $z = 6.28$ 9

1.5 The spectrum of quasar at $z = 3.62$ and the simulated spectrum from hydrodynamical simulations 12

1.6 The Lyα forest transmitted flux PDF at $z = 3$. 15

1.7 A comparison of transmitted flux power spectrum measurements . . . 16

1.8 A comparison between the H I column density distribution predicted by the OWLS simulations and observations 17

1.9 The Lyα velocity width distribution at $z = 2.1$, from hydrodynamical simulations with different galactic feedback prescriptions 18

2.1 The redshift evolution of the volume weighted temperature at mean density, temperature at the characteristic density probed by the Lyα forest and slope of temperature density relation 27

2.2 The redshift evolution of the effective optical depth and H I photoionsation rates overlaid with observations 29

2.3 The H I column density distribution function overlaid with observations at $z = 0.1$ 32

2.4 The Lyα forest column density distribution function with different feedback prescriptions 33

2.5 The Lyα forest velocity width distribution overlaid with observations at $z = 0.1$ 36

2.6 The Lyα forest velocity width distribution with different feedback prescriptions 36

2.7 The redshift evolution in the number of Lyα absorbers per unit redshift 37

2.8 *Top:* The optical depth weighted normalised gas density against the H I column density. *Bottom:* The optical depth weighted gas temperature against the Lyα velocity widths. 42

3.1 The Lyα forest CDDF convergence with mass resolution at $z = 0.1,\ 1,$ and 1.6 48

3.2 The Lyα forest CDDF convergence with box size at $z = 0.1,\ 1,$ and 1.6 49

3.3 The Lyα velocity width distributions convergence with mass resolution at $z = 0.1,\ 1,$ and 1.6 49

3.4 The Lyα velocity width distributions convergence with box size at $z = 0.1,\ 1,$ and 1.6 50

3.5 The redshift evolution of effective optical depth: convergence with mass resolution and box size 51

3.6 The PDF of the Lyα transmitted flux convergence with mass resolution at $z = 0.1,\ 1,$ and 1.6 51

3.7 The PDF of Lyα transmitted flux convergence with box size at $z = 0.1,\ 1,$ and 1.6 52

3.8 The power spectrum of the transmitted flux convergence with box size at $z = 0.1,\ 1,$ and 1.6 52

3.9 The power spectrum of the transmitted flux convergence with mass resolution at $z = 0.1,\ 1$ and 1.6 53

3.10 The convergence with box size and mass resolution of temperature at mean density and the slope of the temperature-density relation 53

4.1 The thermal history of simulations 60

4.2 Contour plot of the optical depth weighted gas overdensity, against transmitted flux 64

4.3 The transmitted flux power spectrum for native models, only pressure smoothing and only thermal broadening effects 66

4.4 *Top left:* The average of the Lyα forest power spectrum (at pressure smoothing scales) against gas density power spectrum. *Top right:* The cumulative energy per proton against the density power spectrum. *Bottom:* The average flux power spectrum (at pressure smoothing scales) against the cumulative energy per proton 68

4.5 The two dimensional probability distributions for the parameters for the mock observations of D15 model 73

4.6 The one dimensional marginalised posterior distributions for u_0 obtained from mock observations of the Tz12, Tz9 and Tz7 models . . . 74

4.7 The two dimensional probability distributions for the parameters for the mock observations of Tz9HOT model 74

4.8 The Lyα flux power spectrum at $z = 4.9,\ 4$ and 3 for Tz12 and Tz7 models 80

5.1 The thermal histories for the simulations, the logarithm of the temperature at mean density and the cumulative energy per proton deposited in a gas parcel at mean density 85

5.2 A comparison of the logarithmic projected gas density relative to the mean density between two models 86

5.3 The transmitted Lyα flux power spectrum convergence with mass resolution at $z = 4.2,\ 4.6,\ 5,$ and 5.4 90

5.4 The transmitted Lyα flux power spectrum convergence with box size at $z = 4.2,\ 4.6,\ 5,$ and 5.4 91

5.5 The transmitted Lyα flux power spectrum for different quasar contribution to UVB at $z = 4.2,\ 4.6,\ 5,$ and 5.4 92

5.6 The MCMC best fits for the observational flux power spectrum data points at $z = 4.2,\ 4.6,\ 5,$ and 5.4 95

5.7 The two dimensional probability distributions for the parameters for observational data at $z = 5$ 96

List of Tables

2.1 The subset of runs in the Sherwood simulations suite 25

2.2 A comparison of baryon phases in the simulations with different treatments for cold, dense gas and feedback 41

3.1 The subset of runs in the Sherwood simulations suite for numerical convergence 48

3.2 The numerical convergence of baryon phases in the simulations with different box size and mass resolution 54

4.1 A list of hydrodynamical simulations 61

4.2 Predicted constraints on $\log(\mathrm{T}_0)$ and u_0 obtained from mock observations for the realistic and optimistic data scenarios 78

5.1 The list of hydrodynamical simulations 87

5.2 Improved constraints on $\log(\mathrm{T}_0)$ and u_0 obtained for the power spectrum at $z = 4.2,\ 4.6,\ 5,$ and 5.4 94

Chapter 1

Introduction

1.1 Cosmology and structure formation

The standard cosmological model explains the formation of the Universe by establishing that sometime in the past, it was once in a very hot dense state and has been expanding and cooling ever since. This "Big Bang" model was suggested to explain some of the major scientific findings in the past century. Some of which include, measurements of the Cosmic Microwave Background (CMB) (Bennett *et al.*, 2013; Planck Collaboration *et al.*, 2016a), the abundance of light elements from primordial nucleosynthesis (Olive & Skillman, 2004), the accelerated expansion of the Universe as established from the luminosity-distance relationship of type Ia supernovae (Perlmutter *et al.*, 1999; Riess *et al.*, 2004; Astier *et al.*, 2006) and the clustering of galaxies as observed by modern large scale surveys (Tegmark *et al.*, 2004; Johnson *et al.*, 2014; van Uitert *et al.*, 2017).

To explain these findings the model assumes an expanding Universe which is homogeneous and isotropic on large scales (i.e. few hundreds of Mpc). The mass-energy content of the Universe is 71% dark energy, 24% dark matter and 4% baryonic matter (Planck Collaboration *et al.*, 2015). The most prevalent is dark energy, which is held responsible for the accelerating Universe but still poorly understood. The dark matter component is detected indirectly through its gravitational influence but has not been observed directly to date. The remaining baryonic content forms the observable Uni-

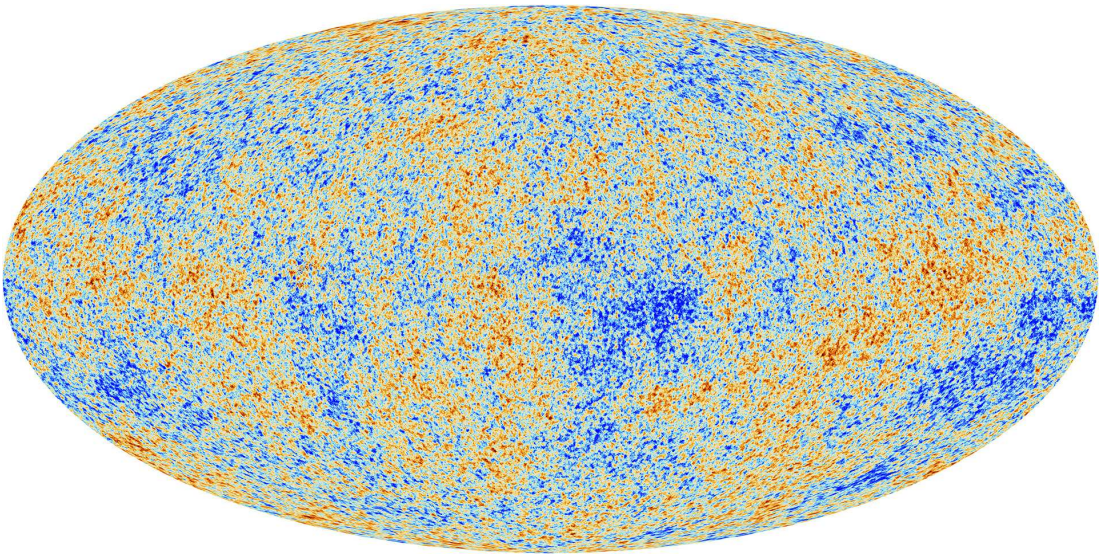


Figure 1.1: The temperature map of the cosmic microwave background as observed by Planck (Planck Collaboration *et al.*, 2016a). It shows temperature fluctuations that correspond to tiny differences in densities, when the Universe was 380,000 years old. These are the seeds for the structure observed later in the Universe. Credit: European space agency and the Planck collaboration. Image taken from `www.esa.int/spaceinimages/Images/2013/03/Planck_CMB`

verse as stars, galaxies and clusters and the gas in between them. The current paradigm for this cosmological model is referred to as ΛCDM. The Λ is Einstein's cosmological constant, a possible candidate for dark energy. Cold Dark Matter (CDM) is a version of dark matter which moves at non-relativistic speeds.

The current accelerated expansion of the Universe can be traced back to an initial hot and dense state. At this stage, the Universe inherited the seeds of quantum inhomogeneities amplified through a period of exponential expansion known as inflation (Guth, 1981). These seeds grew through gravitational instability and formed the large scale structures observed later on in the Universe.

In the hot early Universe, nuclei and electrons are not bound and photons constantly scatter off charged particles. However, as the temperatures and densities dropped due to continued expansion, protons and electrons began to form atoms. This is known as recombination and it happened at $z \sim 1100$. After this the neutral atoms cease to scatter off photons (except bound-bound and bound-free interactions) and they were free to travel without any hindrance until observed. This prevalent relic radiation permeates the whole Universe and is redshifted to microwave frequencies in the current Universe. The CMB shows a black body spectrum at a temperature of 2.72548 ± 0.00057K (Fixsen, 2009).

The CMB is extremely isotropic, but shows temperature fluctuations up to $\Delta T/T \sim 10^{-5}$ (Smoot *et al.*, 1992), giving us a glimpse of the density distribution of matter at the epoch of recombination. There are regions of the Universe which are overdense and regions which are underdense. The more dense regions accrete more matter, thus acquiring more mass and growing in a hierarchical manner (White & Rees, 1978). On the other hand, the underdense regions expand and become less dense. Thus, the Universe proceeds to build up matter in a hierarchical manner, by building small structures first and accreting those structures to build more massive structures. Numerical N-body simulations are an invaluable tool to follow this hierarchical growth (Springel *et al.*, 2005a).

The formation of structures by gravitational instability and hierarchical merging gives us an accurate description of the dark matter distribution. However, as baryons undergo radiative and dissipative processes, they fail to follow dark matter at smaller scales. This makes the accurate modelling of baryons in cosmological simulations quite challenging. At large scales, baryons collapse in dark matter halos and form stars, galaxies, quasars and galaxy clusters (see Figure 1.2). Recent hydrodynamical simulations help to visualize the structures formed in this hierarchical assembly (Vogelsberger *et al.*, 2014a; Schaye *et al.*, 2015). These luminous objects in turn produce large amounts of high energy photons that have sufficient energy to ionise the surrounding gas, that forms the intergalactic medium (IGM). This serves as a huge dilute reservoir of gas, accounting for most of the baryonic matter in the Universe. Understanding the IGM and its evolution is crucial to cosmology and for following the build-up of structures through cosmic time.

1.2 Reionisation

The hierarchical growth which triggered star formation consequently created the first sources of ultraviolet photons (Trenti & Stiavelli, 2009), which ionised the IGM we observe today. These sources ended the dark ages that existed since the epoch of recombination, by producing photons which have energies above 1 Ryd that are capable of ionising the neutral hydrogen in the IGM, resulting in H I reionsation (Rees, 2000).

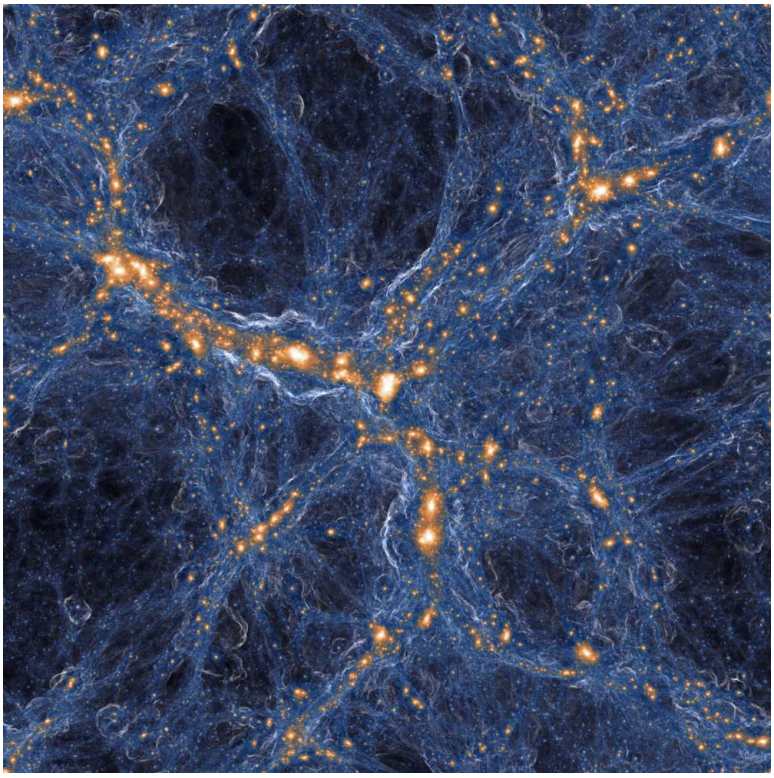


Figure 1.2: A large cosmological hydrodynamical simulation in a $100h^{-1}\mathrm{cMpc}$ box from the Illustris TNG project. A projection of the dark matter density with gravitationally collapsed structures is shown in orange, which are surrounded by successive shock surfaces (blue), showing their formation history. Credit: Illustris TNG team. Image taken from `www.tng-project.org/media`

Reionsation was an extended process. At first the sources start ionising the surrounding gas, forming ionised bubbles (Furlanetto, Zaldarriaga & Hernquist, 2004; Furlanetto & Oh, 2005). There might have been differences in the morphology of these H II bubbles due to the spectrum of ionising sources. Reionsation will be inhomogenous due to the distribution of bright sources and the clumpiness of gas (Becker *et al.*, 2015). Further in to the process of ionisation, the H II bubbles started to overlap eventually resulting in a uniform metagalactic ultraviolet background. Due to the clumpiness of gas, some dense gas pockets remained self shielded to the increasing ultraviolet background (the so-called Lyman-limit systems).

The uncertainty in the timing of reionisation is related to our lack of observations of the astrophysical sources of radiation that are responsible for it. In a traditional view of H I reionisation, high redshift galaxy populations were the main drivers of the ionising background (Haardt & Madau, 2012; Faucher-Giguère *et al.*, 2009), due to the declining number density of Active Galactic Nuclei (AGN) at $z > 3$ (Fan *et al.*, 2006a). However, the relative contributions of these two types of sources to cosmic reionsa-

tion is still debated (Madau & Haardt, 2015), but also see D'Aloisio *et al.* (2017) and Hassan *et al.* (2017). This is motivated by the possibility of large numbers of faint high-redshift quasars at $z > 4$ (Giallongo *et al.*, 2012). Another major uncertainty in pin-pointing the relative contribution of galaxies and AGN arises due to the unknown fraction of ionising photons that escape into the IGM. Determining this factor is a key challenge due to the complexity of modelling photons escaping from the multi-phase interstellar medium into the IGM (Gnedin, Kravtsov & Chen, 2008; Ma *et al.*, 2015).

1.3 The intergalactic medium

Most of the baryons in the Universe reside in the space which lies between the galaxies, forming the IGM (see McQuinn (2016) and Lidz (2016) for reviews). It serves as a huge repository of diffuse gas. For this reason, the IGM is key tracer for the distribution of matter in the Universe and it has important implications for models of structure formation at small scales (at a few Mpc) (Viel *et al.*, 2013a; Iršič *et al.*, 2017c).

The formation of stars and galaxies in the densest regions of the cosmic web also influenced the gas in the IGM by various feedback processes. The gas is processed in galaxies and the material and momentum is injected back into the IGM through supernovae and galactic feedback (Cen & Ostriker, 2006). The gas is also photoionised, heated and enriched with metals through these processes. Hence, the IGM is fundamental for understanding the complete theory of galaxy formation, the role of feedback from galactic winds, supernovae and AGN (Oppenheimer *et al.*, 2010). The IGM also provides an invaluable record of reionsation, when the first sources produced ionising photons to end the dark ages (Miralda-Escudé & Rees, 1994; Peeples *et al.*, 2010; Kulkarni *et al.*, 2015; Nasir, Bolton & Becker, 2016; Oñorbe *et al.*, 2017).

Modelling the IGM through cosmic time is therefore quite challenging. However, there is an epoch at which our understanding of the low density IGM is well developed due to good agreement between the statistical properties of the Lyα forest (see Section 1.4), predicted by the hydrodynamical simulations and observations (Davé *et al.*, 1999; Schaye *et al.*, 2000; Croft *et al.*, 2002; Lidz *et al.*, 2006; Palanque-Delabrouille *et al.*, 2013; Viel *et al.*, 2013b; Bolton *et al.*, 2017). This is at $z = 2$–5, referred here as

intermediate redshifts. This is essentially due to the large number of observations made through ground based telescopes and the simplicity of the underlying model of the IGM at these redshifts. The IGM is mostly photoionised with a very low fraction of neutral hydrogen, kept in equilibrium by recombinations and ionising photons (Katz, Weinberg & Hernquist, 1996) contributed by galaxies and quasars. The sources form the ultra-violet background (UVB) which is assumed to be spatially uniform, forming the metagalactic ionising background. This assumption is a good approximation as the mean free path of ionising photons is large at intermediate redshifts (Croft, 2004; Worseck *et al.*, 2014), thus making the modelling of the IGM simpler at these epochs.

By contrast, at high redshifts $z \gtrsim 5$, the modelling of the IGM becomes complex as our basic assumptions break down at these epochs. The UVB which was assumed to be spatially uniform, is now fluctuating (Wyithe & Loeb, 2004), due to the appearance of rare sources and the shortening of the mean free path to ionising photons (Becker *et al.*, 2015). To model the properties of IGM near the end of reionsation, one has to take in to account all the parameters which were once considered uniform or non-evolving for simplicity. The detailed modelling of radiative transfer from the ionising sources into the IGM is the key challenge in modelling the IGM at high redshifts. At the low redshifts, $z < 2$, the key question is how galactic feedback redistributes the gas around galaxies shapes the IGM and galaxy evolution (Davé *et al.*, 2001, 2010; Cen & Ostriker, 2006).

1.4 Probing the IGM - the Lyman-α forest

Quasars are the most luminous objects in the Universe. They are powered by accreting gas on to the supermassive black holes (Lynden-Bell, 1969). These objects work like a massive lighthouse, shining light through the diffuse gas in the IGM that is otherwise difficult to observe in emission (Frank *et al.*, 2012). It was soon realized after the discovery of quasars (Schmidt, 1965), that there should be Lyα absorption from intervening neutral hydrogen in the IGM (Gunn & Peterson, 1965). However, it took key advancements at two fronts, before the Lyα forest became a dependable probe to study the intergalactic hydrogen. The first was the development of high resolution spectro-

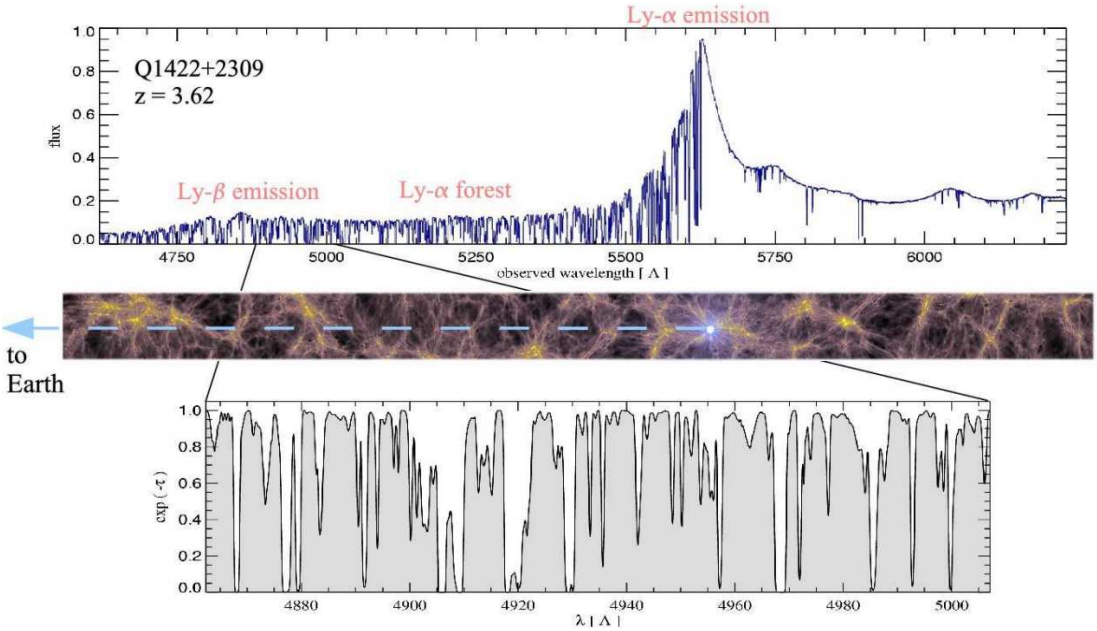


Figure 1.3: *Top:* High resolution spectrum of a quasar at $z = 3.62$. The Lyα emission peak is at wavelength, $1216(1 + z)$Å. The Lyα forest is a series of absorption lines blueward of that peak. The forest arises due to absorption by intervening neutral hydrogen along the line-of-sight through the Lyα transition. *Middle:* The gas distribution in a hydrodynamical simulation, showing the large scale structure. *Bottom:* The simulated line-of-sight predicted by the hydrodynamical simulation at $z = 3$. Figure taken from Springel, Frenk & White (2006).

graphs, (i.e. HIRES on Keck telescope), which made high resolution measurements of quasar spectra possible. The second was the development of the Cold Dark Matter (CDM) model and hydrodynamical simulations to predict the statistical properties of the Lyα forest. The progress at these fronts made it possible to explain the Lyα forest at intermediate redshifts, as the absorption of ultraviolet photons by a fluctuating medium, where most of the absorption is due to low density gas, which lies close to linear regime of hierarchical structure growth (Cen *et al.*, 1994; Hernquist *et al.*, 1996; Miralda-Escudé *et al.*, 1996; Theuns *et al.*, 1998; Zhang *et al.*, 1998; Gnedin & Hui, 1998; Davé *et al.*, 1999; Schaye, 2001; Meiksin, Bryan & Machacek, 2001; Theuns *et al.*, 2002a; Miralda-Escudé & Rees, 1994; Haehnelt & Steinmetz, 1998).

Figure 1.3, shows a typical high resolution quasar spectrum. It peaks at wavelength $1216(1 + z)$Å, where z is the redshift of the quasar ($z = 3.62$ in this case). The Lyα forest comprises of all the Lyα absorption lines blueward of this wavelength. Each absorption line at wavelength $1216(1+z_{\rm ab})$Å exists due to absorption by an intergalactic H I absorber at redshift $z_{\rm ab}$, along the quasar line-of-sight. Note that the forest also includes higher order transitions (such as Lyβ) at shorter wavelengths. The spectral features seen in quasar spectra are furthermore not limited to hydrogen transitions (i.e.

Lyα , Lyβ and so on). Any photon which is redshifted to a wavelength corresponding to a particular atomic or molecular transition gets absorbed by this species, providing a wealth of knowledge about the condition of intervening intergalactic gas and metals.

1.4.1 The Gunn-Peterson trough

Gunn & Peterson (1965) were the first to realise that if the intergalactic neutral hydrogen fraction is high enough it will completely attenuate the photons emitted by the quasars. This results in a trough, a region of complete absorption in Lyα forest. By following Gunn & Peterson (1965), it is possible to associate the observable, the transmitted flux, F (F is related to the optical depth, τ, through, $F = e^{-\tau}$), with the neutral hydrogen fraction.

Consider light with frequency, ν, emitted by a quasar at redshift $z_{\rm q}$. The light is observed at redshift, z (where $z < z_{\rm q}$), where it is redshifted to Lyα frequency, ν_α, where $\nu_\alpha = \nu(1+z)$. The corresponding optical depth, $\tau^\alpha(\nu)$, to these Lyα photons, due to absorption by H I gas with proper number density, $n_{\rm HI}(z)$ at redshift, z, for a path-length dl is

$$\tau^\alpha(\nu) = \int_0^{z_{\rm q}} \sigma(\nu(1+z)) n_{\rm HI}(z) \frac{dl}{dz} dz, \tag{1.1}$$

where $\sigma(\nu)$ is the cross section and the proper line element is given as $dl/dz = -c/H(z)(1+z)$. We may assume that the Lyα cross section is very peaked, which implies ignoring broadening effects (i.e thermal broadening or natural broadening). This simplification allows us to approximate the cross section as a Dirac delta function, peaked at ν_α, $\sigma(\nu(1+z)) = \sigma_\alpha \nu_\alpha \delta(\nu(1+z) - \nu_\alpha)$. Using the Einstein-de Sitter approximation, valid at high redshifts $z \geq 2$, $H(z) \simeq H_0 \Omega_{\rm m}^{1/2} (1+z)^{3/2}$ and changing the variable in integration to ν, gives

$$\tau^\alpha_{\rm GP} \simeq \frac{\sigma_\alpha c n_{\rm HI}(z)}{H_0 \Omega_{\rm m}^{1/2} (1+z)^{3/2}}, \tag{1.2}$$

where $\sigma_\alpha = 4.48 \times 10^{-18} {\rm cm}^2$, is the Ly$\alpha$ cross section. The hydrogen number density, $n_{\rm H}$, can be expressed in terms of a density normalised by the mean cosmic density,

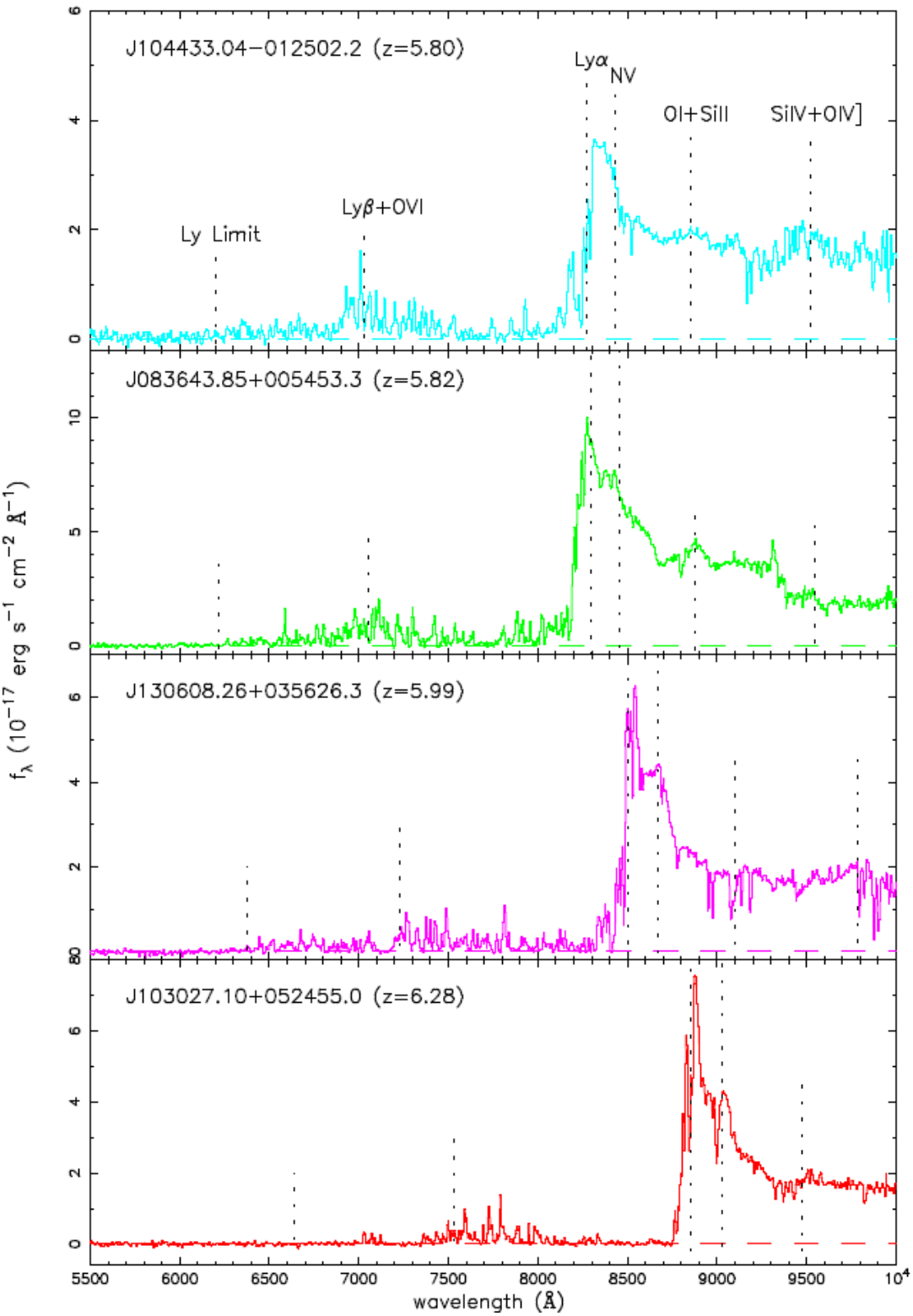


Figure 1.4: The optical spectrum of $z \gtrsim 6$ quasars, obtained by the Keck observatory and discovered by the Sloan Digital Sky Survey (SDSS). The detection of the first Gunn-Peterson trough in the spectrum of a quasar (bottom panel) at $z = 6.28$ is shown. The troughs are regions where the transmitted flux is consistent with zero flux, shown as the horizontal dashed lines. The prominent emission lines are shown as vertical dashed lines. The figure is taken from Becker *et al.* (2001).

$\Delta = \rho/\bar{\rho}$ such that

$$n_{\rm HI}(z) = \frac{\rho_{\rm crit}}{m_{\rm H}}\Omega_{\rm b}\Delta(1-Y)(1+z)^3. \tag{1.3}$$

Here, Y, is the primordial helium mass fraction and $\rho_{\rm crit}$ is the critical density. Now, defining the neutral hydrogen fraction as, $x_{\rm HI} = n_{\rm HI}/n_{\rm H}$, Equation 1.2 can be expressed as

$$\tau^{\alpha}_{\rm GP} \simeq 3\times10^5\times\Delta\, x_{\rm HI}\left(\frac{\Omega_{\rm b}h^2}{0.022}\right)\left(\frac{\Omega_{\rm m}h^2}{0.142}\right)^{-1/2}\left(\frac{1-Y}{0.76}\right)\left(\frac{1+z}{6}\right)^{3/2}. \tag{1.4}$$

There is one direct conclusion that can be drawn from the above equation. At higher redshifts $z \gtrsim 5$, the IGM has to be highly ionised meaning $x_{\rm HI} < 10^{-5}$, for the transmitted flux not to be saturated, $F \approx 0$. This also suggests that the absence of Gunn-Peterson troughs in quasar spectra at $z \gtrsim 5$ means that the neutral fraction has to be quite low. Although first predicted by Gunn & Peterson (1965), the trough was first observed by Becker *et al.* (2001) in a spectrum of the quasar at $z = 6.28$, as shown in Figure 1.4 (bottom panel). As the Lyα forest is very sensitive to the residual H I , this suggests that the quasar does not lie within the reionsation epoch. However, by comparing the quasar at $z = 5.99$, a rapid evolution of transmitted flux can be seen. This attenuation of Lyα transmitted flux as seen in quasars at $z \gtrsim 6$ suggests a lower limit on H I reionsation at $z \approx 6$ (Becker *et al.*, 2001; Fan *et al.*, 2006a).

To make the Lyα forest optical depth dependence on key physical quantities more explicit, Equation 1.4 can be refined further. This requires making some assumptions about the diffuse IGM in the post reionsation era. The number density of any species is physically set by the balance between creation and elimination rates. For the $n_{\rm HI}$, this is set by photoionisation and recombination such that

$$n_{\rm HI}\Gamma_{\rm HI} = n_{\rm e}n_{\rm HII}\alpha_{\rm HII}, \tag{1.5}$$

where $n_{\rm HII}, n_{\rm e}$ are the number densities of ionised hydrogen and electrons; $\Gamma_{\rm HI}$ and $\alpha_{\rm HII}$ are the H I photoionisation rate and the H II recombination coefficient. The best fit for $\alpha_{\rm HII}(T)$ is given as $\alpha_{\rm HII}(T) = 4.063\times10^{-13}(T/10^4K)^{-0.72}{\rm cm}^3\,{\rm s}^{-1}$ (Verner

& Ferland, 1996), which depends on the gas temperature. The photoionisation time scale is, $\Gamma_{\rm HI}^{-1} \sim 3.1 \times 10^4$ yrs, far shorter than the recombination timescale for an ionised IGM. Therefore, it is a good approximation to assume ionisation equilibrium and a highly ionised IGM, in the post reionsation epoch. Then, $n_{\rm HI} \approx n_{\rm HII}$, and $n_{\rm e} \approx n_{\rm HI} + n_{\rm HeI}$, where electrons are contributed by the ionisation of hydrogen and singly ionised helium atoms. By using Equation 1.4 and 1.5, the H I fraction can then be written as

$$x_{\rm HI} \simeq 1.7 \times 10^{-5} \Delta \frac{(1+\chi_{\rm He})}{\Gamma_{-12}} \left(\frac{T}{10^4{\rm K}}\right)^{-0.72} \left(\frac{1-Y}{0.76}\right) \left(\frac{1+z}{6}\right)^3, \qquad (1.6)$$

where $\chi_{\rm He}$, is the helium fraction given as $\chi_{\rm He} = Y/4(1-Y)$, accounting for singly ionised helium and $\Gamma_{-12} = \Gamma_{\rm HI}/10^{-12}\,{\rm s}^{-1}$.

During reionsation, however not only the is gas ionised but the excess photon energy also heats up the IGM. The processes which physically set the gas temperature are photoheating, radiative cooling, adiabatic cooling due to expansion of Universe and shock heating (e.g. Hui & Gnedin (1997)). The Lyα forest is sensitive to low density unshocked gas, where the interplay between the photoheating and adiabatic cooling results in a power law relationship between temperature and overdensity, $T = T_0 \Delta^{\gamma-1}$ (Hui & Gnedin, 1997; Upton Sanderbeck, D'Aloisio & McQuinn, 2016). Here, T_0, is the temperature at mean density and $\gamma - 1$ is the slope of the relation. Finally, combining, Equations 1.4 ,1.6 and using the temperature-density relation

$$\tau^{\alpha}_{\rm FGPA} \simeq 5.0 \times \Delta^{2-0.72(\gamma-1)} \frac{(1+\chi_{\rm He})}{\Gamma_{-12}} \left(\frac{T_0}{10^4{\rm K}}\right)^{-0.72} \left(\frac{1-Y}{0.76}\right)^2 \left(\frac{\Omega_{\rm b}h^2}{0.022}\right)^2 \left(\frac{\Omega_{\rm m}h^2}{0.142}\right)^{-1/2} \left(\frac{1+z}{6}\right)^{9/2}, \qquad (1.7)$$

The above expression is referred to as the Fluctuating Gunn-Peterson Approximation (FGPA) (Weinberg *et al.*, 1997), as describes the Lyα forest as a fluctuating density medium. Further, it shows the dependence of the optical depth (or equivalently transmitted flux, $e^{-\tau}$), on the key quantities temperature, overdensity and photoionisation rate needed to accurately model the Lyα forest with hydrodynamical simulations (see Section 1.5). Note this expression does not include the effects of thermal broadening,

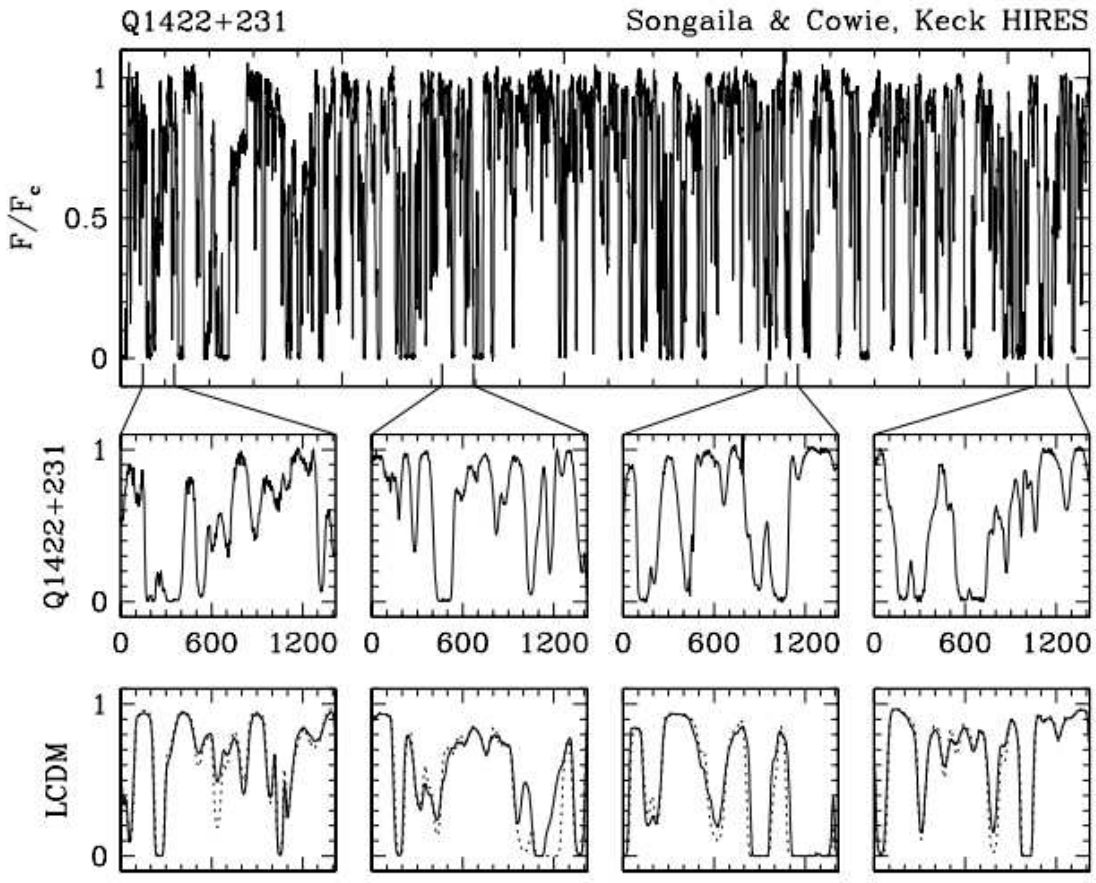


Figure 1.5: The continuum normalised spectrum of a quasar at $z = 3.62$, taken with Keck HIRES, zoomed at four regions (second row) each with length $1422\mathrm{km\,s^{-1}}$. The solid curve in the third row show the simulated spectrum extracted from hydrodynamical simulations at $z = 3$, with ΛCDM cosmology with $\Omega_\mathrm{m} = 0.2$, $\sigma_8 = 1$, $h = 0.65$, while the dotted curve is from N-body simulations at $z = 0$. The figure is taken from Weinberg *et al.* (2003).

peculiar velocities, fluctuations in the UVB and shock heating. To model the Lyα forest including all the relevant phenomena requires performing full hydrodynamical simulations.

1.5 Modelling the Lyman-α forest with cosmological simulations

Cosmological hydrodynamical simulations have been widely used to model the Lyα forest, and have been proven to be powerful tool for tracing the dark matter distribution (Cen *et al.*, 1994; Viel *et al.*, 2002; Weinberg *et al.*, 2003). Figure 1.5 shows an earlier hydrodynamical simulation, where the ΛCDM model (third row) qualitatively predicts the Lyα forest spectrum seen in observations by Keck using the HIRES spectrograph.

I will now highlight the key ingredients and main features in these simulations.

Most cosmological simulations start with a discrete set of particles with fixed masses on a Cartesian grid with periodic boundary conditions. The initial configuration of particles is set at an earlier epoch, usually at $z > 100$, by using linear perturbation theory. Each particle on the grid is displaced by adopting a matter power spectrum, based on the required cosmological model. Mostly, the Zel'dovich approximation (a linear perturbation approximation) is used to calculate the initial displacements for each particle (Zel'dovich, 1970). Once the initial particles positions are set, they are evolved by solving the Newtonian equations of motion.

Most cosmological simulations also include gas, which in Lagrangian models is also discretised as particles of equal masses. However, the dynamics of gas is governed by not only gravity but also dissipative and radiative processes, which involves the cooling and heating of gas. This is achieved by a hydro-solver, mostly following primordial gas for the Lyα forest, as metal line cooling has a very little effect on the Lyα forest (Viel, Schaye & Booth, 2013a). Another consideration for the simulations are the photionisation and photoheating rates, which are usually assumed to be spatially uniform and evolve over time. This forms the metagalactic UVB, which is incorporated into hydrodynamical simulations using pre-computed tables (Haardt & Madau, 2001, 2012; Faucher-Giguère *et al.*, 2009). The photoionisation rates can be rescaled in post-processing to match the observed Lyα forest flux in the observations. This is motivated by the argument that, in photoionisation equilibrium (ignoring collisional ionisation) $n_{\rm HI} \propto 1/\Gamma_{\rm HI}$.

Galactic feedback also has implications on the evolution of the IGM. This deposits gas from the galaxies out to the IGM, through outflows driven by supernovae and AGN. The impact of feedback on the Lyα forest is not considered important at intermediate redshifts (Theuns *et al.*, 2002a; Desjacques *et al.*, 2004; McDonald *et al.*, 2005). However this might not be the case at lower redshifts (Davé *et al.*, 2010; Viel, Schaye & Booth, 2013a; Nasir *et al.*, 2017).

Most of the Lyα forest studies require a direct comparison of extracted simulated spectra and their statistics from simulations with observations. However, the observations are plagued by several contaminants, which can complicate this task. This includes,

identifying and eliminating the absorption due to metals and damping wings. Accurately predicting the quasar continuum level, which can become challenging, is also important at higher redshifts and can induce systematics errors (Kim *et al.*, 2007; Lee, 2012). In the next section, I will discuss the comparison between simulations and observations. This can provide a myriad of information about the underlying gas density and thermal state of the IGM.

1.6 The Lyα forest statistics

The most commonly observed quantity in the Lyα forest is the transmitted flux, F, in the quasar spectra. In observations, one has to normalise the spectra with a continuum flux, $F_{\rm c}$, which is usually a fit to regions with the lowest absorption. There are two approaches to analyse the continuum normalised transmitted flux, $F/F_{\rm c}$. The first method is to treat it as a one dimensional continuous field. Some of the widely used quantities are flux decrements or the mean flux, the flux probability density distribution function (PDF) and the flux power spectrum. An alternative approach is to decompose the spectrum into its constituent absorption lines and study the statistics of the line features. Examples are the column density distribution function (CDDF) and the velocity (Doppler) widths distribution.

One of the simplest measurements obtained with the Lyα forest is the mean transmitted flux, $\langle F \rangle$. This is related to effective optical depth,$\tau_{\rm eff}$ through $\tau_{\rm eff} = -\ln\langle F \rangle$. This is also sometimes reported as a flux decrement, DA, where DA$= 1 - \langle F \rangle$. Most Lyα forest studies rely on calibrating the mean flux of mock spectra extracted from hydrodynamical simulations. The mean flux and its evolution is crucial for establishing the intensity of UVB and this affects others statistics, like the flux power spectrum and flux PDF (Rauch *et al.*, 1997; Bolton *et al.*, 2005; Faucher-Giguère *et al.*, 2008; Becker & Bolton, 2013). The optical depth of Lyα forest is proportional to neutral hydrogen, which scales as $n_{\rm HI} \propto T^{-0.72}\Gamma_{\rm HI}^{-1}$. Therefore, to obtain an estimate for the intensity of the UVB using optical depth measurements, one has to assume a gas temperature which can lead to different estimates for the ionising background.

The flux PDF gives the probability that a given pixel has a transmission, on a scale

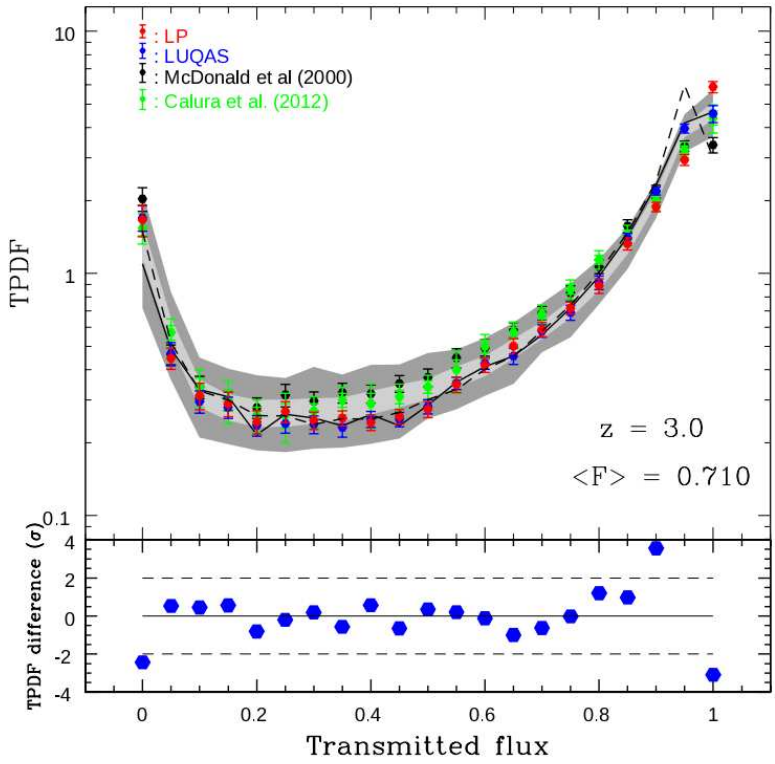


Figure 1.6: *Top:* The Lyα forest transmitted flux PDF at $z = 3$. The flux PDF obtained from hydrodynamical simulations is overlaid with data points from four different measurements. The shaded areas show 1σ and 2σ errors. *Bottom:* The difference between simulated flux PDF compared with the LP observations (red points), normalised in units of 1σ errors. The figure is taken from Rollinde *et al.* (2013).

of zero to one, where a pixel at the continuum has a probability of one (e.g. Miralda-Escudé *et al.* (1996)). Figure 1.6 shows the flux PDF obtained from hydrodynamical simulation and compared with four different measurements. The PDF has been widely employed in past studies (McDonald *et al.*, 2000; Lidz *et al.*, 2006; Kim *et al.*, 2007; Lee *et al.*, 2015). Figure 1.6, shows the flux PDF obtained with the GIMIC cosmological simulations (Crain *et al.*, 2009) compared with four independent measurements at $z = 2$–3. The authors find a good agreement between simulations and observations, where most of the measurements lie within 2σ errors obtained by bootstrap resampling. The noticeable deviations are at $F \approx 0$ and $F > 0.8$. The continuum correction can help to alleviate the discrepancy at $F > 0.8$ (Lee *et al.*, 2015; Bolton *et al.*, 2017). One the other hand, the galactic feedback prescriptions have a noticeable impact on the saturated pixels at $F \approx 0$ (Bolton *et al.*, 2017).

The one dimensional Lyα flux power spectrum (see Figure 1.7) is one of the most widely studied flux statistics. The line-of-sight power spectrum, $P_{\rm F}(k)$, is obtained from the Fourier transform of the estimator, $\delta_{\rm F} = F/\langle F\rangle - 1$, as $P_{\rm F}(k) = L^{-1}|\delta_{\rm F}(k)|^2$,

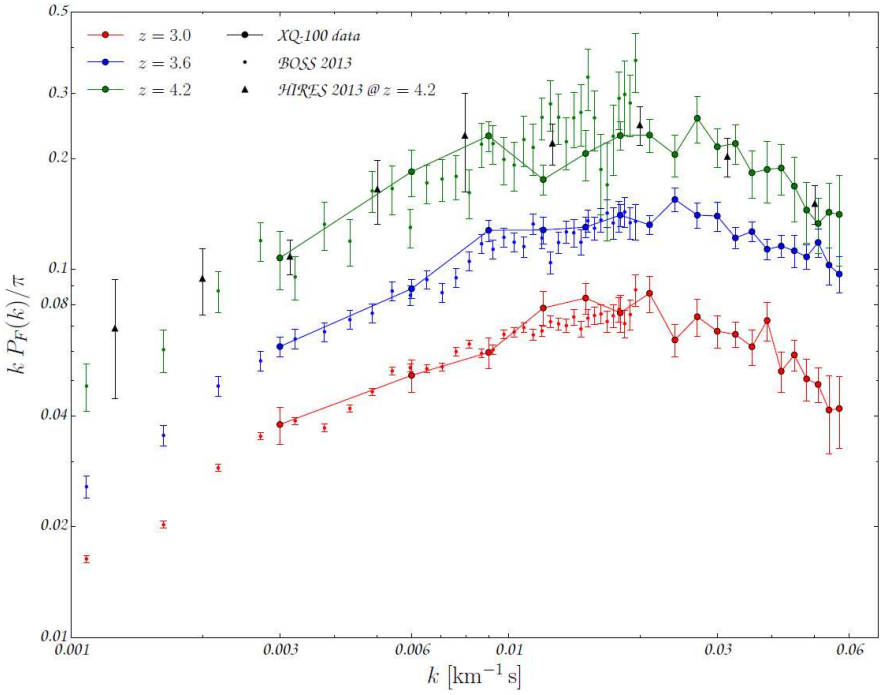


Figure 1.7: A comparison of transmitted flux power spectrum measurements at $z = 3, 3.6,$ and 4.2, from Iršič *et al.* (2017a) (filled circles), Palanque-Delabrouille *et al.* (2013) (filled square) and Viel *et al.* (2013b) (filled triangle). The plot is taken from Iršič *et al.* (2017a).

where $\delta_{\rm F}(k)$, is the Fourier transform of $\delta_{\rm F}$ and L is length of each line of sight. Usually, the flux power spectrum is presented as $kP_{\rm F}(k)/\pi$, against wavenumber k, in units of $\rm km^{-1}\,s$. Intuitively, the flux power spectrum probes the distribution of matter at different scales. At small wavenumbers (large scales) it follows the large scale dark matter distribution (Croft *et al.*, 1998; Viel, Haehnelt & Springel, 2004a). By contrast, at large wavenumbers (small scales), it is sensitive to a combination of non-linear structure formation, thermal broadening, pressure smoothing of the gas and the nature of the dark matter (Peeples *et al.*, 2010; Iršič *et al.*, 2017c). There is a large number of Lyα flux power measurements available to date, ranging over three orders of magnitude in wavenumber (Croft *et al.*, 1998; Viel, Haehnelt & Springel, 2004a; Viel, Schaye & Booth, 2013a; Palanque-Delabrouille *et al.*, 2013; Iršič *et al.*, 2017a). The sensitivity on the gas pressure smoothing on small scales makes it a powerful tool to constrain the integrated thermal history of IGM (Nasir, Bolton & Becker, 2016; Oñorbe *et al.*, 2017). The flux power spectrum has also been employed to compare simulation predictions with observations, to obtain constraints on the matter power spectrum (Croft *et al.*, 1998, 2002; Seljak *et al.*, 2005; Zaroubi *et al.*, 2006; Palanque-Delabrouille *et al.*, 2013; Viel *et al.*, 2013b; Iršič *et al.*, 2017c). The statistic also helps to decouple the various systematics, like the signal-to-noise and metals which tend to

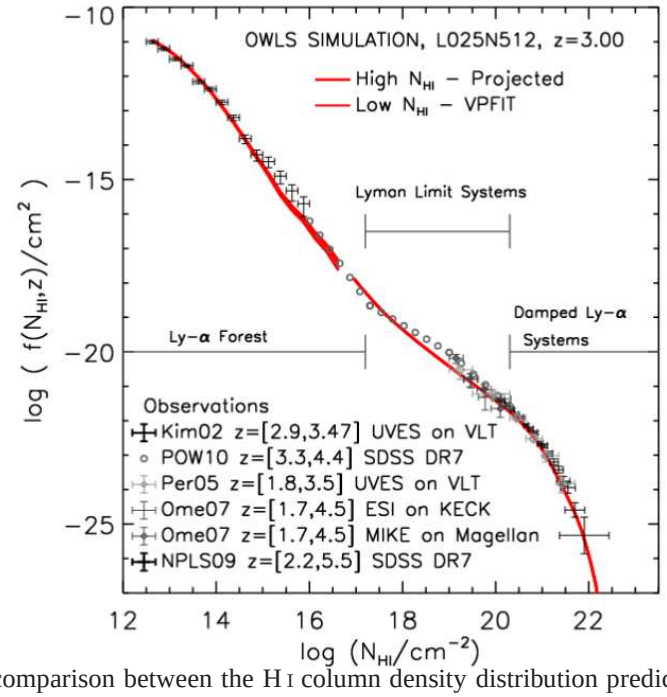


Figure 1.8: A comparison between the H I column density distribution predicted by the OWLS simulations (red curve) with observations shown as symbols. The gap at $N_{\rm HI} = 10^{17}{\rm cm}^{-2}$ separates column densities probed by Lyα forest observations and high column density systems. The red curve at $N_{\rm HI} < 10^{17}{\rm cm}^{-2}$ is obtained from mock spectra by Voigt profile fitting with VPFIT. The rest of the curve is obtained by projecting H I densities.

contribute to power at different scales.

In addition, there are several statistics which are derived from H I absorption line features (i.e. the column density $N_{\rm HI}$ and velocity width, $b_{\rm HI}$), by decomposing the spectrum into individual absorbers. Quantities which are widely studied are the CDDF, line width distribution and number density of absorbers per unit redshift (Hui, Gnedin & Zhang, 1997; Davé *et al.*, 1997; Schaye *et al.*, 2000; Schaye, 2001; Altay *et al.*, 2011; Kim *et al.*, 2013; Bolton *et al.*, 2017).

The CDDF (see Figure 1.8) is defined as the number of absorbers per unit H I column density per unit path length, $\partial^2 N/\partial N_{\rm HI}\partial X$. The statistic is sensitive to the density distribution of absorbers. Recently, it has been shown that hydrodynamical simulations are in remarkable agreement with observations over the range of column densities ($N_{\rm HI} = 10^{13} - 10^{17}{\rm cm}^{-2}$) probed by Ly$\alpha$ forest (Altay *et al.*, 2011; Rahmati *et al.*, 2013). Mostly, the higher column density systems lie within the vicinity of galaxies, which makes them a potential probe to study the impact of galactic feedback, specifically at lower redshifts (Davé *et al.*, 2010; Viel *et al.*, 2017a; Nasir *et al.*, 2017).

An expression which relates the column density of typical absorber with its physical

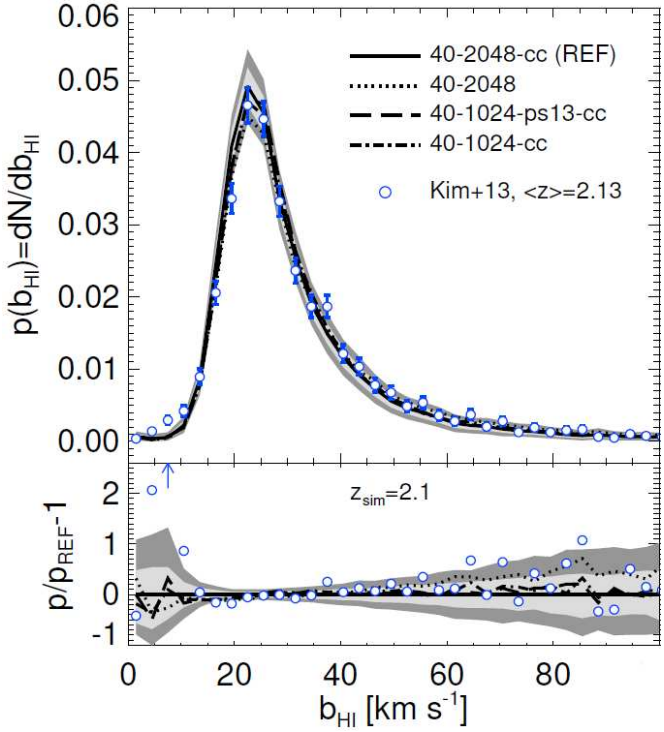


Figure 1.9: *Top:* The Lyα velocity width distribution at $z = 2.1$, from a number of hydrodynamical simulations with different galactic feedback prescriptions, compared with observations by Kim *et al.* (2013). *Bottom:* The simulated and observations relative to the reference model. Figure taken from Bolton *et al.* (2017).

density and temperature was first suggested by Schaye (2001). The main assumption is that the physical scale of these absorbers is the local Jeans scale.

$$N_{\rm HI} = \frac{2.44 \times 10^{12}\,{\rm cm}^{-2}}{\Gamma_{-12}} \left(\frac{\Delta}{10}\right)^{3/2} \left(\frac{T}{2 \times 10^4/K}\right)^{-0.26} \left(\frac{1+z}{1.1}\right)^{9/2} \tag{1.8}$$

This relation encapsulates the key factors, determining the evolution of column density. For a constant ionising background, the physical density decreases due to Hubble expansion, lowering the recombination rate and eventually decreasing the column density at a fixed density. Furthermore, an increase in the intensity of UVB lowers the column density, by increasing ionised fractions. The CDDF extracted from hydrodynamical simulations can be compared with observations, to infer the intensity of ionising background (Kollmeier *et al.*, 2014; Shull, Danforth & Tilton, 2014).

Another statistic which is often encountered in Lyα forest studies is the PDF of the line widths (see Figure 1.9), $b_{\rm HI}$ (Davé *et al.*, 1997; Tytler *et al.*, 2009; Bolton *et al.*, 2017). This serves as a diagnostic to pinpoint any processes which can potentially broaden the line profile either thermally or through turbulence. This includes thermal broaden-

ing due to the instantaneous gas temperature, pressure smoothing, cosmic expansion and additional thermal sources (Puchwein *et al.*, 2012), such as He II reionsation. The absorption line features, $N_{\rm HI}$ and $b_{\rm HI}$, can both be applied to infer the thermal state of IGM (Schaye *et al.*, 2000; Ricotti, Gnedin & Shull, 2000; Bolton *et al.*, 2014).

In conclusion, simulations show a good agreement with the Lyα forest observations at intermediate redshifts, $z = 2$–5, for the statistics I have discussed. However, our understanding at lower or higher redshifts is far from complete. Next, I will discuss the key questions which are vital to our complete understanding of IGM and Lyα forest at these epochs.

1.7 The Lyα forest at high redshifts, $z \gtrsim 5$

Our understanding of high redshift IGM is shaped by the process of reionsation. The Lyα forest provides a rich avenue for studying the thermal and ionisation state of IGM at these epochs. The main feature of the Lyα forest as observed in quasar spectra is the large spatial variations in the transmitted flux at redshifts $z \gtrsim 5.5$ (Songaila, 2004; Fan *et al.*, 2006b), which serves as a lower constraint on the end of reionsation. Interestingly, the Lyα opacity variations seen at $z \sim 6$ (Becker *et al.*, 2015), cannot be explained by simple models of reionsation, that assume a uniform or fluctuating UVB with a constant mean free path. The potential solution lies in a combination of variations in the mean free path, fluctuations in UVB driven by rare bright quasars and variations in gas temperature, consistent with inhomogenous reionisation (D' Aloisio, McQuinn & Trac, 2015; Chardin *et al.*, 2015; Chardin, Puchwein & Haehnelt, 2017)

The precise timing and history of reionsation remain poorly constrained to date. Due to the complexity of the problem and the scarcity of measurements at higher redshifts, several models remain consistent with the observations. Furthermore, the IGM serves as a huge reservoir where energy is deposited during the process of reionsation by photoheating. One way to measure this heat injection is by utilizing the sensitivity of the line of sight transmitted flux power spectrum at small scales, at $z \simeq 4$–5 (Nasir, Bolton & Becker, 2016; Oñorbe *et al.*, 2017). A careful analysis of recent flux power spectrum measurements and the hydrodynamical simulations can translate this in to a

constraint on the redshift of reionsation. The models and data are consistent with the recent Planck results and a conventional reionsation scenario, driven by high redshift galaxies (Oñorbe *et al.*, 2017). See also Chapter 5 for more discussion.

1.8 The Lyα forest at low redshifts, $z \lesssim 2$

At lower redshifts, the cosmic expansion leads to a decrease in the physical density, lowering the recombination rate, and a declining UVB due to the drop in number density of quasars (Davé *et al.*, 2010). The Lyα forest becomes far more transparent at $z < 2$, where absorption lines lie very near to the quasar continuum. The line of sight effective optical depth at $z \sim 0$, drops to $\tau_{\rm eff} \simeq 0.015$ (Kirkman *et al.*, 2007; Danforth *et al.*, 2016).

The low redshift IGM is of great importance for our understanding of enrichment mechanisms in the IGM and circumgalactic medium. At higher redshifts, most of the baryons ($\sim 80\%$) lie within the non-luminous IGM, in the form of diffuse photoionised systems, observed through the Lyα forest (Davé *et al.*, 1999; Shull, Smith & Danforth, 2012). At low-redshift, $z \simeq 0$, they can be in a cool diffuse state or in the form of the Warm Hot Ionised Medium (WHIM), reaching $T > 10^5$K, far beyond the temperatures achieved through photoionisation, due to shock heating from structure formation (Davé *et al.*, 1999, 2010). The lower density and unshocked gas is mostly observed through absorption lines seen in quasar spectra, such as H I and metal lines.

Importantly, the wavelength for the low redshift Lyα forest observations lie in the far-ultraviolet band. Therefore, the observations are made possible primarily through a series of space based instruments, mounted on the Hubble Space Telescope (HST). The instruments like the Faint Object Spectrograph (FOS), the Space Telescope Imaging Spectrograph (STIS), and recently, the Cosmic Origins Spectrograph (COS), have supported low redshift absorption line studies for the past two decades (Bahcall *et al.*, 1993; Weymann *et al.*, 1998; Kirkman *et al.*, 2007; Tilton *et al.*, 2012; Danforth *et al.*, 2016).

The past studies have shown that galactic feedback can significantly increase the WHIM fraction in the IGM, through feedback by supernovae and AGN (Cen & Ostriker, 2006;

Davé *et al.*, 2010; Tepper-García *et al.*, 2012). There is also a recent surge of studies to understand the impact of galactic feedback processes, by comparing COS observations with simulations, utilizing various feedback prescriptions (Gurvich, Burkhart & Bird, 2017; Viel *et al.*, 2017a; Nasir *et al.*, 2017). This usually involves a careful comparison of various observed statistics to simulations.

1.9 Thesis overview

The aim of this thesis is to address some of the key science questions raised in this introduction. Some of these are, the role of galactic feedback in the low-redshift Lyα forest, the intensity of the ultra-violet background and the timing and nature of reionsation. I plan to address these queries using state-of-the art hydrodynamical simulations of the Lyα forest and the various statistical quantities introduced in this chapter.

In Chapter 2, I present the comparison of key statistical properties of low redshift Lyα forest simulations with COS observations. The main objective is to study the impact of galactic feedback and different star formation methods in hydrodynamical simulations of the Lyα forest. In Chapter 3, I discuss the numerical convergence of these quantities from the simulations.

In Chapter 4, I discuss the potential of the Lyα forest power spectrum for constraining the integrated thermal history of the IGM at $z \simeq 5$. I first establish its sensitivity to pressure smoothing using the flux power spectrum and then a perform an Bayesian analysis to obtain constraints on the integrated thermal history.

The objective of Chapter 5 is to obtain the first constraints on the integrated thermal history of IGM using the Lyα forest flux power spectrum measurements from Viel *et al.* (2013b). This is achieved by using new set of hydrodynamical simulations and introducing improvements to the method in Chapter 4. I then discuss the implications of the results in the context of constraining models of reionsation.

Finally, in chapter 6, I summarise and discuss potential future directions.

Chapter 2

The effect of stellar and AGN feedback on the low redshift Lyman-α forest in the Sherwood simulation suite

2.1 Introduction

The Lyα forest is an indispensable tool for probing the evolution and distribution of gas in the intergalactic medium (see Meiksin, 2009; McQuinn, 2016, for reviews). At intermediate redshifts ($2 \lesssim z \lesssim 5$), the majority of the intergalactic medium (IGM) by volume is in the form of warm ($T \sim 10^4\,\mathrm{K}$) diffuse gas that is kept photo-ionised by the metagalactic ultraviolet background (UVB). The latest hydrodynamical simulations of the IGM that model the Lyα forest of absorption produced by this gas are in very good agreement with a wide range of spectroscopic data from optical, ground-based telescopes (e.g. Bolton *et al.*, 2017). However, at lower redshifts ($z \lesssim 2$), due to the interplay between cosmic expansion, the growth of structure and the declining intensity of the UVB, the Lyα forest thins out and becomes more transmissive (Danforth *et al.*, 2016). By $z \sim 0$ a significant fraction of the baryons in the IGM are in a collisionally ionised, shock heated phase with temperatures $T \sim 10^5$–$10^7\,\mathrm{K}$ (Cen & Ostriker, 1999). In the present day Universe, the Lyα forest therefore traces less than one half of the remaining diffuse gas in the IGM (Lehner *et al.*, 2007; Shull, Smith & Danforth, 2012).

Over the past two decades, the properties of Lyα absorption arising from the low redshift IGM have been studied with observations made by a series of space-based UV spectrographs (Bahcall *et al.*, 1993; Weymann *et al.*, 1998; Janknecht *et al.*, 2006; Kirkman *et al.*, 2007; Williger *et al.*, 2010; Tilton *et al.*, 2012). Most recently, the *Cosmic Origins Spectrograph* (COS, Green *et al.*, 2012), mounted on the *Hubble Space Telescope* (HST) has collected many more active galactic nuclei (AGN) spectra with improved signal-to-noise, providing new opportunities for absorption line studies of the low redshift Lyα forest (Shull, Danforth & Tilton, 2014; Danforth *et al.*, 2016; Pachat *et al.*, 2016). Some of the key questions addressed by recent investigations are related to the nature of these Lyα absorbers, and their relationship to the evolution of the UVB and galactic feedback (see e.g. Davé *et al.*, 2010; Tepper-García *et al.*, 2012; Kollmeier *et al.*, 2014; Shull *et al.*, 2015; Khaire *et al.*, 2016; Viel *et al.*, 2017b; Gurvich, Burkhart & Bird, 2017).

The mostly widely used measurements of Lyα absorbers at $z < 2$ are the column density distribution function (CDDF), the velocity (Doppler) widths of the absorption lines and the evolution of the absorption line number density with redshift. The CDDF shape and normalisation is determined by the density distribution of absorbers and the intensity of the UVB. The velocity width distribution provides constraints on the gas temperature. Furthermore, both observables are in principle sensitive to galactic feedback. In this context, hydrodynamical simulations have significantly aided our understanding and interpretation of these observational data (Rauch *et al.*, 1997; Theuns, Leonard & Efstathiou, 1998; Davé *et al.*, 1999; Richter, Fang & Bryan, 2006; Paschos *et al.*, 2009; Oppenheimer & Davé, 2009; Davé *et al.*, 2010; Rahmati *et al.*, 2013).

Of particular note is the recent comparison of the CDDF for Lyα absorbers at $z \simeq 0.1$ observed with COS (Danforth *et al.*, 2016) to hydrodynamical simulations. Kollmeier *et al.* (2014) reported that the UVB intensity needed to match the COS measurement of the CDDF is a factor of five larger than predicted by empirically calibrated UVB models (Haardt & Madau, 2012, HM12). The claimed "photon underproduction crisis" prompted further investigation into this apparent discrepancy. Large uncertainties in the production rate of ionising photons by quasars and star forming galaxies, and possibly also the role of AGN feedback, have been suggested as the likely cause (Khaire

& Srianand, 2015; Shull *et al.*, 2015; Wakker *et al.*, 2015; Gurvich, Burkhart & Bird, 2017; Gaikwad *et al.*, 2017a).

Viel *et al.* (2017b) (hereafter V17) also recently considered this problem using hydrodynamical simulations including Illustris (Vogelsberger *et al.*, 2014b) and a sub-set of the Sherwood simulations (Bolton *et al.*, 2017). They concluded the HM12 photoionisation rate needed to be increased by a factor of two in the hydrodynamical simulations to match the observed CDDF, smaller than the factor of five found by Kollmeier *et al.* (2014). However, in contrast to other recent studies, V17 also focussed on the distribution of Lyα line velocity widths (see also Gaikwad *et al.*, 2017b). V17 found that the simulations struggled to reproduce the Lyα velocity width distribution at $z \simeq 0.1$, producing line widths that were too narrow compared to the COS data. This was attributed to gas in the simulations that was either too cold to produce the observed line widths, or too highly (collisionally) ionised to produce Lyα absorption due to vigorous AGN feedback heating the gas to $T > 10^5\,\mathrm{K}$ (particularly in the Illustris simulation). V17 concluded that the Lyα line width distribution at $z \simeq 0.1$ is a valuable diagnostic for models of feedback in the low redshift Universe.

The goal of the present chapter is to the extend the V17 analysis, and present in full the low redshift ($0 < z < 2$) IGM models that V17 used from the Sherwood simulation suite (Bolton *et al.*, 2017). Following V17, we perform the same Voigt profile analysis on the simulations and COS data to minimise potential biases in the comparison due to line fitting. This furthermore enables a detailed assessment of the effect that our stellar and AGN feedback implementation has on the Lyα forest.

The contents of this chapter are published in Nasir *et al.* (2017). The chapter is organised as follows. In Section 2.2, we briefly describe the simulations used. In Section 2.3, we compare the simulations to current observational data at $z < 2$ and assess the impact of different galactic feedback prescriptions on the Lyα forest observables, including the the Lyα velocity width distribution. The physical origin of the absorbers is examined in Section 2.4. Finally, we summarise our results in Section 2.5. Throughout this chapter we refer to comoving distances with the prefix "c". The cosmological parameters used throughout this chapter are $\Omega_\mathrm{m} = 0.308$, $\Omega_\Lambda = 0.692$, $h = 0.678$, $\Omega_\mathrm{b} = 0.0482$, $\sigma_8 = 0.829$ and $n = 0.961$ consistent with the best fit

Table 2.1: The hydrodynamical simulations used in this chapter. The first column uses the naming convention *L-N-param*. Here L is the box size in units of $h^{-1}\mathrm{cMpc}$, N is the cube root of the total number of gas particles and *-param* is associated with the subgrid treatment of star formation and feedback. Here $-ps13$ refers to the star formation and energy driven outflow model of Puchwein & Springel (2013), while *-ps13+agn* also includes AGN feedback based on Sijacki *et al.* (2007). All other models instead convert all cold ($T < 10^5\,\mathrm{K}$), dense ($\Delta > 1000$) gas into collisionless particles. The remaining columns give the mass of each dark matter and gas particle in $h^{-1}M_\odot$ and the gravitational softening length in $h^{-1}\mathrm{ckpc}$. All simulations are performed to $z = 0$.

Name	M_{dm} $[h^{-1}M_\odot]$	M_{gas} $[h^{-1}M_\odot]$	l_{soft} $[h^{-1}\mathrm{ckpc}]$
80-512-ps13	2.75×10^8	5.10×10^7	6.25
80-512-ps13+agn	2.75×10^8	5.10×10^7	6.25
80-512	2.75×10^8	5.10×10^7	6.25
80-1024	3.44×10^7	6.38×10^6	3.13
80-256	2.20×10^9	4.08×10^8	12.50
40-512	3.44×10^7	6.38×10^6	3.13
20-256	3.44×10^7	6.38×10^6	3.13

$\Lambda\mathrm{CDM} + Planck + WP + highL + BAO$ cosmological parameters (Planck Collaboration *et al.*, 2014).

2.2 Methodology

2.2.1 Hydrodynamical simulations

The simulations used in this work are summarised in Table 2.1. These were performed using P-GADGET-3, a modified version of the publicly available code GADGET-2 (Springel, 2005). The initial conditions were generated at $z = 99$ on a Cartesian grid using the N-GENIC code (Springel *et al.*, 2005b) using transfer functions generated by CAMB (Lewis, Challinor & Lasenby, 2000). A detailed description of these models may be found in the Sherwood overview paper (Bolton *et al.*, 2017).

The photo-ionisation and photo-heating rates are calculated using a spatially uniform UVB model for emission from star forming galaxies and quasars (Haardt & Madau, 2012) applied in the optically thin limit. A small increase to the He II photo-heating rate, $\epsilon_{\mathrm{HeII}} = 1.7\epsilon_{\mathrm{HeII}}^{\mathrm{HM12}}$ at $2.2 < z < 3.4$ was applied to better match observational measurements of the IGM temperature at $z > 2$ (Becker *et al.*, 2011). The ionised fractions for hydrogen and helium are obtained assuming ionisation equilibrium. Metal

line cooling is not included, although this is not expected to impact significantly on the Lyα forest at the redshifts considered here (Tepper-García *et al.*, 2012). In five of the simulations, gas particles with temperatures $T < 10^5$K and densities $\Delta = \rho/\langle\rho\rangle > 1000$ are converted into collisionless star particles (the QUICKLYA method, see Viel, Haehnelt & Springel, 2004b) to speed up the calculation. We will show this choice makes very little difference to Lyα forest systems at low column densities, $N_{\rm HI} < 10^{14.5}\,{\rm cm}^{-2}$, in our analysis. However, galactic winds and AGN feedback may have an impact on high column density lines that probe the (circumgalactic) gas in the vicinity of dark matter haloes. Therefore, two models that follow star formation and feedback are included. The first model (80-512-ps13) includes energy driven galactic outflows following Puchwein & Springel (2013). The star formation model is based on Springel & Hernquist (2003), but assumes a Chabrier rather than Salpeter initial mass function (IMF) and a galactic wind velocity that is directly proportional to the escape velocity of the galaxy. These choices increase the available supernovae feedback energy by a factor of two, as well as raising the mass-loading of winds in low-mass galaxies. The second run (80-512-ps13+agn) also incorporates AGN feedback, again following Puchwein & Springel (2013). This AGN feedback model is based on Sijacki *et al.* (2007). In the "quasar" mode, when accretion rates are above 0.01 of the Eddington rate, only 0.5 per cent of the accreted rest mass energy is thermally coupled to the surrounding gas. For lower accretion rates a more efficient coupling of AGN jets in the "radio" mode is assumed and 2 per cent of the rest mass energy is used for recurrently injecting hot AGN bubbles.

The evolution of the low-density IGM thermal history at $z < 2$ in a sub-set of the simulations is displayed in Figure 2.1. This is parameterised as a power law temperature-density ($T - \Delta$) relation for the low density ($\Delta < 1$–10) IGM, $T = T_0\Delta^{\gamma-1}$. Here $\Delta = \rho/\langle\rho\rangle$ is the gas density normalised by the background density, T_0 is the gas temperature at mean density and $\gamma - 1$ is the slope of the relation (Gnedin & Hui, 1998; Upton Sanderbeck, D'Aloisio & McQuinn, 2016). Note that the 80-512-ps13, 80-512-ps13+agn and 80-512 models have very similar thermal histories; this suggests gas at the mean background density is not strongly impacted by feedback. Additionally, by comparing these models to the 80-1024 simulation (solid black line), it is clear that the lower resolution simulations are not converged, with volume weighted temperatures

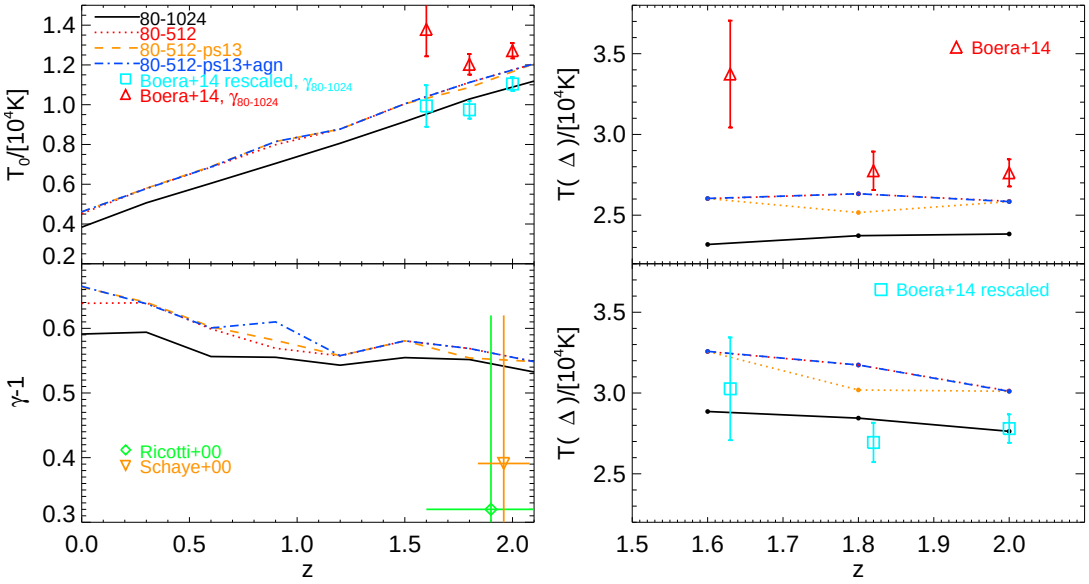


Figure 2.1: *Left:* The redshift evolution of the volume weighted temperature at mean density, T_0 (upper panel) and slope of the power-law temperature-density relation, $\gamma - 1$ (lower panel), where $T = T_0 \Delta^{\gamma-1}$. The parameters are obtained from the volume weighted $T - \Delta$ plane by finding the mode of the gas temperature in bins of width 0.02 dex at $\log \Delta = 0$ and -0.7. The T_0 data points with 1σ errors (red triangles) are inferred from IGM temperature measurements at the characteristic density probed by the Lyα forest, $T(\bar{\Delta})$, obtained by Boera *et al.* (2014), evaluated at the $\gamma - 1$ values predicted by the 80-1024 model. The same measurements scaled to match the Becker *et al.* (2011) effective optical depth are displayed as cyan squares (see text for details). The $\gamma - 1$ data points with 1σ errors are from Schaye *et al.* (2000) (orange inverted triangle) and Ricotti, Gnedin & Shull (2000) (green diamond). *Right:* The temperature at the characteristic density probed by the Lyα forest, $T(\bar{\Delta})$, for the same models overlaid with data from Boera *et al.* (2014) (top panel) and following recalibration to match the Becker *et al.* (2011) effective optical depth (bottom panel). The characteristic densities at $z = [1.63, 1.82, 2.00]$ are $\bar{\Delta} = [5.13, 4.55, 4.11]$ ($\bar{\Delta} = [7.65, 6.32, 5.38]$) for the fiducial (recalibrated) Boera *et al.* (2014) temperature measurements.

at mean density $\sim 800\,\mathrm{K}$ hotter in the 80-512 runs (further details may be found in Chapter 3).

There are currently no detailed observational constraints on the temperature of the low density IGM at $z < 1.6$, but there are a few measurements from optical data at $1.6 \leq z \leq 2$. In the upper left panel of Figure 2.1 the red triangles show the IGM temperature at mean density from Boera *et al.* (2014). This study uses the curvature of the Lyα forest transmitted flux to measure the gas temperature at the characteristic density, $T(\bar{\Delta})$, probed by the Lyα forest absorption. We derive values for T_0 from these data assuming the $\gamma - 1$ for the 80-1024 model shown in the lower left panel, such that $T_0 = T(\bar{\Delta})/\bar{\Delta}^{\gamma-1}$. Additionally, the cyan squares display the Boera *et al.* (2014) measurements obtained assuming the effective optical depth, $\tau_{\rm eff}$ (where $\tau_{\rm eff} = -\ln\langle F \rangle$ and $\langle F \rangle$ is the mean transmission in the Lyα forest), evolution used

in an earlier curvature analysis performed by Becker *et al.* (2011) (E. Boera, private communication). The effective optical depth sets the characteristic gas density probed by the Lyα forest, and this comparison gives an indication of the likely systematic uncertainty in $\tau_{\rm eff}$ arising from line of sight variance. For completeness, we also directly compare the simulations to the $T(\bar{\Delta})$ measurements in the right panel of Figure 2.1. The measurements bracket all the simulations at $z > 1.6$. The models are also formally consistent with the constraints on $\gamma - 1$ from Schaye *et al.* (2000) and Ricotti, Gnedin & Shull (2000) shown in the lower left panel of Figure 2.1. These were obtained from an analysis of the lower envelope of the column density – velocity width plane obtained from Voigt profile fits to the Lyα forest, although the error bars on these measurements are very large. Note also the simulations do not follow non-equilibrium ionisation effects, and therefore produce a temperature-density relation slope that is steeper by $\Delta(\gamma - 1) \sim 0.1$ at $z = 1$–2 compared to the recent study by Puchwein *et al.* (2015).

In all cases the simulated T_0 monotonically decreases toward lower redshift as the IGM cools due to adiabatic expansion, reaching $\sim 4000\,{\rm K}$ by $z = 0$. The agreement with measurements of the IGM thermal state at $1.6 < z < 2$ suggests the photo-heating rates used in the UVB model are broadly correct at these (and higher) redshifts. Significantly higher temperatures at mean density than those predicted by the models at $z < 1.6$ would require an additional, unidentified source of heating in the low density IGM.

2.2.2 Mock Lyα forest spectra

Mock Lyα forest spectra were obtained by extracting 5000 lines of sight parallel to each of the box axes on regularly spaced grids of 50^2, 40^2 and 30^2, each with 2048 pixels. The H I Lyα optical depths, $\tau^{\alpha}_{\rm HI}$, are obtained using the method described by Theuns *et al.* (1998) combined with the Voigt profile approximation described by Tepper-García (2006). The transmitted flux, F, in each pixel is then $F = e^{-\tau^{\alpha}_{\rm HI}}$, and the effective optical depth evolution with redshift is averaged over all sight lines. In our analysis we also make use of the fact that the pixel optical depths are inversely proportional to the H I photo-ionisation rate, $\tau^{\alpha}_{\rm HI} \propto \Gamma^{-1}_{\rm HI}$. This enables the optical depths (and hence the $\tau_{\rm eff}$ evolution) to be rescaled to match different UVB models in post-processing

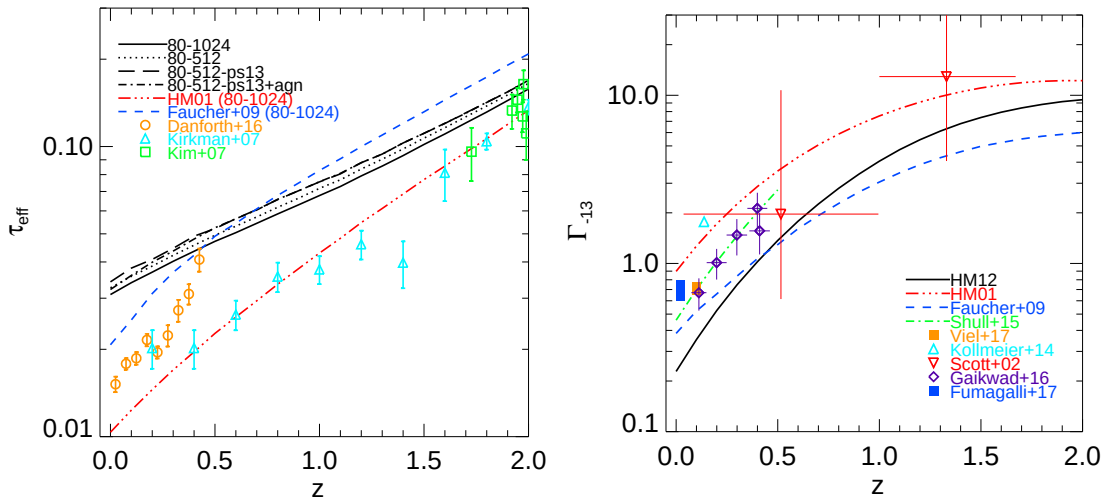


Figure 2.2: *Left:* The redshift evolution of the effective optical depth, $\tau_{\rm eff}$, predicted by the hydrodynamical simulations. The evolution using the HM01 (red triple-dot dashed line) and Faucher-Giguère *et al.* (2009) (blue dashed line) UVB models for emission from star forming galaxies and quasars are also shown for the rescaled 80-1024 model. The Lyα forest observations are from Kirkman *et al.* (2007), Kim *et al.* (2007) and Danforth *et al.* (2016). *Right:* The H I photo-ionisation rate, $\Gamma_{-13} = \Gamma_{\rm HI}/10^{-13}{\rm s}^{-1}$, evolution with redshift for the HM12 (black solid line), HM01 (red triple-dot dashed line) and Faucher-Giguère *et al.* (2009) (blue dashed line) UVB models. The observational measurements are from Scott *et al.* (2002); Kollmeier *et al.* (2014); Gaikwad *et al.* (2017a); Viel *et al.* (2017b) and Fumagalli *et al.* (2017). The green dot-dashed line is the best-fit from Shull *et al.* (2015).

(e.g. Rauch *et al.*, 1997).

In Figure 2.2 (left panel), the $\tau_{\rm eff}$ evolution for a variety of sub-grid physics and UVB models are compared with Lyα forest observations. The results shown by the black curves use the HM12 UVB model, whereas the red triple-dot dashed and blue dashed curves are obtained by scaling the simulated optical depths to match the H I photo-ionisation rates in the earlier Haardt & Madau (2001, HM01) and Faucher-Giguère *et al.* (2009) UVB models for emission from star-forming galaxies and quasars. The evolution of $\tau_{\rm eff}$ in the 80-1024 model when using the HM01 UVB is in reasonable agreement with observational measurements from Kirkman *et al.* (2007) (except the dip at $z \simeq 1.4$) and Kim *et al.* (2007) at $1.7 < z < 2.0$, but underpredicts $\tau_{\rm eff}$ at $z < 0.4$. In contrast, the fiducial HM12 UVB predicts $\tau_{\rm eff}$ values that are too high, particularly $z < 1.5$; a closely related result was noted by Kollmeier *et al.* (2014) when analysing the H I CDDF. None of the UVB models is able to reproduce a $\tau_{\rm eff}$ evolution that is in good agreement with the more recent COS data from Danforth *et al.* (2016) at $z \leq 0.4$. There is also a difference between these data and the measurements from Kirkman *et al.* (2007) at $z \sim 0.4$, possibly due to systematic differences in the measurements and cosmic variance. The Faucher-Giguère *et al.* (2009) UVB is closer to

these data than HM12 at $z < 0.5$, but overpredicts $\tau_{\rm eff}$ at all redshifts including $z = 2$. Interestingly, the differences between models with different feedback implementations are small, indicating that it is the uncertain amplitude of the UVB rather than galactic feedback that is largely responsible for this discrepancy (see also figure 1 in Davé *et al.*, 2010).

This is further illustrated in the right panel of Figure 2.2 where observational estimates of the H I photoionisation rate, $\Gamma_{-13} = \Gamma_{\rm HI}/10^{-13}{\rm s}^{-1}$, are compared to the three UVB models. The measurements by Shull *et al.* (2015); Gaikwad *et al.* (2017a) and V17, based on an analysis of the COS Lyα CDDF, are in mutual agreement and predict photo-ionisation rates at $z < 0.4$ intermediate between HM01 and HM12. The value proposed by Kollmeier *et al.* (2014) (cyan triangle) lies very close to the HM01 UVB at $z = 0.1$. The red inverted triangles with large error bars display earlier constraints on $\Gamma_{\rm HI}$ obtained from the proximity effect by Scott *et al.* (2002). The blue rectangle corresponds to the recent, independent constraint from Fumagalli *et al.* (2017) using observations of Hα fluorescence from H I in a nearby galactic disk (see also Adams *et al.*, 2011).

Differing assumptions regarding the relative contributions of star forming galaxies and quasars and their spectral shape are largely responsible for differences between existing UVB models. Given these considerable differences, efforts to calibrate the H I photoionisation rate to match $\tau_{\rm eff}$ and CDDF measurements at $z < 0.4$ (e.g. Khaire & Srianand, 2015; Madau & Haardt, 2015), as well as renewed attempts to obtain measurements of $\Gamma_{\rm HI}$ in the redshift interval $0.4 < z < 2$, are desirable.

2.3 Voigt profile analysis

We now proceed to present the results of the Voigt profile analysis of our mock Lyα forest spectra. We fit lines at three redshifts, $z = [0.1,\ 1,\ 1.6]$. When comparing simulations to each other or to data compilations that have a range of resolution and signal-to-noise properties, the mock spectra are post-processed by convolving them with an instrument profile with a Full Width Half Maximum (FWHM) of $7\ {\rm km\,s^{-1}}$ and rebinned to a pixel size of $3\ {\rm km\,s^{-1}}$. A uniform Gaussian distributed noise is added

with a signal-to-noise of S/N$= 50$ per pixel. The mean transmission of the spectra are rescaled to match $\tau_{\rm eff} = [0.012, 0.043, 0.086]$ at $z = [0.1, 1, 1.6]$. These values correspond to the 80-1024 model $\tau_{\rm eff}$ evolution for the HM01 UVB for emission from star forming galaxies and quasars, which is in good agreement with the Kirkman *et al.* (2007) and Kim *et al.* (2007) $\tau_{\rm eff}$ measurements in the left panel of Figure 2.2.

The exception to this is when we directly compare the simulations to the V17 COS measurements of the CDDF and the velocity width distribution at $z = 0.1$. In this case, we follow V17 and convolve the spectra with the LF1 G130M COS line spread function including scattering at wavelength 1350 Å[1]. The spectra are rebinned to pixels of $\sim 7.2\,{\rm km\,s^{-1}}$ and a Gaussian distributed signal-to-noise of S/N$= 30$ per resolution element (or equivalently ~ 20 per pixel) is then added. The effective optical depth is scaled to $\tau_{\rm eff} = 0.021$ ($\langle F \rangle = 0.979$). This corresponds to the value V17 required to match the observed CDDF in the range $10^{13} \leq N_{\rm HI}/{\rm cm^{-2}} \leq 10^{14}$.

The COS observations of the CDDF and velocity width distribution at $z = 0.1$ are as described by V17; further details regarding the data reduction and AGN spectra can also be found in Wakker *et al.* (2015) and Kim et al. (in prep). The data comprises of 704 H I lines within column densities $10^{12.5} \leq N_{\rm HI}/{\rm cm^{-2}} \leq 10^{14.5}$ with a total redshift path length of $\Delta z = 4.991$, covering the Lyα forest at $0 < z < 0.2$. The Voigt profile fits are obtained using Lyα absorption only.

The fitting of Voigt profiles to the mock Lyα spectra is performed with VPFIT (Carswell & Webb, 2014), which deconvolves the (already convolved) mock spectra with the instrument profile to obtain intrinsic line widths. Importantly, this approach matches that used to fit the COS observational data at $z = 0.1$. A total path length of $10^5 h^{-1}{\rm cMpc}$ is fitted for each model in segments of $20h^{-1}{\rm cMpc}$ to obtain our simulated line lists. All lines within $50\,{\rm km\,s^{-1}}$ of the start and end of each segment are ignored to avoid spurious line fits due to edge effects. Finally, to estimate the sample variance in the COS observational data, we adopt the approach of Rollinde *et al.* (2013) and bootstrap resample the mock spectra with replacement over the observed path length $\Delta z = 4.991$. The sampling is performed 1000 times over the total simulated path length of $10^5 h^{-1}\,{\rm cMpc}$.

[1] `http://www.stsci.edu/hst/cos/performance/spectral_resolution/`

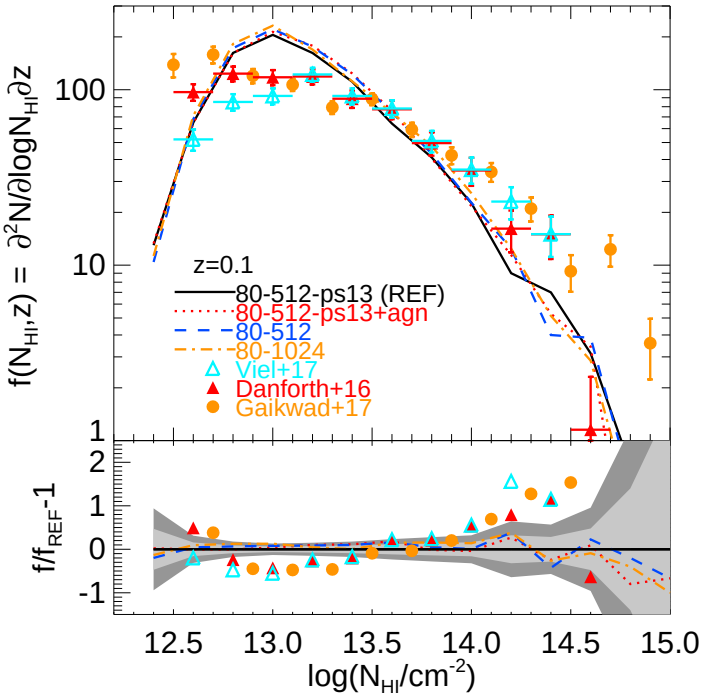


Figure 2.3: The H I column density distribution function at $z = 0.1$ after scaling the mock spectra to a mean transmission $\langle F \rangle = 0.979$. Three of the models use different prescriptions for following cold, dense gas and galactic feedback: QUICKLYA (blue dashed curve), multi-phase star formation and energy driven winds (black solid curve) and with the addition of AGN feedback (red dotted curve). The fourth model (80-1024) uses QUICKLYA but has increased mass resolution. The observational data points are from Danforth *et al.* (2016) (red triangles), Gaikwad *et al.* (2017a) (orange circles) and V17 (cyan triangles). Only absorption lines with a relative error less than 50 per cent on the column density are used. The lower panel shows the simulations and COS observations relative to the reference model 80-512-ps13. The grey shaded areas display the sample variance estimate, corresponding to the 68 and 95 per cent confidence intervals when bootstrap resampling over a redshift path length of $\Delta z = 4.991$.

2.3.1 The CDDF

Figure 2.3 displays the comparison between the CDDF, defined as the number of absorbers per unit log column density per unit redshift, $f(N_{\rm HI}, z) = \partial^2 N / \partial \log N_{\rm HI} \partial z$, from the Sherwood models and the COS observations described by V17 at $z = 0.1$ (see also figure 1 in V17). Note that only the 80-512-ps13+agn model was examined in detail by V17; in this work we present a comparison of the additional Sherwood models in which star formation, feedback and numerical resolution have been changed while other parameters remain fixed. We also display the independent measurements of the CDDF from Danforth *et al.* (2016) (red triangles) and Gaikwad *et al.* (2017a) (orange circles), although we caution that differences in the line fitting methodologies used in these studies will bias any direct comparison with our simulations.

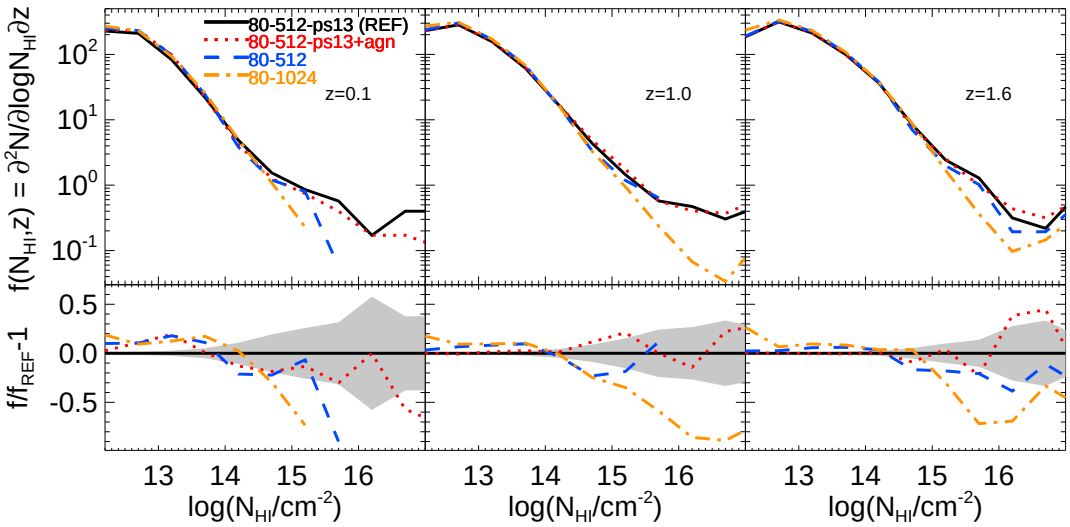


Figure 2.4: *Upper panels:* The Lyα forest column density distribution function at $z = 0.1,\ 1,\ \mathrm{and}\ 1.6$. The models shown here are the same as in Figure 2.3, except now the spectra are post-processed to have higher resolution ($\mathrm{FWHM} = 7\,\mathrm{km\,s^{-1}}$) and signal-to-noise ($\mathrm{S/N} \sim 50$). Only lines with relative error less than 50 per cent on the column density are used. *Lower panels:* The CDDF relative to the reference model, 80-512-ps13. The grey shaded area shows the Poisson error for the reference model.

The simulations fail to capture the correct number of absorbers at $N_{\rm HI} < 10^{13.2}\,\mathrm{cm^{-2}}$, by as much as a factor ~ 2 at $10^{13}\,\mathrm{cm^{-2}}$. Note that the simulations are well converged with mass resolution – this may be assessed by comparing the 80-512 (blue dashed curve) and 80-1024 (orange dot-dashed curve) models. However, the CDDF is very sensitive to the signal-to-noise and spectral resolution at low column densities (cf. Figure 2.4 where S/N$= 50$ and FWHM=$7\,\mathrm{km\,s^{-1}}$), and the observational data are incomplete at $N_{\rm HI} < 10^{13}\,\mathrm{cm^{-2}}$. This discrepancy therefore reflects differences between the true noise on the data and the idealised, uniform noise added to the mock spectra and is probably not significant. In contrast, the agreement between the V17 data and simulations at $10^{13.2} < N_{\rm HI}/\mathrm{cm^{-2}} < 10^{14}$ is within the 2σ uncertainty from sample variance, shown by the grey shading in the lower panel. At $N_{\rm HI} > 10^{14}\,\mathrm{cm^{-2}}$, however, the number of absorbers are underpredicted by a factor ~ 2 and the slope of the observed CDDF is shallower than the simulated prediction. A similar discrepancy was present in the recent analysis by Shull *et al.* (2015) using simulations performed with the Eulerian hydrodynamical code ENZO, as well as in the study by Gurvich, Burkhart & Bird (2017) with the moving mesh code AREPO, suggesting this discrepancy is not unique to P-GADGET-3 simulations. In contrast Gaikwad *et al.* (2017b) recently found better

agreement with the CDDF at $N_{\rm HI} > 10^{14}\,{\rm cm}^{-2}$ using GADGET-2 adiabatic hydrodynamical simulations post-processed to incorporate radiative cooling, photo-heating and ionisation. Note, however, the effect of gas pressure on the H I distribution will not be correctly captured in these models, complicating interpretation of this result.

Lastly, it is clear that the various feedback scenarios explored by the simulations impact very little overall on the CDDF at low column densities, particularly at $N_{\rm HI} < 10^{14}\,{\rm cm}^{-2}$. Outflows have a similarly small impact on the low column Lyα forest at $z > 2$; these systems are associated with the diffuse IGM rather than circumgalactic gas (Theuns *et al.*, 2002b; Viel, Schaye & Booth, 2013a, and see Section 2.4). Any differences between the feedback models are within the expected 1σ sample variance.

This is further emphasised in Figure 2.4 where we examine the Lyα absorption systems at column densities $10^{12.2} \leq N_{\rm HI}/{\rm cm}^{-2} \leq 10^{17}$ at $z = [0.1,\, 1.0,\, 1.6]$. Note that we adopt S/N$= 50$ per pixel and a instrument resolution ${\rm FWHM} = 7\,{\rm km\,s}^{-1}$ here. The lower panels display the residual with respect to the 80-512-ps13 model, and grey shading shows the Poisson error. The QUICKLYA method (80-512, blue dashed-line) agrees well with the more sophisticated sub-grid physics models for weak absorption systems with $N_{\rm HI} < 10^{13.5}\,{\rm cm}^{-2}$ at $z = 0.1$ and $N_{\rm HI} < 10^{14.5}\,{\rm cm}^{-2}$ at $z = 1.6$. However, higher column density lines are either underpredicted or absent relative to the other models. Multi-phase star formation and stellar feedback (80-512-ps13, black curve) results in a factor of 2-5 more absorption systems at $N_{\rm HI} \gtrsim 10^{14}\,{\rm cm}^{-2}$. A similar result was noted by Bolton *et al.* (2017) for the CDDF at $2 < z < 3$, although the H I column density threshold where QUICKLYA underpredicted the CDDF was higher, $N_{\rm HI} \simeq 10^{14.5-15}\,{\rm cm}^{-2}$. The lack of $N_{\rm HI} \gtrsim 10^{14}\,{\rm cm}^{-2}$ absorbers is in part because of missing cold dense gas in the QUICKLYA model, but also because winds redistribute gas into the diffuse IGM and introduce peculiar velocities that can increase the equivalent widths of the lines (Davé *et al.*, 2010; Meiksin, Bolton & Tittley, 2015).

Finally, including AGN feedback in the Sherwood models yields similar results for the CDDF relative to the stellar feedback only model, except at $z = 0.1$ where the incidence of high column density systems is slightly lower (although the total number of absorbers here is small). A stronger effect was noted by Gurvich, Burkhart & Bird (2017), who found that the more vigorous AGN feedback in the Illustris simulation

suppresses the CDDF at $N_{\rm HI} = 10^{14}$–$10^{15}\,{\rm cm}^{-2}$ by a factor of two due to changes in the density and temperature of the gas associated with these absorbers. The higher temperatures reduce the Lyα opacity by lowering the radiative recombination rate and (for $T \gtrsim 10^5\,{\rm K}$) collisionally ionising the gas. In contrast, Tepper-García *et al.* (2012, see their figure C1) find stellar and AGN feedback have a negligible effect on the CDDF at $z = 0.25$ using simulations drawn from the OWLS project (Schaye *et al.*, 2010). These differences likely reflect variations in the sub-grid physics, as the precise impact of feedback will depend on how efficiently gas is ejected from dark matter haloes.

In contrast to the present study, Tepper-García *et al.* (2012) also found reasonably good agreement with the H I CDDF measurement at $10^{14} \leq N_{\rm HI}/{\rm cm}^{-2} \leq 10^{14.5}$ from Lehner *et al.* (2007) based on an earlier compilation of FUSE (*Far Ultraviolet Spectroscopic Explorer*, FWHM$\sim 20\,{\rm km\,s}^{-1}$) and HST/STIS (*Space Telescope Imaging Spectrograph*, FWHM$\sim 7\,{\rm km\,s}^{-1}$) observations at $z \lesssim 0.4$. However, the models in Tepper-García *et al.* (2012) underpredicted the incidence of saturated lines at $N_{\rm HI} \sim 10^{14.5}\,{\rm cm}^{-2}$; their Ly$\alpha$ only line fits underestimated the column density of these absorbers since the Lehner *et al.* (2007) HST/STIS data are obtained from Lyα and higher order Lyman lines. The Lehner *et al.* (2007) H I CDDF furthermore only includes absorbers with velocity widths $b_{\rm HI} < 40{\rm km\,s}^{-1}$ and relative errors less than 40 per cent on $N_{\rm HI}$ and $b_{\rm HI}$ (i.e. figure 14 in Lehner *et al.*, 2008). We have confirmed we obtain similar agreement with the Lehner *et al.* (2007) CDDF measurements and our simulations (for ${\rm S/N} = 50$ and FWHM=7 ${\rm km\,s}^{-1}$) to that obtained by Tepper-García *et al.* (2012) when selecting only absorbers with $b_{\rm HI} < 40\,{\rm km\,s}^{-1}$.

2.3.2 The velocity width distribution

We next turn to consider the distribution of Lyα line velocity widths, $b_{\rm HI}$. Figure 2.5 displays a comparison between the V17 COS measurements and simulations at $z = 0.1$. We again show the independent measurements from Danforth *et al.* (2016) (red triangles) and Gaikwad *et al.* (2017a) (orange circles) for comparison. Overall, the models slightly underpredict the incidence of broad lines at $b_{\rm HI} = 40$–$60\,{\rm km\,s}^{-1}$ and overpredict at $b_{\rm HI} < 30{\rm km\,s}^{-1}$, although generally the data lie within the expected 95

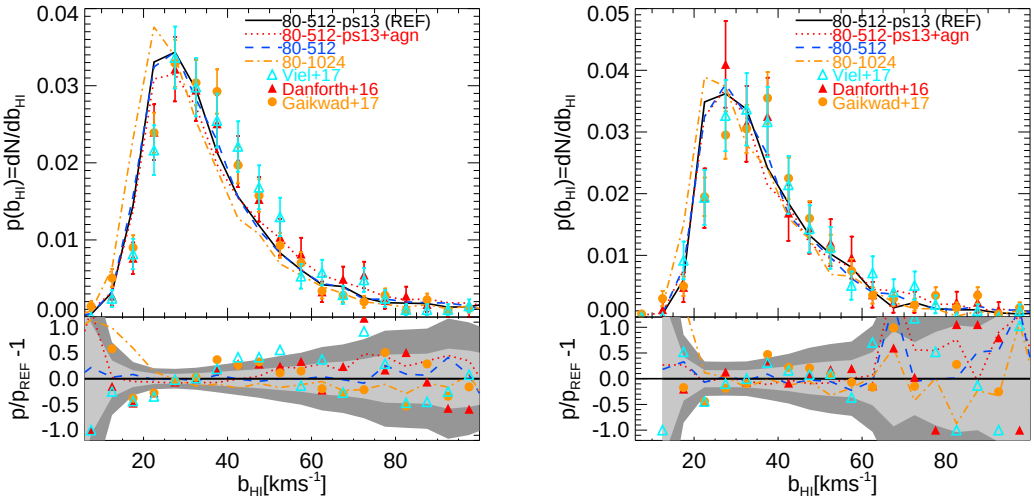


Figure 2.5: *Left:* The Lyα velocity width distribution at $z = 0.1$ after scaling the mock spectra to a mean transmission $\langle F \rangle = 0.979$. The observational data points are from Danforth *et al.* (2016) (red triangles), Gaikwad *et al.* (2017a) (orange circles) and V17 (cyan triangles). Only lines with $N_{\rm HI} = 10^{13}$–$10^{14}\,{\rm cm}^{-2}$ and a relative error less than 50 per cent on the velocity widths are included. The lower panel shows the simulations and COS observations relative to the reference model 80-512-ps13. The grey shaded areas display the sample variance estimate, corresponding to the 68 and 95 per cent confidence intervals when bootstrap resampling over a redshift path length of $\Delta z = 4.991$. *Right:* As for left, but now for lines with $N_{\rm HI} = 10^{13.5}$–$10^{14}\,{\rm cm}^{-2}$ are included.

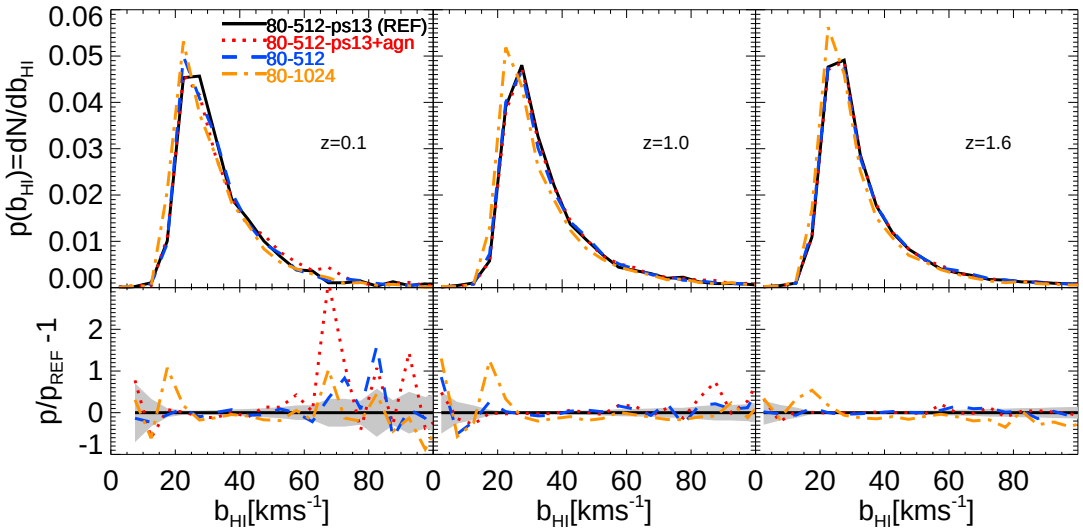


Figure 2.6: The Lyα forest velocity width distribution at $z = 0.1$, 1, and 1.6. The curves are as for Figure 2.4. *Lower panels:* The velocity width distribution relative to the reference model, 80-512-ps13. Only lines with $N_{\rm HI} = 10^{13}$–$10^{14}\,{\rm cm}^{-2}$ and a relative error less then 50 per cent on velocity widths are used. The grey shaded area shows the Poisson error for the reference model.

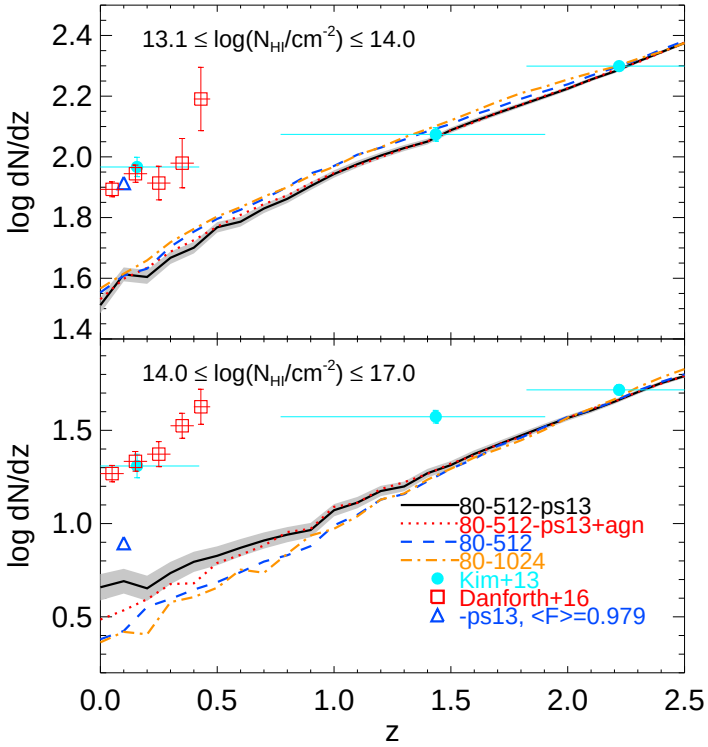


Figure 2.7: Redshift evolution in the number of Lyα absorbers per unit redshift for a subset of the simulations. Absorbers with column densities $10^{13.1} \leq N_{\rm HI}/{\rm cm}^{-2} < 10^{14}$ (top-panel) and $10^{14} \leq N_{\rm HI}/{\rm cm}^{-2} \leq 10^{17}$ (bottom-panel) are shown. The observational data points with Poisson error bars are from Danforth *et al.* (2016) (open red squares) and a data compilation presented by Kim *et al.* (2013) (filled cyan circles, see text for details). The blue triangles show the 80-512-ps13 model rescaled to $\langle F \rangle = 0.979$ at $z = 0.1$. The grey shaded area shows the Poisson errors for the 80-512-ps13 model.

per cent scatter arising from sample variance in the reference model. It is important to note, however, that unlike the CDDF (where the effect of feedback is comparable to or smaller than the effect of mass resolution) the line widths are not well converged with mass resolution (see also Chapter 3 later). The distribution from the 80-1024 simulation (orange dot-dashed curve) differs significantly from the 80-512 model (blue dashed curve), particularly at $b_{\rm HI} \lesssim 30\,{\rm km\,s^{-1}}$, with a median value of $30.8{\rm km\,s^{-1}}$ (cf. $33.5{\rm km\,s^{-1}}$ for the 80-512 model and $36.2{\rm km\,s^{-1}}$ for the COS data). Higher resolution simulations will therefore predict line widths that are narrower than observed. As pointed out by V17, this suggests there may be additional physics that broadens the absorption lines that is not incorporated into the simulations at present. Note however, the difference between the simulations and the COS data at $b_{\rm HI} \lesssim 30\,{\rm km\,s^{-1}}$, could mostly be contributed to by the low column density systems. Since, such systems are affected by resolution and signal-to-noise, we decided to apply a cut on $N_{\rm HI}$, that

$N_{\rm HI} = 10^{13.5} - 10^{14.0}\,{\rm cm}^{-2}$. The results are shown in the right panel of Figure 2.5. We found formally the agreement with the data improves at $b_{\rm HI} \lesssim 20\,{\rm km\,s}^{-1}$ and at $b_{\rm HI} \gtrsim 40\,{\rm km\,s}^{-1}$, but this is due to low number statistics. However, the discrepancy still remains, as the simulations produce a systematically narrower $b_{\rm HI}$ distribution compared to data.

We may nevertheless still examine the relative difference between the different feedback models. The incorporation of multi-phase star formation and supernovae-driven winds (black curve) makes very little difference compared to the QUICKLYA model. The addition of AGN feedback (red dotted curve) also has a small effect, increasing the number of broad lines at $b_{\rm HI} > 50\,{\rm km\,s}^{-1}$ with a median[2] b-parameter $35.3{\rm kms}^{-1}$.

In comparison to earlier work, Davé *et al.* (2010) also reported a small difference of $\sim 1{\rm km\,s}^{-1}$ in the median $b_{\rm HI}$ values predicted by their constant wind and momentum-driven wind models at $z = 0$. However, their velocity widths are generally higher then we find here, with a median value of $\sim 43{\rm km\,s}^{-1}$. The mass resolution of their simulations is around factor of two higher than this work ($M_{\rm gas} = 2.49 \times 10^7 h^{-1} M_\odot$) although performed in smaller volumes $(48h^{-1}\,{\rm cMpc})^3$. This difference is therefore most likely because Davé *et al.* (2010) do not deconvolve their Voigt profile fits with the instrument profile (see the first paragraph in section 4 of that paper). Tepper-García *et al.* (2012) similarly find that AGN feedback produces a small increase in the typical Lyα line widths at $z = 0.25$ using the OWLS simulations, and report a median b-parameter of $29.4\,{\rm km\,s}^{-1}$ from mock spectra with FWHM=$7{\rm km\,s}^{-1}$ and a S/N$= 50$ per pixel. This is similar to the value of $27.7{\rm km\,s}^{-1}$ we obtain from our AGN feedback (80-512-ps13+agn) model using the same signal-to-noise and instrument resolution. As Tepper-García *et al.* (2012) also use SPH simulations performed at slightly lower mass resolution compared to this work ($M_{\rm gas} = 8.7 \times 10^7 h^{-1} M\odot$), their line widths will be similarly under-resolved. More recently, Gaikwad *et al.* (2017b) also found their simulated velocity width distribution predicts lines that are narrower than the COS data. It is possible that the lack of any coupling between radiative cooling, photo-ionisation and the hydrodynamical response of the gas in their simulations may

[2]This is consistent with V17, who reported an increase by roughly $2\ {\rm km\,s}^{-1}$ in the median b-parameter when including AGN feedback. Note that V17 incorrectly reported this quantity as the peak of the velocity width distribution rather than the median.

exaggerate this difference further, however.

The impact of feedback on the velocity distribution at $z = [0.1,\ 1.0,\ 1.6]$ is displayed in Figure 2.6, for FWHM$= 7\,\mathrm{km\,s^{-1}}$ and $\mathrm{S/N} = 50$ per pixel. Again it is clear that the velocity width distribution is not converged with mass resolution. By comparing the 80-1024 (orange dot dashed line) and 80-512 (blue dashed line) the line widths differ significantly at $b_{\rm HI} < 30\,\mathrm{km\,s^{-1}}$. This implies a comparison between simulations and observations requires a mass resolution of at least $m_{\rm gas} \simeq 6 \times 10^6 h^{-1} M_\odot$. However, as for the CDDF, the simulations with varying sub-grid physics performed at the same mass resolution are very similar. The only exception is at $z = 0.1$ when hot gas from AGN feedback produces slightly broader lines.

2.3.3 The evolution of number density of absorbers

Lastly we examine the number of H I absorbers per unit redshift, dN/dz. Figure 2.7 displays dN/dz for low ($10^{13.1} \leq N_{\rm HI}/\mathrm{cm^{-2}} \leq 10^{14}$, upper panel) and high ($10^{14} < N_{\rm HI}/\mathrm{cm^{-2}} \leq 10^{17}$, lower panel) column density absorbers, overlaid with a compilation[3] of observational data from Kim *et al.* (2013). In this instance we do not attempt to match the resolution and signal-to-noise of the simulations to the data compilation, which was obtained with a variety of instruments. We instead use FWHM$= 7\,\mathrm{km\,s^{-1}}$ and S/N$= 50$ per pixel and assume the HM01 UVB for emission from star forming galaxies and quasars. We also show the more recent COS measurements[4] from Danforth *et al.* (2016) at $0 \leq z \leq 0.47$. These are formally consistent with the earlier data compilation at $z \leq 0.3$, but with an increased incidence of lines at $0.3 < z < 0.5$. Note also we use Lyα only fits for comparison to the observations, which may complicate the comparison to the stronger, saturated lines with column densities inferred using higher order Lyman lines. We have therefore tested this by also directly integrating the

[3]The individual measurements are from Hu *et al.* (1995); Lu *et al.* (1996); Kim *et al.* (1997); Kirkman & Tytler (1997); Savaglio *et al.* (1999); Kim, Cristiani & D'Odorico (2001); Sembach *et al.* (2004); Williger *et al.* (2006); Aracil *et al.* (2006); Janknecht *et al.* (2006); Lehner *et al.* (2007); Williger *et al.* (2010).

[4]Note the Danforth *et al.* (2016) measurements in the upper panel of Fig. 2.7 are for the slightly different column density range $10^{13} \leq N_{\rm HI}/\mathrm{cm^{-2}} \leq 10^{14}$, rather than $10^{13.1} \leq N_{\rm HI}/\mathrm{cm^{-2}} \leq 10^{14}$ used for the Kim *et al.* (2013) data compilation.

H I number densities along the simulated sight-lines to obtain dN/dz (see also Gurvich, Burkhart & Bird, 2017). This procedure yields similar results to the Voigt profile fits.

The number of low column density Lyα forest absorbers (top panel) is not sensitive to the differences in star formation and feedback prescriptions in the models. This is consistent with the CDDF, where galactic winds and AGN feedback do not significantly impact on the gas distribution at the low column densities that probe the diffuse IGM (see also Davé *et al.*, 2010). The simulations are in good agreement with the observational data at $z > 1$, but underpredict the number of weak lines at $z = 0.1$. To investigate this further, we have rescaled the mean transmission in the 80-512-ps13 model to $\langle F \rangle = 0.979$ at $z = 0.1$ (blue triangle), which V17 find provides a better match to CDDF at $10^{13} < N_{\rm HI}/{\rm cm}^{-2} < 10^{14}$. The improved agreement again demonstrates this discrepancy is due to the uncertain UVB amplitude; the HM01 model overpredicts the H I photo-ionisation rate at $z \lesssim 0.5$.

In contrast to the low column density systems, the simulated predictions for higher column density Lyα forest absorbers exhibit some differences with the choice of star formation and feedback model at $z < 1.5$. The 80-512-ps13 model produces a factor of ~ 2 higher dN/dz relative to 80-512 at $z \simeq 0$, with the AGN feedback intermediate between the two. However, all models fail to reproduce the observational data at $z \leq 1.5$. Rescaling the mean transmission at $z = 0.1$ slightly improves agreement but does not remove the discrepancy. In combination with the CDDF, this strongly suggests the simulations are not correctly capturing the saturated Lyα absorption systems that are still optically thin to Lyman continuum radiation.

2.4 Identifying the gas responsible for low redshift Lyα forest absorbers

In order to more closely examine the physical origin of the absorption in our models and assess the effect of feedback, we consider the typical temperature and density of gas in the QUICKLYA model (80-512) and the Puchwein & Springel (2013) energy

Table 2.2: A comparison of baryon phases in the simulations with different treatments for cold, dense gas and feedback at $z = 0\,, 0.1$ and 1.6 where $\Delta_{\rm th} = 97.2,\ 65.9$ and 62, respectively. The percentage of the total gas mass is divided into four categories following Davé *et al.* (2010).

Name	Model	Diffuse	WHIM	Hot Halo	Condensed	Stars
		$\Delta < \Delta_{\rm th}, T < 10^5{\rm K}$	$\Delta < \Delta_{\rm th}, T > 10^5{\rm K}$	$\Delta > \Delta_{\rm th}, T > 10^5{\rm K}$	$\Delta > \Delta_{\rm th}, T < 10^5{\rm K}$	
$z = 0.1$	80-512	36.5	21.3	17.1	0.9	24.2
	80-512-ps13	36.6	24.3	22.4	9.1	7.7
	80-512-ps13+agn	36.5	36.9	20.0	3.3	3.3
$z = 1.0$	80-512	51.7	15.4	12.6	1.9	18.4
	80-512-ps13	51.9	17.0	16.3	10.6	4.3
	80-512-ps13+agn	51.6	19.2	17.7	8.5	3.0
$z = 1.6$	80-512	61.8	11.3	8.9	2.8	15.1
	80-512-ps13	62.0	12.3	11.3	11.5	2.8
	80-512-ps13+agn	62.0	12.7	11.7	11.1	2.4

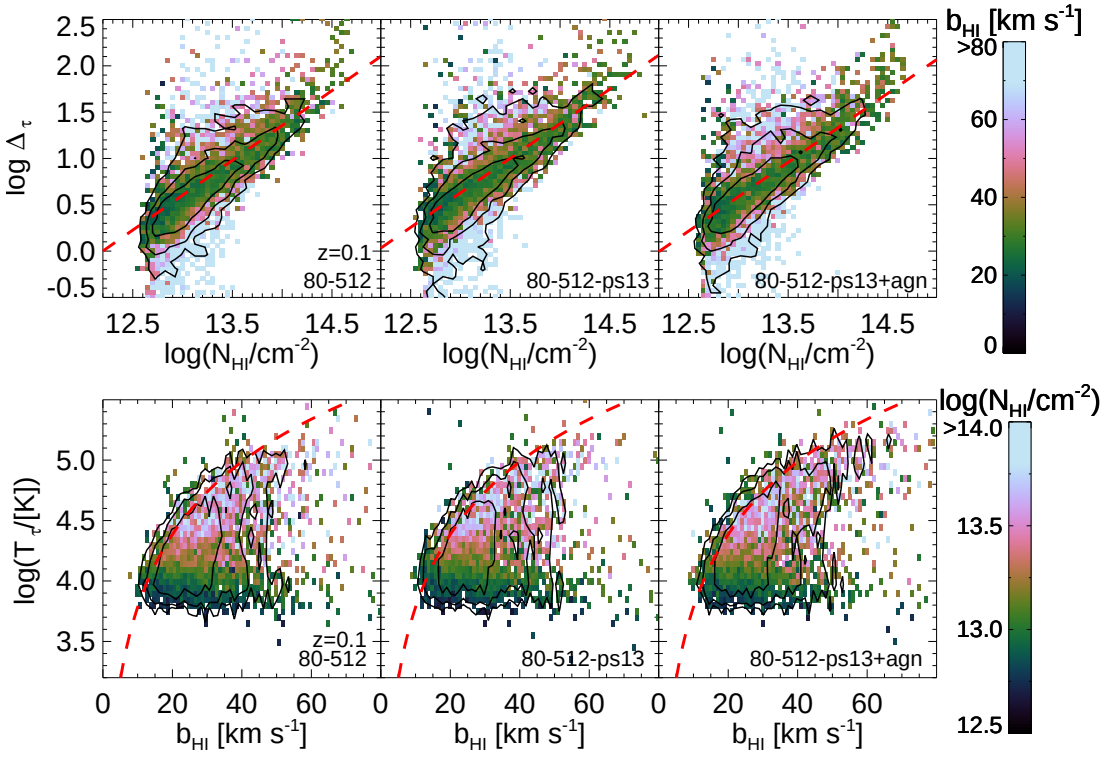


Figure 2.8: *Upper panel:* The optical depth weighted normalised gas density against the H I column density for simulations with different prescriptions for feedback at $z = 0.1$ (from left to right, QUICKLYA, stellar feedback and stellar+agn feedback). The colours display the median velocity widths of the absorbers in each cell, and the black contours enclose 50, 75 and 90 per cent of total number of absorbers. Only data points with relative errors on the velocity widths and H I column densities less then 50 per cent are shown. The red dashed line shows the analytical model of Schaye (2001), evaluated at the gas temperature and H I photo-ionisation rate used in the simulation (see Eq. 2.1). *Lower panel:* The optical depth weighted gas temperature against the Lyα velocity widths, $b_{\rm HI}$. The colours now correspond to the median H I column density in each cell and the red dashed line shows the relationship between T and $b_{\rm HI}$ for pure thermal broadening, given by Eq. (2.2).

driven winds model with (80-512-ps13+agn) and without (80-512-ps13) AGN feedback. We have divided the gas into four categories based on temperature, $T_{\rm th} = 10^5$ K, and normalised density thresholds, $\Delta_{\rm th}$, following Davé *et al.* (2010). These are i) diffuse gas ($\Delta < \Delta_{\rm th}, T < 10^5$K) ii) the warm-hot IGM (WHIM, $\Delta < \Delta_{\rm th}, T > 10^5$K) iii) hot halo gas ($\Delta > \Delta_{\rm th}, T > 10^5$K, and iv) condensed gas ($\Delta > \Delta_{\rm th}, T < 10^5$K). In Table 2.2, the percentage of the total baryon mass in each category is shown at $z = 0.1,\ 1$ and 1.6 where $\Delta_{\rm th} = 97.2,\ 65.9$ and 62, respectively (here $\Delta_{\rm th}$ is computed using equations 1 and 2 in Davé *et al.*, 2010). We have also included the percentage of gas that has been converted into collsionless star particles.

The redshift evolution of gas in the diffuse phase is very similar for all models, with no noticeable difference due to feedback. This diffuse gas follows a power law temperature-density relationship, $T = T_0 \Delta^{\gamma-1}$ (see Figure 2.1). However, there is a significant in-

crease in the mass fraction in the WHIM for the model with AGN feedback at $z = 0.1$, with a corresponding decrease in the condensed phase fraction and stellar mass. Including multi-phase star formation and stellar feedback produces more gas in the hot halo and condensed phases compared to the QUICKLYA model at $z = 0.1$. In contrast, the QUICKLYA model produces significantly more stars at $z \leq 1$ and – while capturing the diffuse IGM reasonably well – will produce unreliable results for gravitationally bound gas at $\Delta > \Delta_{\rm th}$.

The mass fractions for the 80-512-ps13 model are broadly similar to the "vzw" momentum driven winds model described in Davé *et al.* (2010), with slightly more (~ 5 per cent) gas in the dense phases with $\Delta > \Delta_{\rm th}$. There is also reasonable agreement between the 80-512-ps13 model and the post-processed adiabatic simulations described by Gaikwad *et al.* (2017a) at $z = 0$, with around 4 per cent more (less) gas in the WHIM (hot halo) phase. This suggests the bulk of the hot gas with $T > 10^5\,{\rm K}$ in the models without AGN feedback is produced by gravitational infall. The largest difference is the condensed phase which contains 18.8 per cent of the mass at $z = 0$ in Gaikwad *et al.* (2017a); this is because dense gas is not converted into stars in their adiabatic simulations.

The connection between the density and temperature of the gas and the column density and velocity widths of the Lyα absorbers at $z = 0.1$ is summarised in Figure 2.8. Along each simulated line of sight we have computed the optical depth weighted temperature, T_τ, and density, Δ_τ, where $X_{\tau,{\rm j}} = \sum_{\rm i} \tau_{\rm i,j} X_{\rm i} / \sum_{\rm i} \tau_{\rm i,j}$ and $\tau_{\rm i,j}$ is optical depth at the $i^{\rm th}$ pixel in real space contributing to the $j^{\rm th}$ pixel in velocity space (Schaye *et al.*, 1999). We then associate T_τ and Δ_τ with $N_{\rm HI}$ and $b_{\rm HI}$ at the location of the line centres identified by VPFIT. This approach takes redshift space distortions due to the peculiar motion of the gas into account. As before, following V17 we only consider systems with relative errors less then 50 per cent on $b_{\rm HI}$ and $N_{\rm HI}$.

The top panel of Figure 2.8 displays the relationship between $N_{\rm HI}$ and Δ_τ in the simulations. The data are coloured according to their velocity widths. The red dashed line shows the power-law relationship between $N_{\rm HI}$ and Δ predicted by Schaye (2001), assuming the typical size of an H I absorber is the local Jeans scale:

$$N_{\rm HI} = \frac{2.44\times10^{13}\,{\rm cm}^{-2}}{\Gamma_{-13}}\left(\frac{\Delta}{10}\right)^{3/2}\left(\frac{T_4}{2}\right)^{-0.26}\left(\frac{1+z}{1.1}\right)^{9/2}. \quad (2.1)$$

Here $\Gamma_{-13} = \Gamma_{\rm HI}/10^{-13}\,{\rm s}^{-1}$ is the H I photo-ionisation rate (where $\Gamma_{-13} = 0.78$ at $z = 0.1$ in the 80-512-ps13 simulation for $\langle F\rangle = 0.979$) and $T_4 = T/10^4\,{\rm K}$ is the gas temperature.

This provides a good description of the scaling between gas density and H I column density (see also Davé *et al.*, 1999, 2010; Tepper-García *et al.*, 2012). The majority of the absorption lines at $N_{\rm HI} = 10^{13}$–$10^{14}\,{\rm cm}^{-2}$ correspond to gas densities $\Delta = 4$–40 in the simulations (V17), with typical velocity widths of $b_{\rm HI} = 20$–$40\,{\rm km\,s}^{-1}$. In all models there are a small number of broad lines, $b_{\rm HI} > 40\,{\rm km\,s}^{-1}$, with column densities $N_{\rm HI} = 10^{12.5}$–$10^{13.5}\,{\rm cm}^{-2}$ that are associated with hot $T \sim 10^5\,{\rm K}$ gas in the WHIM with $\Delta \simeq 1$–100 (see also Tepper-García *et al.*, 2012). The effect of feedback on the diffuse, low column density gas is rather subtle; there are slightly more broad lines lying above the $N_{\rm HI} - \Delta_\tau$ correlation for the AGN feedback model, consistent with additional heating. Although there is significantly more hot gas in the WHIM by mass at $z = 0.1$ when including AGN feedback, much of this is also collisionally ionised. In all instances, however, the higher column density systems, $N_{\rm HI} > 10^{14}\,{\rm cm}^{-2}$ correspond to gas densities at $\Delta \gtrsim 20$. The simulations fail to correctly capture the number density of these systems, some of which are at densities associated with circumgalactic gas.

The lower panel in Figure 2.8 shows the corresponding values of T_τ at the line centres against the velocity widths. The red dashed line displays the expected velocity width under the assumption of pure thermal broadening:

$$b_{\rm HI} = 18.2\,{\rm km\,s}^{-1}\left(\frac{\rm T_4}{2}\right)^{1/2}. \quad (2.2)$$

In general, although the minimum line widths trace the expectation for thermal broadening, most of the absorbers are significantly broader, particularly for low column density lines originating from low density gas (see also Garzilli, Theuns & Schaye, 2015, for a recent discussion at $z \sim 3$). Many of the absorbers are therefore broadened through the additional effects of gas pressure (i.e. Jeans smoothing). The absorbers

with $N_{\rm HI} = 10^{13}$–$10^{14}\,{\rm cm}^{-2}$ are associated with gas with a broad range of temperatures, but most are in the range $T = 10^4$–$10^{4.5}\,{\rm K}$. The velocity widths of these lines remain too narrow with respect to the COS data. Again, the effect of stellar and AGN feedback on the temperature of the absorbers is small.

2.5 Conclusions

We have investigated the impact of different feedback prescriptions on the properties of the low redshift Lyα forest, using a selection of hydrodynamical simulations drawn from the Sherwood simulation suite. The simulations adopt stellar feedback, AGN feedback and a simplified scheme for modelling the low column density Lyα forest that converts all gas with $\Delta > 1000$ and $T < 10^5\,{\rm K}$ into collisionless star particles. We have examined the CDDF, velocity width distribution, the redshift evolution in the line number density, dN/dz, and the relationship between the column density, velocity widths, and the underlying gas density and temperature.

Our analysis confirms the finding by V17 that the velocity widths of simulated Lyα absorption lines with gas densities $\Delta = 4$–40 are too narrow when compared with COS data. We also stress that this difference will be exacerbated further for simulations performed at higher mass resolution than considered here; the line widths are underresolved at our fiducial resolution of $M_{\rm gas} = 5.1 \times 10^7 h^{-1} M_\odot$ (see also Chapter 3). We also find that absorbers with column densities $N_{\rm HI} > 10^{14}\,{\rm cm}^{-2}$, which correspond to gas with $\Delta \gtrsim 20$ in our simulations, are underestimated, in agreement with earlier work (Shull *et al.*, 2015; Gurvich, Burkhart & Bird, 2017).

On the other hand, using simulations that vary the feedback prescription while keeping other parameters fixed, we find that the impact of galactic winds and AGN feedback is generally very modest. AGN feedback only impacts on the Lyα absorbers at very low redshift, $z = 0.1$, by producing some broader lines and slightly reducing the incidence of systems with $N_{\rm HI} > 10^{14}{\rm cm}^{-2}$ with respect to a model with only stellar feedback. There is no noticeable impact on the CDDF due to stellar or AGN feedback at $N_{\rm HI} < 10^{14}\,{\rm cm}^{-2}$. Furthermore, we find a simplified scheme that ignores feedback and star formation altogether adequately capture the properties of absorption lines with

$N_{\rm HI} < 10^{14}\,{\rm cm}^{-2}$, although the incidence of stronger systems is underestimated compared to models that include feedback. Similarly, the Lyα line number density and its evolution with redshift, dN/dz, is in good agreement with observational data for low column density systems, $10^{13.1} \leq N_{\rm HI}/{\rm cm}^{-2} \leq 10^{14}$, once the amplitude of the UVB is rescaled to match the CDDF. In contrast, for high column density systems, $10^{14} \leq N_{\rm HI}/{\rm cm}^{-2} \leq 10^{17}$, the simulations underpredict the incidence of absorbers at $z = 0.1$ and $z = 1$ by a factor of $\simeq 2.2$ and 3, respectively.

This demonstrates that stellar and AGN feedback – as currently implemented in our simulations – have a limited impact on the Lyα forest. We conclude that resolving the discrepancy between COS data and the simulations requires an increase in the temperature of gas with $\Delta = 4$–40, either through (i) additional He II photo-heating at $z > 2$, (ii) additional fine-tuned feedback that ejects overdense gas into the IGM at just the right temperature for it to still contribute significantly to the Lyα forest or alternatively (iii) a larger, currently unresolved turbulent component to the line widths (Oppenheimer & Davé, 2009; Iapichino, Viel & Borgani, 2013; Gaikwad *et al.*, 2017b). Note, however, the first possibility would require a UVB with a harder spectrum at $z > 2$, potentially producing gas temperatures that are too high with respect to existing observational constraints from the Lyα forest at $1.6 \leq z \leq 3$ (Becker *et al.*, 2011; Boera *et al.*, 2014; Bolton *et al.*, 2014). Our results provide further motivation for studying the impact of state-of-the-art feedback models on the properties of the low redshift Lyα forest.

Chapter 3

Resolving the Lyα forest in hydrodynamical simulations at redshifts $z < 2$

In this chapter, the numerical convergence of various statistical properties of the low redshift ($z \leq 2$) Lyα forest in the Sherwood simulation suite is presented. Most of the quantities are introduced in Chapter 2, and majority of this chapter is published as an appendix in Nasir *et al.* (2017). The aim is to quantify the uncertainties imposed by the hydrodynamical simulations due to mass resolution and box size on these statistical quantities, which are widely used in the Lyα forest absorption line studies. Similar recent studies at higher redshifts, $2 < z < 5$ can be found in Lukić *et al.* (2015) and Bolton *et al.* (2017)

The outline of the chapter is as follows. In Section 3.1, the results of the Voigt profile fitting analysis are discussed, which is complementary to the results presented in Chapter 2. Furthermore, the convergence for the effective optical depth, flux probability distribution function (PDF) and flux power spectrum are shown in Section 3.2. Finally, the gas temperatures are presented in Section 3.3. The simulations used in this chapter are listed in Table 3.1.

Table 3.1: The hydrodynamical simulations used in this chapter. The first column uses the naming convention *L-N-param*. Here L is the box size in units of $h^{-1}\mathrm{cMpc}$ and N is the cube root of the total number of gas particles. The remaining columns give the mass of each dark matter and gas particle in $h^{-1}M_{\odot}$ and the gravitational softening length in $h^{-1}\mathrm{ckpc}$.

Name	M_{dm} $[h^{-1}M_{\odot}]$	M_{gas} $[h^{-1}M_{\odot}]$	l_{soft} $[h^{-1}\mathrm{ckpc}]$
80-512	2.75×10^8	5.10×10^7	6.25
80-1024	3.44×10^7	6.38×10^6	3.13
80-256	2.20×10^9	4.08×10^8	12.50
40-512	3.44×10^7	6.38×10^6	3.13
20-256	3.44×10^7	6.38×10^6	3.13

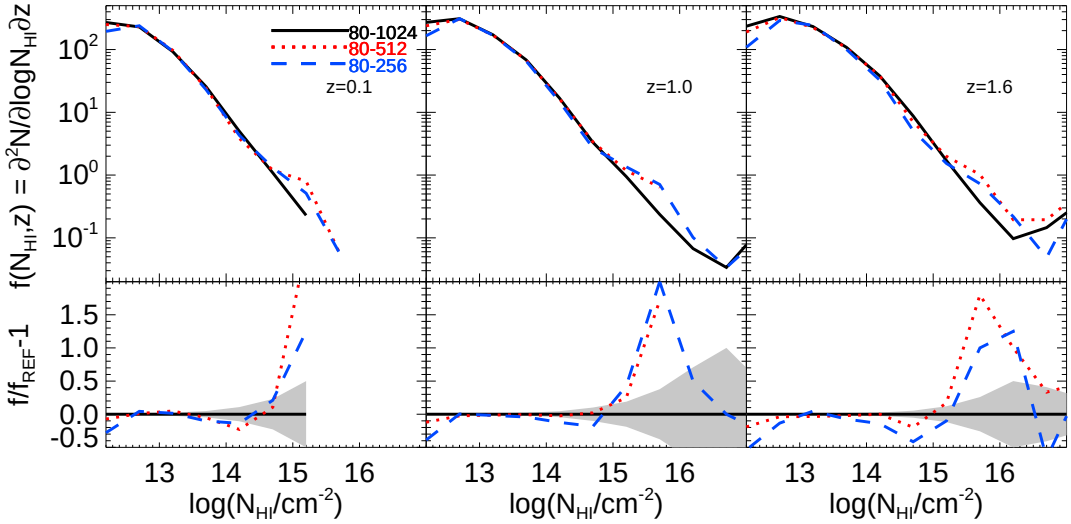


Figure 3.1: The Lyα forest CDDF at $z = 0.1,\ 1,$ and 1.6. Convergence with mass resolution for a fixed box size of $80h^{-1}\mathrm{cMpc}$ is displayed. Only column densities with a relative error less than 50 per cent are used. The lower panel displays the models with respect to the reference model 80-1024. The grey shaded areas are the Poisson errors on the reference model.

3.1 Voigt profile fitting

First, the convergence with mass resolution and box size for the line fitting results from Chapter 2 are examined. A signal-to-noise $S/N = 50$ per pixel and FWHM of 7 $\mathrm{km\,s^{-1}}$ is assumed. The Lyα CDDF and velocity width distribution at $z = [0.1,\ 1,\ 1.6]$ are displayed through Figures 3.1-3.4.

As shown in Figure 3.1-3.2, the CDDF is well converged with mass resolution and box size within the range $10^{12.7} \leq N_{\mathrm{HI}}/\mathrm{cm}^{-2} \leq 10^{14}$. However, at $N_{\mathrm{HI}} > 10^{14}\,\mathrm{cm}^{-2}$ ($N_{\mathrm{HI}} < 10^{12.7}\,\mathrm{cm}^{-2}$) the number of lines are over (under) estimated at lower mass resolution. This suggests that numerical resolution is unlikely to be the cause of the discrepancy between the COS observations and our simulations at $N_{\mathrm{HI}} > 10^{14}\,\mathrm{cm}^{-2}$

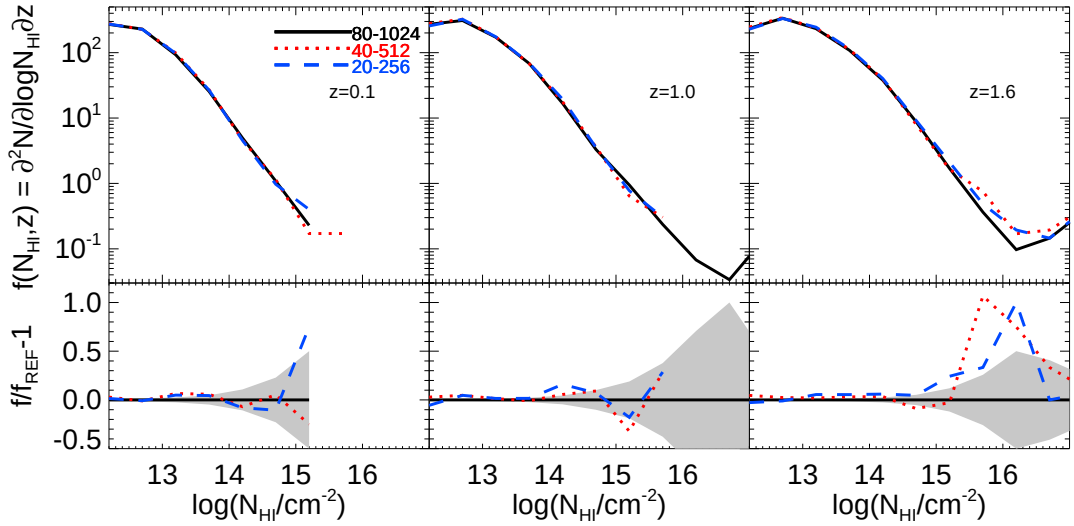


Figure 3.2: As for Figure 3.1, but now convergence with box size for a fixed mass resolution of $M_{\rm gas} = 6.38 \times 10^6 h^{-1} M_\odot$ is displayed.

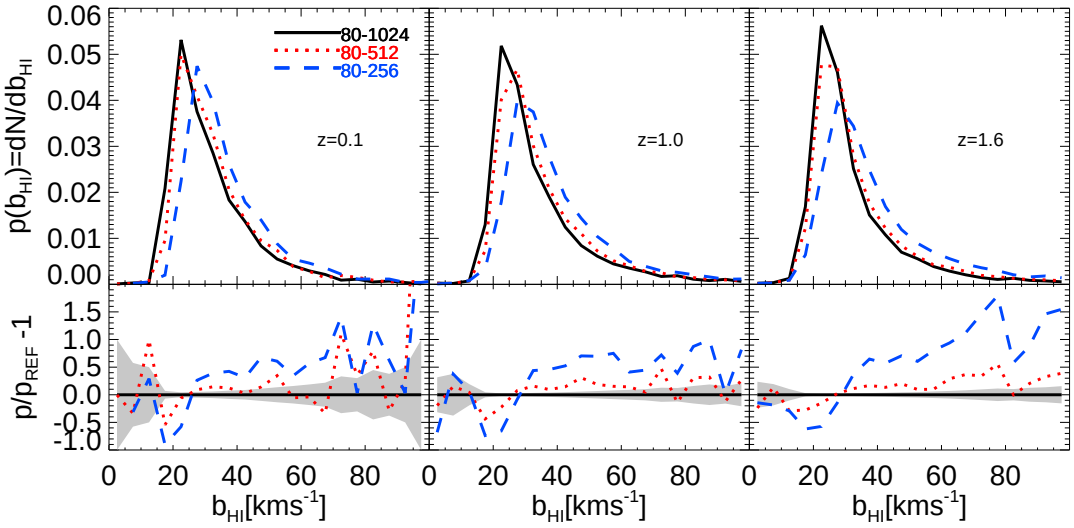


Figure 3.3: The Lyα velocity width distribution at $z = 0.1$, 1, and 1.6. Convergence with mass resolution for a fixed box size of $80h^{-1}$cMpc is displayed. Only lines with $N_{\rm HI} = 10^{13}$–$10^{14}\,{\rm cm}^{-2}$ and a relative error less than 50 per cent on the velocity widths are used. The lower panel displays the models with respect to the reference model 80-1024. The grey shaded areas are the Poisson errors on the reference model.

(see Chapter 2).

For comparison, Tepper-García *et al.* (2012) also report that the H I CDDF is well converged using the OWLS simulations at $z = 0.25$. They found that the H I CDDF is well converged within the range $10^{12.5} \leq N_{\rm HI}/{\rm cm}^{-2} \leq 10^{14}$ for a mass resolution of $M_{\rm gas} = 8.7 \times 10^7 h^{-1} M_\odot$.

However, in Figure 3.3, it is clear that mass resolution significantly impacts on the velocity width distributions, with line widths that are systematically overestimated at our fiducial resolution of $M_{\rm gas} = 5.1 \times 10^7 h^{-1} M_\odot$ (80-512). A mass resolution of at

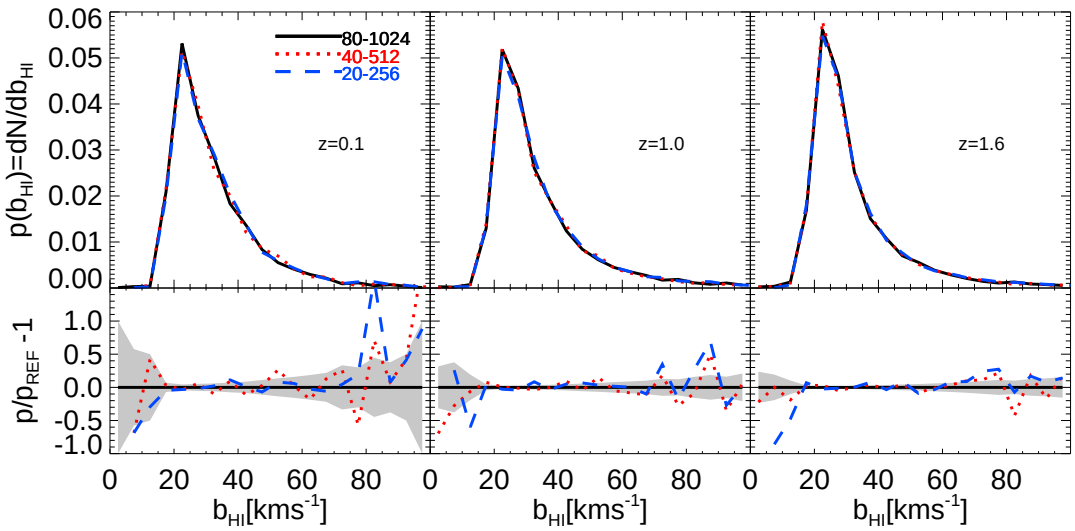


Figure 3.4: As for Figure 3.3, but now convergence with box size for a fixed mass resolution of $M_{\rm gas} = 6.38 \times 10^6 h^{-1} M_\odot$ is displayed.

least $M_{\rm gas} = 6.4 \times 10^6 h^{-1} M_\odot$ is required for an acceptable level of convergence. This means the discrepancy between the COS observations of the velocity width distribution in Chapter 2 will be even larger for higher resolution simulations. The Lyα line width distribution is generally well converged with box size, as shown Figure 3.4, with the exception of lines at $b_{\rm HI} < 20 {\rm km\,s^{-1}}$ in the $20 h^{-1}\,{\rm cMpc}$ box. Again, similar results are reported by Tepper-García *et al.* (2012).

3.2 Transmitted flux statistics

The convergence of the effective optical depth, $\tau_{\rm eff}$, at $z \leq 2$ is displayed in Figure 3.5. The $\tau_{\rm eff}$ is converged within $\sim 2\%$ with box size and $\sim 5\%$ with mass resolution for the fiducial 80-512 model.

The transmitted flux PDF obtained from the simulations are shown through Figure 3.6-3.7. Figure 3.6 shows the convergence of the flux PDF with mass resolution. The PDF is converged within 20% for the 80-512 model and is slightly better converged at $z = 1.6$, where proportionally more of the absorption is due to gas at mean density. The convergence with box size (Figure 3.7) is at $\sim 5\%$ level.

The convergence of the transmitted flux power spectrum with box size and mass resolution is presented in Figures 3.8 and 3.9. The flux power spectrum shows convergence up to $\sim 5\%$ with box size as shown in Figure 3.8. Note that the difference at low k-

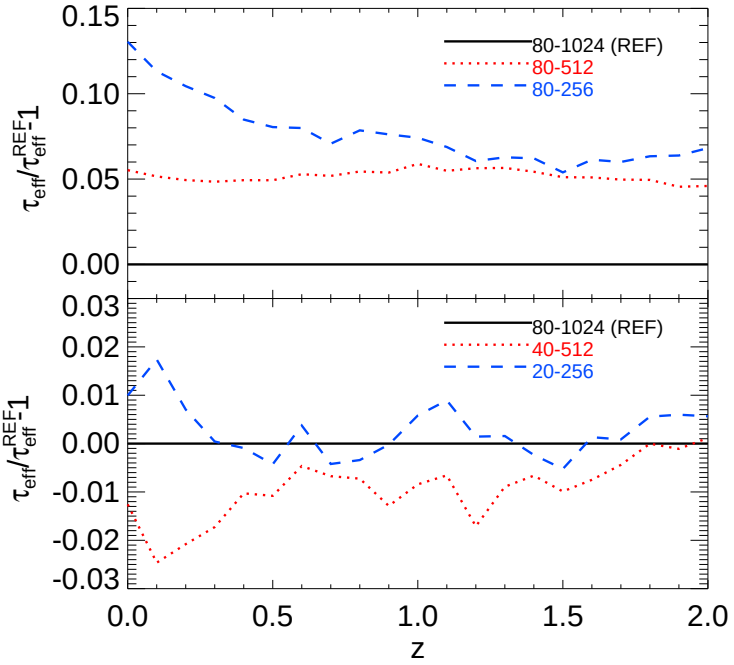


Figure 3.5: The effective optical depth relative to the reference model 80-1024 against redshift. *Top:* Convergence with mass resolution for a fixed box size $80h^{-1}\mathrm{cMpc}$. *Bottom:* Convergence with box size for a fixed mass resolution $M_{\mathrm{gas}} = 6.38 \times 10^6 h^{-1} M_{\odot}$.

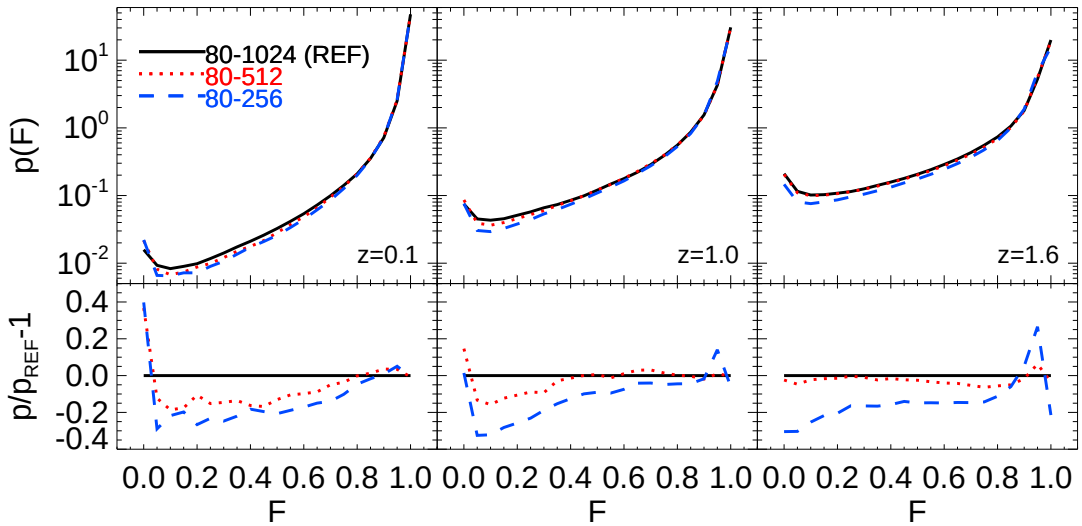


Figure 3.6: The PDF of the Lyα transmitted flux at $z = 0.1,\ 1,$ and 1.6. Convergence with mass resolution for a fixed box size of $80h^{-1}\mathrm{cMpc}$ is displayed. The lower panel displays the models with respect to the reference model 80-1024.

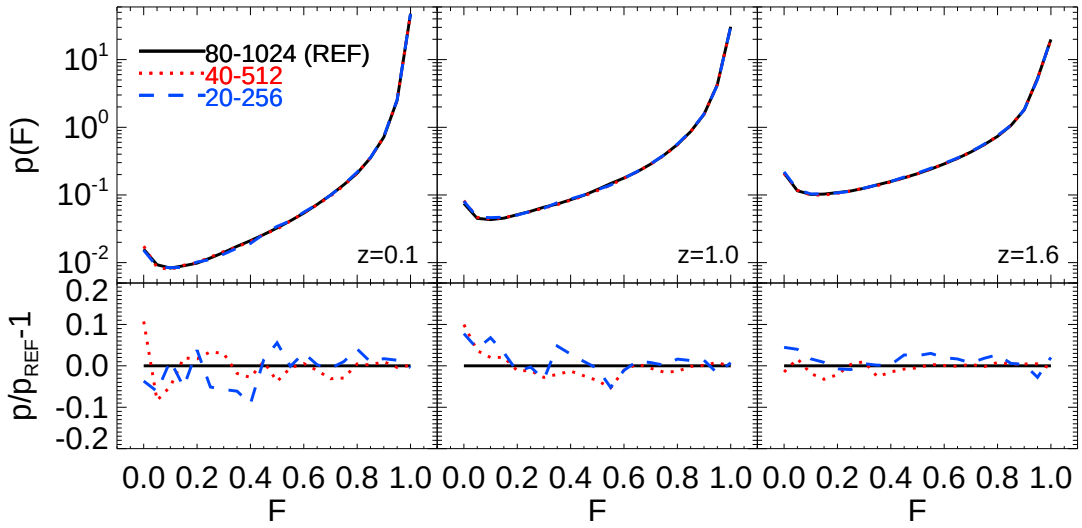


Figure 3.7: As for Figure 3.6, but now convergence with box size for a fixed mass resolution of $M_{\rm gas} = 6.38 \times 10^6 h^{-1} M_\odot$ is displayed.

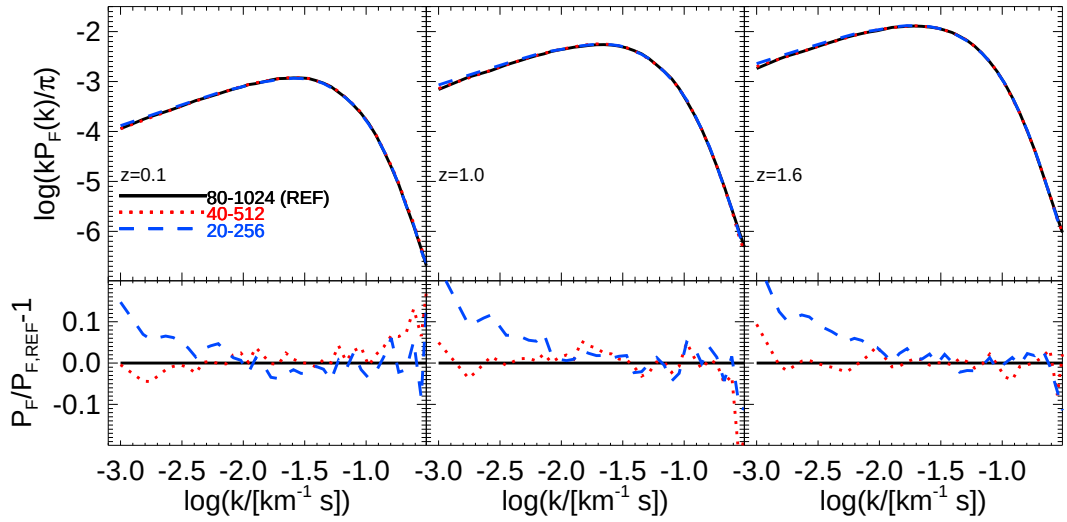


Figure 3.8: The power spectrum of transmitted flux at three different redshifts indicated in each panel. Here each plot gives convergence with box size for fixed mass resolution $M_{\rm gas} = 6.38 \times 10^6 h^{-1} M_\odot$. The lower panel displays the models with respect to the reference model 80-1024.

scales is due to difference, in the box size and hence the maximum physical scale that can be probed by the models. By contrast, the flux power spectrum shows convergence up to $20 - 30\%$ with mass resolution at scales $\log k/(\mathrm{km}^{-1}\,\mathrm{s}) < -0.5$, for the fiducial model as shown in Figure 3.9.

3.3 Temperature and slope of $T - \Delta$ relation

Finally, Figure 3.10 and Table 3.2 display convergence tests for the volume weighted IGM thermal state with box size and mass resolution. The results are well converged

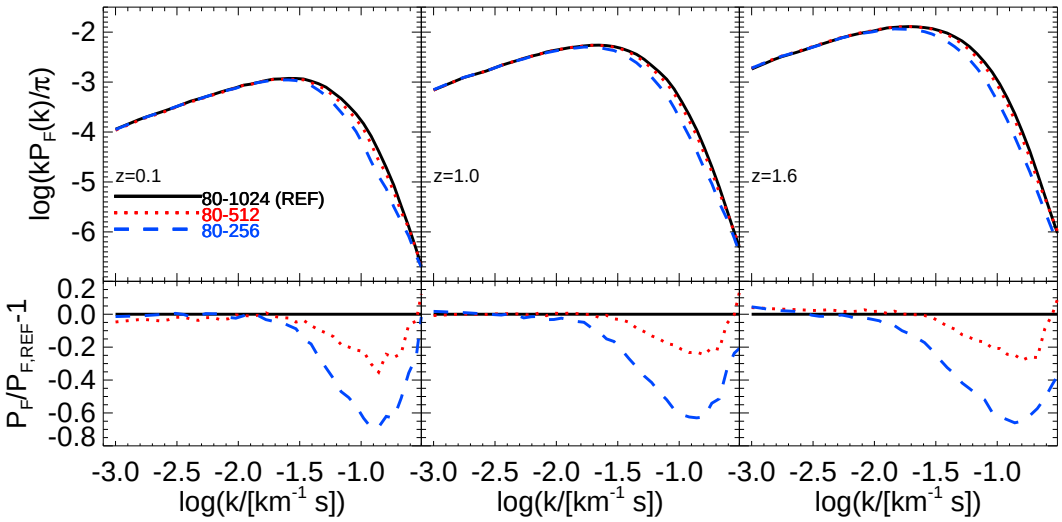


Figure 3.9: As for Figure 3.8 but now convergence with mass resolution is displayed for a fixed box size of $80h^{-1}\mathrm{cMpc}$. The lower panel displays the models with respect to the reference model 80-1024.

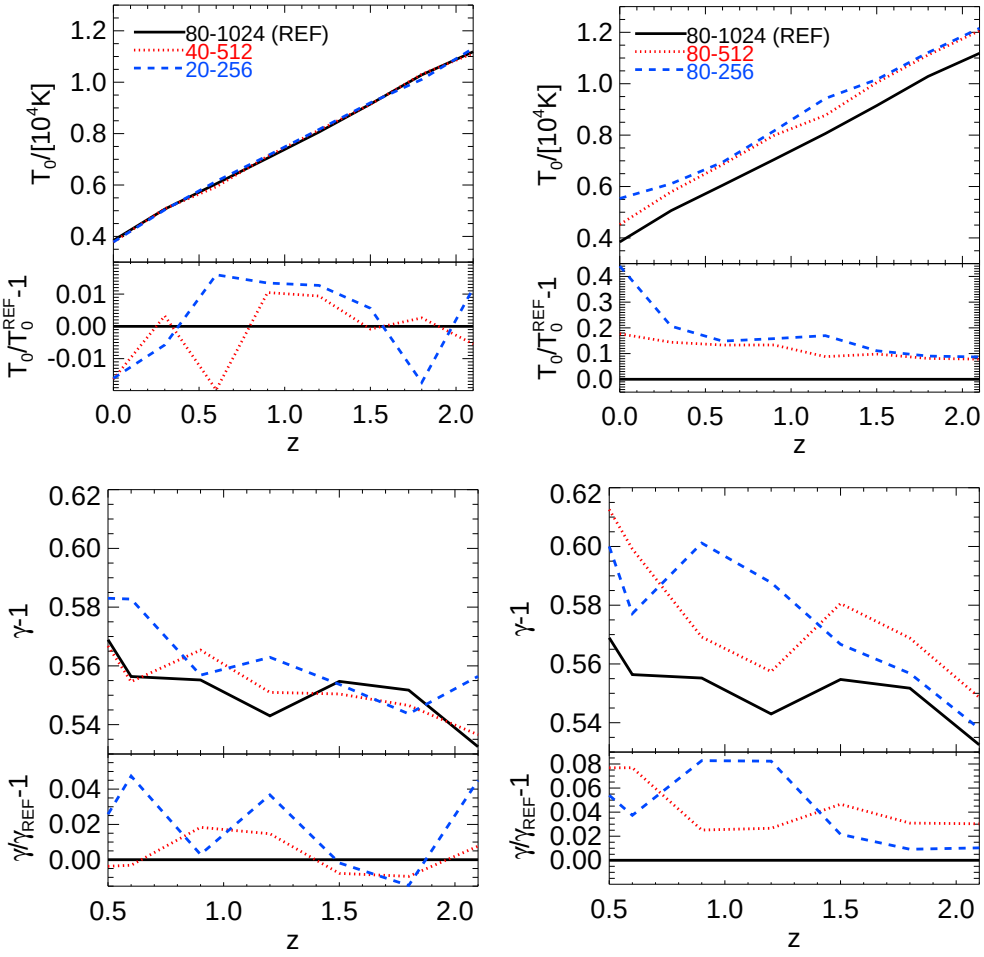


Figure 3.10: The temperature at mean density T_0 (top panels), and the slope of the temperature-density relation $\gamma - 1$ (bottom panels). Convergence with box size for a fixed mass resolution of $M_{\mathrm{gas}} = 6.38 \times 10^6 h^{-1} M_\odot$ (left column) and for mass resolution at a fixed box size of $80h^{-1}\mathrm{cMpc}$ is displayed (right column).

Table 3.2: A comparison of baryon phases in the simulations showing models with different box size and mass resolution at $z = 0\,, 0.1$ and 1.6 where $\Delta_{\rm th} = 97.2,\ 65.9$ and 62, respectively. The percentage of the total gas mass is divided into four categories following Davé *et al.* (2010) (see also Chapter 2).

Name	Model	Diffuse	WHIM	Hot Halo	Condensed	Stars
		$\Delta < \Delta_{\rm th}, T < 10^5{\rm K}$	$\Delta < \Delta_{\rm th}, T > 10^5{\rm K}$	$\Delta > \Delta_{\rm th}, T > 10^5{\rm K}$	$\Delta > \Delta_{\rm th}, T < 10^5{\rm K}$	
$z = 0.1$	80-1024	35.0	20.1	15.3	0.7	28.8
	80-512	36.5	21.3	17.1	0.9	24.2
	80-256	39.7	22.6	20.0	1.2	16.6
	40-512	34.6	20.5	15.3	0.8	28.8
	20-256	35.3	19.4	15.2	0.7	29.3
$z = 1.0$	80-1024	49.6	14.5	11.1	1.6	23.2
	80-512	51.7	15.4	12.6	1.9	18.4
	80-256	55.4	16.4	14.9	2.1	11.2
	40-512	49.2	15.0	11.1	1.5	23.2
	20-256	49.7	13.5	11.5	1.6	23.7
$z = 1.6$	80-1024	59.3	10.7	7.7	2.3	20.0
	80-512	61.8	11.3	8.9	2.8	15.1
	80-256	65.7	12.3	10.6	2.9	8.4
	40-512	58.9	11.1	7.8	2.2	19.9
	20-256	59.2	10.2	7.9	2.3	20.4

with box size, but demonstrate the temperature of the IGM at mean density is overestimated by 10–20 per cent at our fiducial resolution (80-512). Although not shown, the *mass weighted* temperature obtained from the gas particles is well converged with mass resolution, suggesting this difference originates from the larger smoothing lengths used in the lower resolution models. Additionally, we observe from Table 3.2 that as mass resolution is increased using the QUICKLYA model, a greater proportion by mass of the baryons are converted to collisionless star particles. Note, however, this is already a significant overestimate, and the results of the QUICKLYA model will be unreliable for gas at $\Delta > \Delta_{\rm th}$.

3.4 Conclusions

In this chapter, the numerical convergence of various statistical quantities of the low redshift ($z \leq 2$) Lyα forest in the Sherwood simulations suite is presented. The CDDF is well converged for low density absorbers ($N_{\rm HI} > 10^{12.7}{\rm cm}^{-2}$) with mass resolution and box size, except at $N_{\rm HI} > 10^{14}{\rm cm}^{-2}$. By contrast, the mass resolution has a noticeable impact on the velocity widths, significantly overestimating the line widths at lower mass resolution.

The Lyα effective optical depth,$\tau_{\rm eff}$, shows excellent convergence within $\sim 2\%$ with box size and $\sim 5\%$ with mass resolution for our fiducial simulation (80-512). The flux PDF is converged within 20% for mass resolution and 5% for box size. The flux power spectrum shows convergence up to $\sim 5\%$ with box size but within 30% level with mass resolution at scales $\log k/({\rm km}^{-1}\,{\rm s}) < -0.5$.

In conclusion, resolving the Lyα forest at $z < 2$, requires a box size of $80h^{-1}{\rm cMpc}$ and a gas mass resolution of $M_{\rm gas} \leq 6.38 \times 10^6 h^{-1} M_{\odot}$, particularly for modelling the line widths and the flux power spectrum at scales $\log k/({\rm km}^{-1}\,{\rm s}) < -0.5$. This suggests that the discrepancy between the Lyα forest line widths at $z \sim 0.1$ measured by COS and numerical simulations will only be exacerbated with higher resolution models.

Chapter 4

Inferring the IGM thermal history during reionisation with the Lyman-α forest power spectrum at redshift $z \simeq 5$

4.1 Introduction

The intergalactic medium (IGM) probed by the Lyα forest of absorption lines is a valuable cosmic laboratory for studying the thermal and ionisation history of the Universe at redshifts $z \leq 7$. Observations of intergalactic absorption lines in high redshift quasar spectra indicate the first luminous sources had reionised the neutral hydrogen by $5.5 \leq z \leq 7$ and photo-heated the IGM to $\sim 10^4\,\mathrm{K}$ (Becker, Bolton & Lidz, 2015). The recently updated Thomson scattering optical depth reported by the Planck Collaboration *et al.* (2016b) is furthermore consistent with an instantaneous reionisation at $z_{\mathrm{re}} = 8.8 \pm 0.9$. In combination with other, complementary observations, these observations translate to an H I reionisation era that may have started as early as redshift $z \sim 12$ and ended by $z = 5.5$–6 (Robertson *et al.*, 2015; Bouwens *et al.*, 2015; Mitra, Choudhury & Ferrara, 2015).

Despite this progress, details regarding the precise timing and duration of reionisa-

tion remain elusive. One possible approach to clarifying this situation is measuring the energy deposited into the low density IGM by photo-heating during reionisation (Miralda-Escudé & Rees, 1994). At a redshift interval $\Delta z \simeq 1$–2 after reionisation the temperature of the low density ($\Delta = \rho/\bar{\rho} \leq 10$) IGM traced by the Ly$\alpha$ forest is expected to follow a power law relationship, $T = T_0 \Delta^{\gamma-1}$, parameterised in terms of the temperature at the mean cosmic gas density, T_0, and a slope, $\gamma - 1$ (Hui & Gnedin, 1997; McQuinn & Upton Sanderbeck, 2016). This temperature-density relation has been measured using a wide variety of techniques over the last two decades. These include analysing the velocity (Doppler) widths of Lyα absorption lines (Haehnelt & Steinmetz, 1998; Schaye *et al.*, 2000; Ricotti, Gnedin & Shull, 2000; McDonald *et al.*, 2001; Rudie, Steidel & Pettini, 2012; Bolton *et al.*, 2012, 2014), the suppression of small-scale power in the Lyα forest flux power spectrum (Zaldarriaga, Hui & Tegmark, 2001; Croft *et al.*, 2002; Zaroubi *et al.*, 2006; Viel *et al.*, 2013a), the probability distribution of wavelet amplitudes (Meiksin, 2000; Theuns & Zaroubi, 2000; Zaldarriaga, 2002; Lidz *et al.*, 2010; Garzilli *et al.*, 2012), the probability distribution of the transmitted Lyα forest flux (Lidz *et al.*, 2006; Bolton *et al.*, 2008; Calura *et al.*, 2012; Lee *et al.*, 2015), and the curvature of the Lyα forest transmission (Becker *et al.*, 2011; Boera *et al.*, 2014, 2016). The common element to almost all these studies is that they rely on mock Lyα forest spectra – typically drawn from cosmological hydrodynamical simulations – that can be compared directly to the observational data.

The bulk of these measurements are at redshifts $z < 4$ where high quality spectroscopic data are most readily available. These provide a valuable probe of photo-heating during the epoch of (likely quasar driven) He II reionisation around $z \simeq 3$ (McQuinn *et al.*, 2009; Compostella, Cantalupo & Porciani, 2014; Puchwein *et al.*, 2015). Importantly, however, the long cooling timescale of the low density IGM enables T_0 measurements at $z \simeq 5 - 6$ to be used as a probe of H I reionisation at $z > 6$ (Haehnelt & Steinmetz, 1998; Theuns *et al.*, 2002a; Hui & Haiman, 2003; Trac, Cen & Loeb, 2008; Cen *et al.*, 2009; Furlanetto & Oh, 2009; Lidz & Malloy, 2014; D' Aloisio, McQuinn & Trac, 2015). Indeed, recent studies have demonstrated observational measurements of T_0 at $z = 5$–6 are inconsistent with rapid ($\Delta z \simeq 2$) late H I reionisation occurring at $z \lesssim 8$ (Raskutti *et al.*, 2012; Upton Sanderbeck, D'Aloisio & McQuinn, 2016), although note this inference also depends on the typical spectral shape of the ionising sources during

reionisation.

A wide range of reionisation scenarios therefore remain consistent with these data, and their constraining power remains relatively limited. Furthermore, the absorption features in the Lyα forest are not only sensitive to the instantaneous thermal state of the gas set by the Doppler broadening of the lines in velocity space. The absorbing gas is also smoothed out in physical space by the increased gas pressure following reionisation, leading to additional broadening of the absorption features (i.e. Jeans smoothing, Gnedin & Hui, 1998; Hui & Rutledge, 1999; Theuns, Schaye & Haehnelt, 2000; Peeples *et al.*, 2010; Kulkarni *et al.*, 2015; Garzilli, Theuns & Schaye, 2015). The long dynamical timescale for low density intergalactic gas (comparable to a Hubble time, e.g. Schaye, 2001) means the precise degree of this pressure induced smoothing depends on the prior thermal (and hence reionisation) history. Consequently, the degeneracy between the Doppler broadening associated with the instantaneous gas temperature and the uncertain degree of pressure smoothing in the low density IGM is an important systematic for measurements of T_0 using the Lyα forest. It is furthermore a nuisance parameter when attempting to measure cosmological parameters and probe the nature of dark matter with the Lyα forest power spectrum (McDonald *et al.*, 2006; Zaroubi *et al.*, 2006; Viel *et al.*, 2013a; Palanque-Delabrouille *et al.*, 2015).

Analysis of the typical coherence scale of Lyα absorption transverse to the line of sight utilising close quasar pairs provides a promising way to directly measuring the pressure smoothing scale at $z \simeq 2$–3 (Rorai, Hennawi & White, 2013). However, the limited number of close pairs currently known at higher redshift prevents this method from being used at $z \simeq 5$, approaching the epoch of H I reionisation. The line of sight power spectrum of the transmitted flux at $z \simeq 5$ – a quantity widely studied at lower redshifts – provides a potential alternative. In common with other temperature diagnostics, the power spectrum is sensitive to *both* the instantaneous temperature and the prior thermal history. These smoothing scales may be disentangled to some extent with high resolution ($R \sim 40000$) spectra that probe wavenumbers $\log(k/\mathrm{km}^{-1}\,\mathrm{s}) \gtrsim -1$ (see e.g. Appendix D in Puchwein *et al.*, 2015). As the quantity of high resolution Lyα forest data available at $z \simeq 5$ has increased in the last few years (e.g. Becker *et al.*, 2015, with 7 additional quasar spectra at $z > 5.8$ and 16 at $4.5 < z < 5.4$),

a measurement of the cumulative energy deposited into the IGM, and hence tighter constraints on the thermal history during hydrogen reionisation may now be feasible (see also Lidz & Malloy, 2014).

In this work, we demonstrate that it is possible to constrain the integrated thermal history at $z > 5$ using the Lyα forest power spectrum measured from data sets that are now comparable in size to existing high resolution observational measurements. Recent studies have typically parameterised the integrated thermal history in Lyα forest models as either a characteristic filtering scale, $k_{\rm F}$, over which the gas is smoothed (e.g Rorai, Hennawi & White, 2013), or as the starting redshift of reionisation, $z_{\rm re}$, in optically thin hydrodynamical simulations (Viel *et al.*, 2013a). The former approach is well motivated, but in practice often treats the pressure smoothing scale as a free parameter that is decoupled from the reionisation history. The latter approach is not optimal either, as the parameter $z_{\rm re}$ does not uniquely define[1] the amount of energy deposited into the IGM as a function of time. In this work we propose instead that, aided by a suitable grid of hydrodynamical models, one may instead infer the cumulative energy per proton injected into a gas parcel during and soon after reionisation – a quantity which is more straightforward to connect directly to reionisation models.

The contents of this chapter are published in Nasir, Bolton & Becker (2016). The structure of this chapter is as follows. In Section 4.2, we present an overview of the hydrodynamical simulations used in this work and examine the typical scales on which thermal broadening and pressure smoothing act on the Lyα forest power spectrum at $z \simeq 5$. In Section 4.3, we examine the relationship between the gas density and Lyα forest transmission power spectra and the cumulative energy per proton injected into the IGM at mean density, u_0. In Section 4.4, we forecast how well observations might distinguish between different integrated thermal histories by examining mock datasets within a Bayesian statistical framework via a Markov Chain Monte Carlo (MCMC) analysis. We finally summarise our conclusions in Section 4.5. Throughout this chapter we refer to comoving Mpc and kpc as "cMpc" and "ckpc", respectively. A flat ΛCDM cosmology is adopted thoughout, with $\Omega_{\rm m} = 0.26$, $\Omega_\Lambda = 0.74$, $\Omega_{\rm b}h^2 = 0.023$, $\sigma_8 = 0.80$, $h = 0.72$ and $n_{\rm s} = 0.96$.

[1]For example, two reionisation models where $z_{\rm re}$ is identical but the spectral shape of the ionising sources is different will not have the same thermal history.

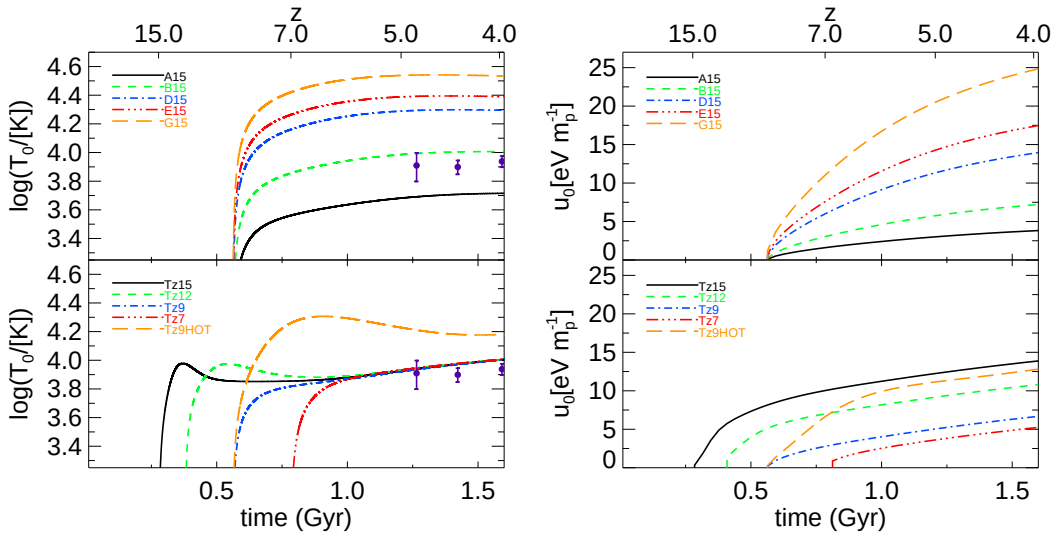


Figure 4.1: *Left:* The logarithm of the temperature at mean density, T_0, as function of time for a subset of the simulations listed in Table 4.1. The T_0 observational measurements from Becker *et al.* (2011), evaluated at their fiducial γ values along with 2σ errors, are shown by the filled circles. *Right:* The cumulative energy per proton deposited in a gas parcel at mean density (see Section 4.3 for details) as a function of time in the simulations.

4.2 Modelling the Lyα forest at $z \simeq 5$

4.2.1 Hydrodynamical simulations

In order to model Lyα forest spectra at $z \simeq 5$ we first require hydrodyanmical simulations with a variety of thermal histories. The models used in this work are summarised in Table 4.1, and are described in Becker *et al.* (2011) and Becker & Bolton (2013). Convergence tests with box size and mass resolution are presented in those papers and in Bolton & Becker (2009) (and also see Chapter 5).

In brief, the simulations were performed with the smoothed-particle hydrodynamics code P-GADGET-3, an updated version of the publicly available GADGET-2 (Springel, 2005). These simulations use a total of 2×512^3 dark matter and gas particles within a periodic $10h^{-1}\,\mathrm{cMpc}$ box. The initial positions and velocities of the particles at redshift $z = 99$ were generated using the P-GENIC initial conditions code (Springel *et al.*, 2005a) and the Eisenstein & Hu (1999) transfer function. In this work we neglect the impact of the small change in cosmological parameters required to match the more recent results reported by the Planck Collaboration *et al.* (2015), but expect that this will not affect our general conclusions. The baryons in the Lyα forest simulations are of primordial composition with a helium fraction by mass of $Y = 0.24$ (Olive

Table 4.1: The hydrodynamical simulations used in this work. All models have a box size of $10h^{-1}\,\mathrm{cMpc}$, 2×512^3 particles and a gas particle mass of $9.2 \times 10^4 h^{-1} M_\odot$. The columns in the table list the redshift of reionisation, $z_{\rm re}$, in the model, the scaling factors for the photoheating rates (see text for details), the logarithm of the temperature at mean density $\log T_0$, the slope of the temperature-density relation, γ, and the cumulative energy per proton, u_0, deposited into a gas parcel at mean density by $z = 4.9$. The values of $\log T_0$ and γ are estimated with a power-law fit to the volume weighted temperature-density plane.

Model	$z_{\rm re}$	ζ	ξ	$\log(\mathrm{T_0^{z=4.9}/K})$	$\gamma^{z=4.9}$	$u_0^{z=4.9}\,\mathrm{eV\,m_p^{-1}}$	References
A15	9	0.30	0.00	3.68	1.43	3.1	Table 2, Becker *et al.* (2011)
B15	9	0.80	0.00	3.98	1.46	5.9	
C15	9	1.45	0.00	4.16	1.47	8.7	
D15	9	2.20	0.00	4.28	1.48	11.5	
E15	9	3.10	0.00	4.38	1.47	14.5	
F15	9	4.20	0.00	4.47	1.47	17.8	
G15	9	5.30	0.00	4.53	1.48	20.9	
D13	9	2.20	-0.45	4.28	1.37	11.5	
D10	9	2.20	-1.00	4.26	1.08	11.5	
D07	9	2.20	-1.60	4.25	0.92	11.5	
Tz15	15	–	–	3.92	1.49	12.4	Appendix B, Becker & Bolton (2013)
Tz12	12	–	–	3.93	1.50	9.3	
Tz9	9	–	–	3.92	1.50	5.2	
Tz7	7	–	–	3.93	1.47	3.7	
Tz9HOT	9	–	–	4.21	1.52	11.3	

& Skillman, 2004). Any gas particles with an overdensity $\Delta > 10^3$ and temperature $T < 10^5\,\mathrm{K}$ are converted to collisionless star particles (Viel, Haehnelt & Springel, 2004b). The gas is also photo-ionised and heated by a spatially uniform metagalactic UV background (UVB) applied in the optically thin limit. The gas is assumed to be in ionisation equilibrium (Katz, Weinberg & Hernquist, 1996) using the recombination, ionisation and cooling rates listed in Bolton & Haehnelt (2007).

The UVB for the Becker *et al.* (2011) simulations is based on the Haardt & Madau (2001) synthesis model. This includes ionising emission from young star forming galaxies and quasars, and results in rapid reionisation at $z_{\rm re} = 9$. The photo-heating rates in most of these models have been rescaled to reproduce a range of temperature-density relations, such that $\epsilon_{\rm i} = \zeta \Delta^{\xi} \epsilon_{\rm i}^{\rm HM01}$, where $\epsilon_{\rm i}^{\rm HM01}$ are the Haardt & Madau (2001) photoheating rates for species $i = [\mathrm{H\,I},\ \mathrm{He\,I},\ \mathrm{He\,II}]$ and ζ, ξ are constants listed in Table 4.1. We also include five simulations from Becker & Bolton (2013). These have UVB models that have been tuned by hand to reproduce a range of reionisation histories. Four of the models are designed to have similar temperatures at $z \simeq 5$ that match the Becker *et al.* (2011) IGM temperature measurements, but with $z_{\rm re} = [15,\ 12,\ 9,\ 7]$. The final model, Tz9HOT, is similar to Tz9 but with increased photo-heating rates. The evolution of the temperature and the cumulative energy per proton deposited in a gas parcel at the mean background density (see Eq. (4.4) and Section 4.3 for details) in these models is displayed in Figure 4.1.

In order to extract mock spectra from our simulations we analyse snapshots at $z = 4.915$. The spectra consist of 2048 pixels drawn along 1000 random sight-lines parallel to the box boundaries. The mean transmission, $\langle F \rangle$, of the spectra is rescaled to correspond to an effective optical depth $\tau_{\rm eff} = -\ln\langle F \rangle = 1.53$ (Fan *et al.*, 2006a; Becker *et al.*, 2013), and the spectra are convolved with a Gaussian instrumental profile with $\mathrm{FWHM} = 7\,\mathrm{km\,s^{-1}}$. In order to aid intuition, Figure 4.2 demonstrates the range of gas densities the Lyα forest is sensitive to at $z = 4.9$. We plot the optical depth weighted gas overdensity, Δ_τ (Schaye *et al.*, 1999), against the transmitted flux from the D15 model. The Lyα forest at high redshift predominately probes gas close to the mean background density, with very little contribution from regions with overdensities greater than a few except where the transmission is saturated ($F = 0$). This may be

contrasted to the Lyα forest at $z = 2$–3, where the bulk of the transmission arises from mildly overdense gas (cf. fig. 4 in Bolton *et al.*, 2014).

Finally, before proceeding further we note that one caveat to our analysis is that reionisation is an inhomogeneous process and spatial fluctuations in the IGM temperature and pressure smoothing scale are expected during reionisation (Raskutti *et al.*, 2012; Lidz & Malloy, 2014; D' Aloisio, McQuinn & Trac, 2015). Our $10h^{-1}\,\mathrm{cMpc}$ simulation boxes are too small to capture this effect – this scale is comparable to the typical size of individual H II regions during reionisation (e.g. Wyithe & Loeb, 2004; Furlanetto, McQuinn & Hernquist, 2006) – but for this reason approximating a uniform redshift of reionisation over this volume is likely reasonable. The large scales on which temperature fluctuations occur also translate to a modest effect (< 5 per cent) on the one dimensional power spectrum (Lai *et al.*, 2006; McQuinn *et al.*, 2011; Greig, Bolton & Wyithe, 2015). A direct comparison of the gas clumping factor predicted by radiation hydrodynamical simulations performed in similar volumes to this work (Finlator *et al.*, 2012) to optically thin models (Pawlik, Schaye & van Scherpenzeel, 2009) also yields good agreement (see fig. 5 in Finlator *et al.*, 2012). Nevertheless, full radiation hydrodynamical simulations that model patchy reionisation may eventually be required. The first steps toward such large scale simulations are being made (Gnedin, 2014; Norman *et al.*, 2015; Pawlik, Schaye & Vecchia, 2015; Park *et al.*, 2016), although attaining the required mass resolution for modelling the high redshift Lyα forest in large volumes remains challenging.

4.2.2 The broadening of Lyα forest absorbers

In this section we briefly review the impact of thermal broadening and pressure smoothing on the Lyα forest power spectrum at $z \simeq 5$ (see also Bi, Boerner & Chu, 1992; Peeples *et al.*, 2010; Kulkarni *et al.*, 2015; Garzilli, Theuns & Schaye, 2015; Puchwein *et al.*, 2015). We begin with the assumption that Lyα absorbers are in hydrostatic equilibrium (Schaye, 2001). The scale where the dynamical time equals the sound crossing timescale is the Jeans scale, L_{J}, which may also be written in terms of a line of sight velocity, $\sigma_{\mathrm{J}} = H(z)L_{\mathrm{J}}$, where L_{J} is a proper distance. For gas with temperature T and normalised density Δ, this corresponds to:

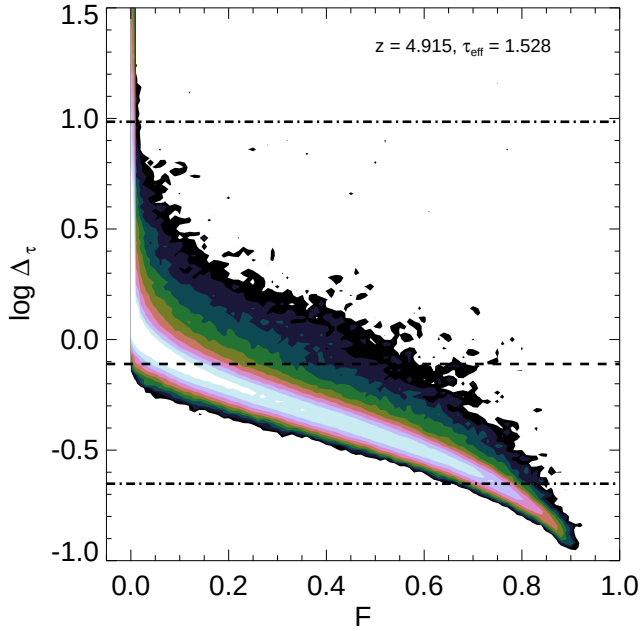


Figure 4.2: Contour plot of the optical depth weighted gas overdensity, Δ_τ, against transmitted flux F at $z = 4.9$ for the D15 model for $\tau_{\rm eff} = 1.53$. Here Δ_τ is calculated as a weighted average $\Delta_{\tau,{\rm j}} = \sum_{\rm i} \tau_{\rm i,j}\Delta_{\rm i} / \sum_{\rm i} \tau_{\rm i,j}$ and $\tau_{\rm i,j}$ is optical depth at the $i^{\rm th}$ pixel in real space contributing to the $j^{\rm th}$ pixel in velocity space (Schaye *et al.*, 1999). The number density of pixels increase by 0.5 dex within each contour level. The dashed and dot-dashed lines display the median and 95 per cent range of the optical depth weighted densities.

$$\begin{aligned}\sigma_{\rm J} &= \left(\frac{40\pi^2 k_{\rm B}}{9\mu m_{\rm H}}\right)^{1/2} T^{1/2}\Delta^{-1/2}\left(\frac{\Omega_{\rm m}(1+z)^3+\Omega_\Lambda}{\Omega_{\rm m}(1+z)^3}\right)^{1/2} \\ &\approx 77.1{\rm km\,s^{-1}}\left(\frac{\rm T_0}{10^4{\rm K}}\right)^{1/2}\Delta^{\gamma/2-1},\end{aligned} \tag{4.1}$$

where we assume $\mu = 0.61$ for the mean molecular weight of an admixture of ionised hydrogen and singly ionised helium[2]. In the second line we have also used the fact that $T = T_0\Delta^{\gamma-1}$ and $\Omega_{\rm m}(1+z)^3 \gg \Omega_\Lambda$ at $z \gtrsim 3$. Note, however, the Jeans scale only approximates the pressure smoothing scale in the low density IGM. As the dynamical timescale, $t_{\rm dyn} = \sqrt{\pi/G\rho_{\rm m}} \simeq H(z)^{-1}\Delta^{-1/2}$, is long for low density gas the absorbing structures in the Lyα forest at $z \simeq 5$ will not have reached hydrostatic equilibrium. The pressure smoothing scale is instead better described as $\sigma_{\rm p} = f_{\rm J}\sigma_{\rm J}$, where $f_{\rm J} < 1$ and

[2]The Jeans scale in Eq. (4.1) is larger than the classical cosmological Jeans scale, $\lambda_{\rm J}$ – derived from linear theory when assuming an adiabatic thermal history – by a factor of 2π (Bi, Boerner & Chu, 1992; Kulkarni *et al.*, 2015). For arbitrary thermal histories within the linear theory derivation, Gnedin & Hui (1998) further show that the pressure smoothing may be described by a filtering scale, $\lambda_{\rm F}$, which depends on the prior thermal history. Typically $\lambda_{\rm F} < \lambda_{\rm J}$ and $\lambda_{\rm F} \sim 100\,{\rm ckpc}$ ($\sim 10\,{\rm km\,s^{-1}}$ at $z = 5$), although the precise value is dependent on the prior heating history of the IGM.

depends on the prior thermal history (Gnedin & Hui, 1998; Hui & Rutledge, 1999, and see footnote 2).

In comparison, the thermal (or Doppler) broadening scale for a Gaussian line profile is given by:

$$\sigma_{\rm th} = \left(\frac{k_{\rm B}T}{m_{\rm H}}\right)^{1/2} = 9.1{\rm km\,s^{-1}} \left(\frac{\rm T_0}{10^4\,\rm K}\right)^{1/2} \Delta^{(\gamma-1)/2}. \quad (4.2)$$

The ratio of these two scales is $\sigma_{\rm p}/\sigma_{\rm th} \simeq 8.5 f_{\rm J} \Delta^{-1/2}$. In general we therefore expect the pressure smoothing to act on similar scales to the thermal broadening. Fortunately, as we see shall see next, the different scale dependence of these effects in our hydrodynamical simulations at $z = 5$ enables us to break this degeneracy.

4.2.3 The line of sight Lyα forest power spectrum

We compute the power spectrum of the transmitted flux, $P_{\rm F}(k)$, at $z = 4.9$ from our simulations using the estimator $\delta_{\rm F} = F/ < F > -1$, where $\langle F \rangle = \langle e^{-\tau} \rangle$ is the mean transmission (or equivalently the effective optical depth, $\tau_{\rm eff} = -\ln\langle F \rangle = 1.53$) of the 1000 sight-lines drawn from each simulation. The top row of Figure 4.3 shows the results for a sub-set of the models listed in Table 4.1. The left hand panel displays the effect of changing T_0 on the power spectrum; higher temperatures result in decreased power at wavenumbers $\log(k/{\rm km^{-1}\,s}) > -1.5$ arising from a combination of thermal broadening and pressure smoothing. The middle panel demonstrates the effect of changing γ – the slope of the temperature-density relation – is more modest, with a slight increase in power over all scales as γ is decreased. This is in part due to the fact that the typical gas densities probed by the Lyα forest at $z \simeq 5$ are close to mean density, and the characteristic pressure and thermal broadening scales both have a modest dependence on gas density. It also suggests that any constraint on γ from $P_{\rm F}(k)$ is likely to be weak at this redshift.

The right panel in the top row displays the four models with varying $z_{\rm re}$; recall these have similar T_0 at $z = 4.9$ but different reionisation redshifts. Any differences in $P_{\rm F}(k)$ are due variations in the pressure smoothing scale only. The Tz15 model has less power (and more pressure smoothing) than the Tz7 and Tz9 models over a wide

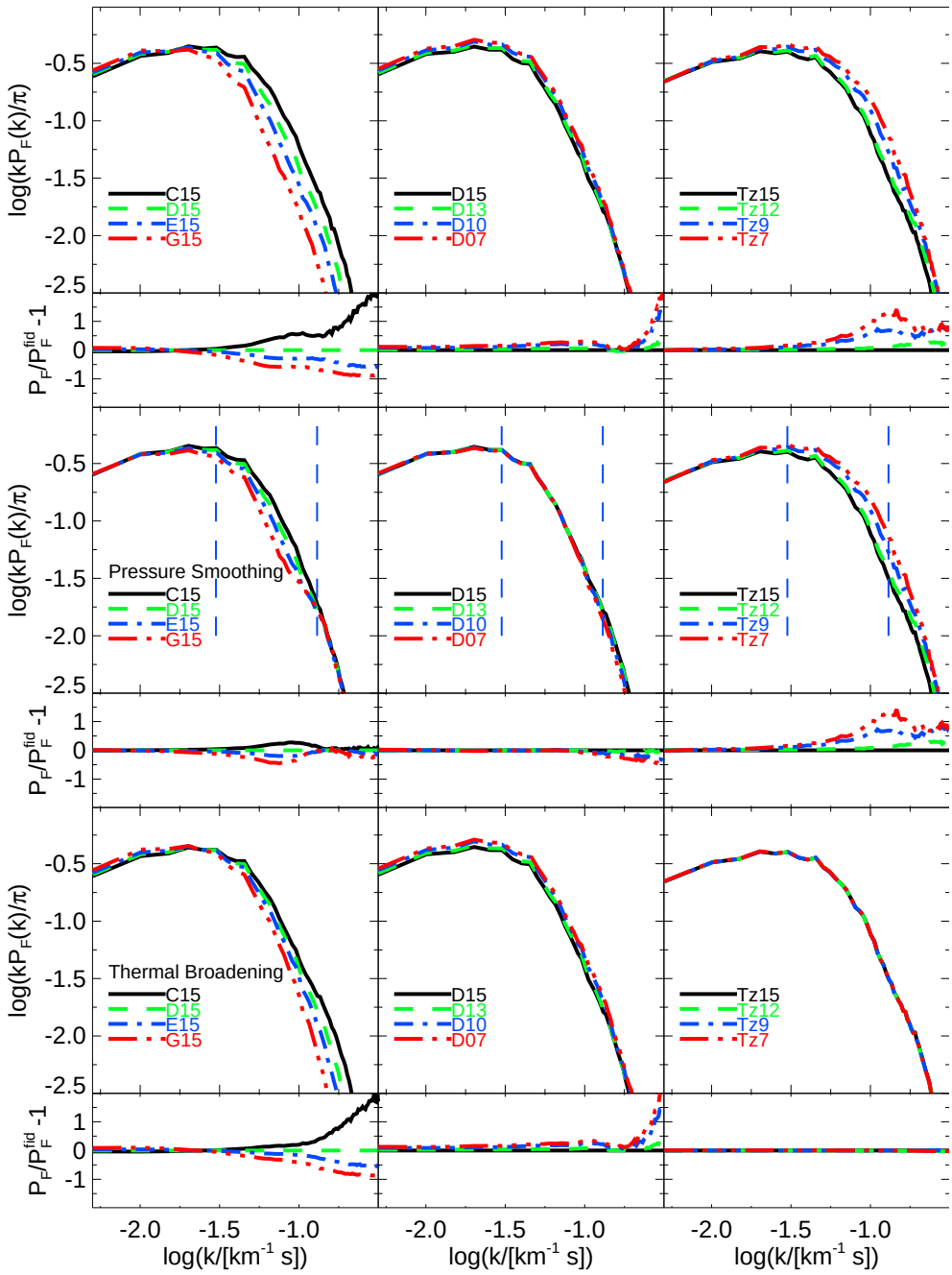


Figure 4.3: *Top row:* the transmitted flux power spectrum – including variations from both pressure smoothing and thermal broadening – at $z = 4.9$ for a sub-set of models with varying T_0 (left), γ (middle) and the redshift of reionisation (right). The power spectra are displayed relative to the D15 (left and middle) and Tz15 (right) models are displayed immediately below. *Middle row:* the power spectrum for the same simulations, but now with each $T - \Delta$ relation mapped to the D15 (left and middle) and the Tz15 model (right). The thermal broadening in these models is therefore identical. The dashed blue lines display the approximate wavenumber range over which pressure smoothing is dominant. Note that for simulations with varying γ (D15-D07, middle column), pressure smoothing has very little effect on the power spectrum except at the smallest scales. *Bottom row:* the transmitted flux power spectrum for the D15 (left and middle) and Tz15 (right) models after imposing the $T - \Delta$ relation from the models indicated in the figure legend. The pressure smoothing in these models is identical. The varying $z_{\rm re}$ models have almost identical values of T_0 at $z \sim 4.9$ (Figure 4.1) and therefore are indistinguishable when pressure smoothing is removed. This can be seen by comparing middle-right and bottom-right panels. The u_0 , T_0 and γ values for each model are listed in Table 4.1. All mock spectra are scaled to have $\tau_{\rm eff} = 1.53$, and have been convolved with a Gaussian with FWHM=7 $\rm km\,s^{-1}$.

range of wavenumbers, with the largest differences at $\log(k/\mathrm{km}^{-1}\,\mathrm{s}) \simeq -1$. Earlier reionisation allows more time for the gas to respond to the change in pressure due to heating during and soon after reionisation, resulting in increased smoothing of the gas distribution. Note also the power spectra for the Tz15 and Tz12 models are very similar, although the cumulative energy per proton deposited at mean density, u_0, by $z = 4.9$ in these models is rather different. A related result was noted by Pawlik, Schaye & van Scherpenzeel (2009), who found that the clumping factor[3], $C = \langle\rho^2\rangle/\bar{\rho}^2$, of gas in optically thin hydrodynamical simulations at $z \approx 6$ is insensitive to the redshift of reionisation if $z_{\mathrm{re}} \geq 9$. Although the exact upper redshift limit will be model dependent, this indicates the pressure smoothing is only sensitive to the prior IGM thermal history over a limited redshift range (see also Figure 4.8 and text in Section 4.5).

We may examine the impact of pressure smoothing and thermal broadening on the Lyα forest power spectrum more easily by separating these effects in our models. We first fit a single power law to the $T - \Delta$ relation in each model, with $\log T_0$ and $\gamma - 1$ as the intercept and slope. We then translate and rotate the entire $T - \Delta$ plane in each simulation to match $\log T_0$ and $\gamma - 1$ from another model. This procedure allows us to change the instantaneous temperature of the gas, but retain the same pressure smoothing scale (which arises from the underlying gas density distribution). The middle row in Figure 4.3 displays the result of this procedure, where we have transformed each $T - \Delta$ plane in each model to correspond to the T_0 and γ values in the D15 simulation in the left and middle column, and the Tz15 model in the right. Note that as the temperatures are changed we also rescale the neutral hydrogen number densities in the simulated spectra as $n_{\mathrm{HI}} \propto T^{-0.72}$, due to the temperature dependence of the H II recombination coefficient (Verner & Ferland, 1996). All models are again rescaled to have the same $\tau_{\mathrm{eff}} = 1.53$.

As might be expected, the different thermal histories in the simulations displayed in the middle left panel of Figure 4.3 produce rather different pressure smoothing scales. With the effect of thermal broadening removed, this effect is most prominent at wavenumbers $0.03 \leq k/[\mathrm{km}^{-1}\,\mathrm{s}] \leq 0.13$, shown by the dashed vertical lines, although

[3]The clumping factor is related to the root mean square of the density contrast (and hence also the gas density power spectrum) by $\langle\delta^2\rangle = C - 1$, where the density contrast is $\delta = \rho/\bar{\rho} - 1$.

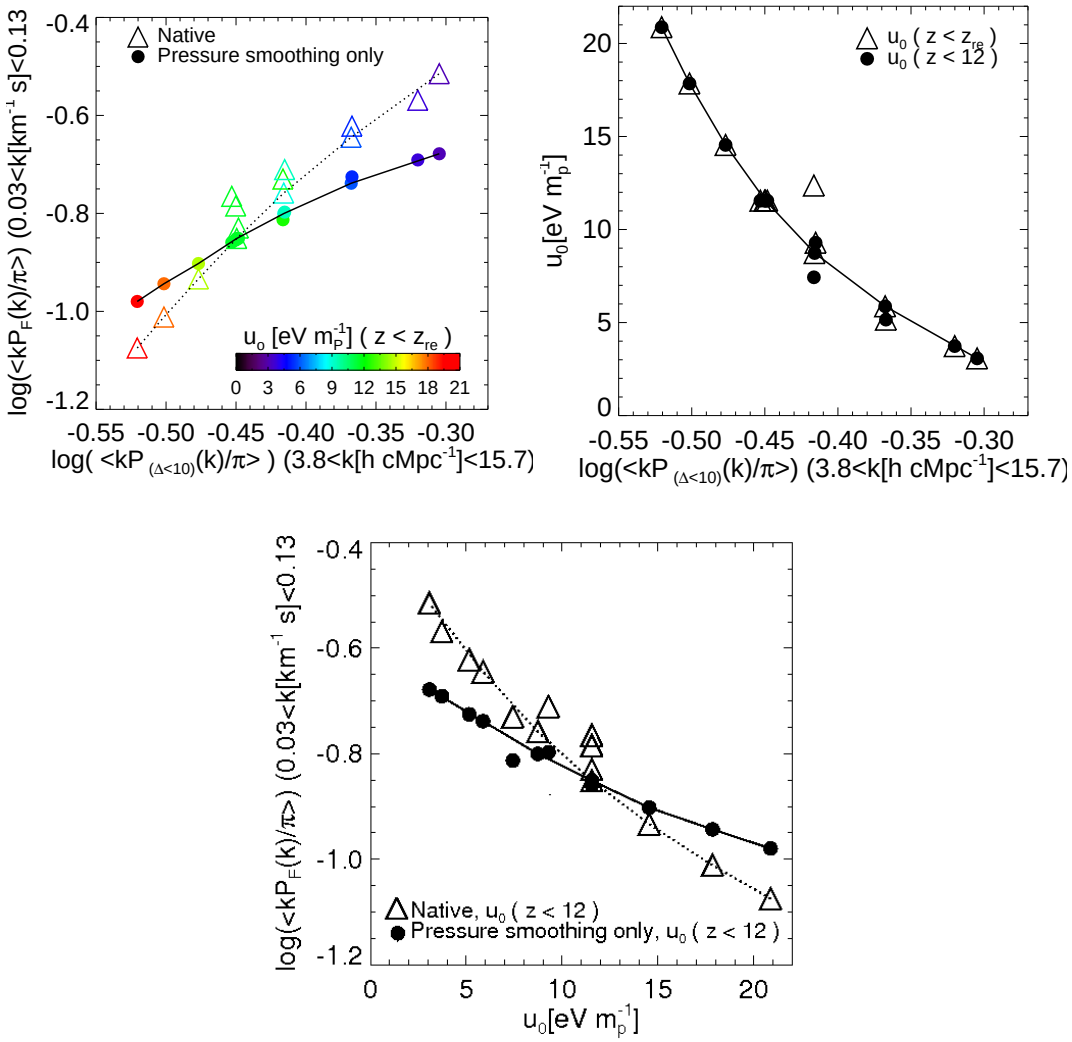


Figure 4.4: *Top left:* The open triangles display the average of the Lyα forest power spectrum at wavenumbers $0.03 < \mathrm{k/km^{-1}\,s} < 0.13$ (approximately the scale where pressure smoothing dominates) against the $\Delta < 10$ gas density power spectrum averaged over the equivalent scale. The A15–G15, Tz15–Tz7 and D13–D07 models are shown at $z = 4.9$, with a dotted curve through the A15–G15 models. The average Lyα forest power spectrum for each model after thermal broadening differences are removed is shown by the filled circles. Here each $T - \Delta$ distribution is mapped to the T_0 and γ for the D15 model, and a solid curve is drawn through the A15–G15 models. The colour scale indicates u_0 for each model. *Top right:* The cumulative energy per proton against the average of the $\Delta < 10$ density power spectrum computed using Eq. (4.4) for all photo-heating up to $z_{\rm re}$ for each model (open triangles) and $z = 12$ (filled circles). The solid curve is again drawn through the A15–G15 models. *Bottom:* The average of the Lyα forest flux power spectrum at wavenumbers $0.03 < \mathrm{k/km^{-1}\,s} < 0.13$ (open triangles) against $u_0(z < 12)$. The filled circles show the same quantity once differences due to thermal broadening are removed. The solid and dashed curves are again drawn through A15–G15 models.

it operates to a lesser extent at smaller scales (i.e. larger wavenumbers) as well. In contrast, the central panel demonstrates the slope of the $T - \Delta$ relation has very little impact on the pressure smoothing except at the smallest scales – note the cumulative energy per proton deposited into a gas parcel at mean density is identical in these simulations. The models with varying $z_{\rm re}$ are also largely unchanged, emphasizing again that it is the pressure smoothing which causes the differences in the power spectrum for these models.

Finally, the bottom row of Figure 4.3 displays the flux power spectrum computed using the density field from the D15 model (left and middle panel) and the Tz15 model (right panel), but with an imposed $T - \Delta$ relation that matches the models indicated in the figure panels. This procedure isolates the impact of thermal broadening on $P_{\rm F}(k)$. There is some degeneracy with the pressure smoothing, but in general the thermal broadening acts on smaller scales, with the largest difference in the models occurring at $\log(k/{\rm km^{-1}\,s}) > -1$. The small-scale cut-off for the power spectrum is mainly determined by the instantaneous temperature (Peeples *et al.*, 2010). This also suggests that measurements of the power spectrum at small scales, $-1 \leq \log(k/{\rm km^{-1}\,s}) \leq -0.5$, are required to break the degeneracy between pressure smoothing and thermal broadening. Note also the models in the middle panel are similar to the results in the top row; most of the contribution to the power when changing γ is from thermal broadening. As expected, there is no apparent difference in power among the varying $z_{\rm re}$ models, which are designed to reach a similar temperature at mean density around $z \simeq 5$.

4.3 From flux power spectrum to thermal history

We now proceed to examine the relationship between the transmitted flux power spectrum at $z \simeq 5$ and the integrated thermal history in our hydrodynamical simulations. The temperature evolution of a gas parcel with density ρ in an expanding universe can be expressed as (e.g. Miralda-Escudé & Rees, 1994; McQuinn & Upton Sanderbeck, 2016)

$$\frac{dT}{dt} = \frac{2\mu m_H}{3k_B\rho}(\mathscr{H} - \Lambda) + \frac{2T}{3(1+\delta)}\frac{d\delta}{dt} + \frac{T}{\mu}\frac{d\mu}{dt} - 2HT, \tag{4.3}$$

where $\mathscr{H} = \sum_{\rm i} n_i \epsilon_i$ is the total photoheating rate per unit volume for the species $i = [\mathrm{H\,I}, \mathrm{He\,I}, \mathrm{He\,II}]$, Λ is the cooling rate per unit volume, and H is the Hubble parameter. The first term in Eq. (4.3) encapsulates all the photo-heating and radiative cooling processes. The second term describes adiabatic heating and cooling from structure formation, and the third term is associated with changes in the mean molecular weight. The final term arises from adiabatic cooling due to the expansion of the Universe.

The cumulative energy deposited into a gas parcel by photo-heating is obtained by considering the first term in Eq. (4.3) and setting the radiative cooling term to zero. Noting that the specific internal energy is given by $u = 3k_BT/2\mu m_{\rm H}$, we may then write $du/dt = \mathscr{H}/\rho$. For a gas parcel at the mean background density, the total energy per unit mass deposited into the gas parcel by redshift z_0 is

$$u_0 = \int_{z_{\rm o}}^{z_{\rm re}} \frac{\mathscr{H}}{\bar{\rho}} \frac{dz}{H(z)(1+z)}, \tag{4.4}$$

where $\bar{\rho} = \rho_{\rm crit}\Omega_{\rm b}(1+z)^3$ is the mean background baryon density. This quantity is displayed in the left panel of Figure 4.1 and is listed in Table 4.1 at $z = 4.9$. The cumulative energy per proton deposited into a gas parcel at mean density is straightforward to compute for a given reionisation history in our Lyα forest simulations.

We illustrate the relationship between the transmitted flux power spectrum, the gas density power spectrum and u_0 in our hydrodynamical simulations in Figure 4.4. The open triangles in the left panel display the mean of the transmitted flux power spectrum against the mean of the gas density power spectrum for all gas with $\Delta < 10$. The mean is obtained over the scales $0.03 \leq k/[\mathrm{km^{-1}\,s}] \leq 0.13$, approximately corresponding to the scales over which the influence of pressure smoothing is largest in our models (see Figure 4.3). Following Kulkarni *et al.* (2015) and Lukić *et al.* (2015), we consider the gas density power spectrum for normalised densities $\Delta < 10$ only; including higher density gas associated with non-linear structure results in significantly more power toward small scales. As shown in Figure 4.2, the Lyα forest power spectrum at $z \simeq 5$

is insensitive to absorption from gas at these densities. The precise choice of cut-off here is somewhat arbitrary, but is motivated by the fact that optical depth weighted densities, $0.2 \leq \Delta_\tau \leq 10$, bound 95 per cent of all Lyα forest pixels at $z = 4.9$ in our models.

There is a correlation between the Lyα forest power spectrum and the underlying gas density power spectrum, as expected. Models with a greater energy deposited per proton exhibit less power on scales $0.03 \leq k/(\mathrm{km^{-1}\,s}) \leq 0.13$ due to the smoother distribution of gas. The points that scatter upward from the dotted curve correspond to the varying γ and $z_{\rm re}$ models. The increased power in the transmitted flux arises from differences in the thermal broadening, even for models where the average gas density power spectrum (and energy input per proton) are similar. The pressure smoothing is thus still somewhat degenerate with thermal broadening on these scales. This is evident from the filled circles in the top-left panel of Figure 4.4, which display the average Lyα forest power spectrum after rescaling the T–Δ relation in all models to match the D15 simulation. This implies if the degeneracy between thermal broadening and pressure smoothing is broken with the transmitted flux power spectrum on scales $\log(k/\mathrm{km^{-1}\,s}) > -1$, the Ly$\alpha$ forest directly probes the underlying gas density power spectrum (or equivalently the gas clumping factor[4]) at $z \simeq 5$.

The open triangles in the top-right panel of Figure 4.4 display the cumulative energy deposited per proton at mean density, u_0, computed using Eq. (4.4) against the gas density power spectrum for $\Delta < 10$. The gas density power spectrum is averaged over the same scale as in the left panel. Again, there is an excellent correlation between the two quantities aside from the triangle at $u_0 = 12.4\,\mathrm{eV\,m_p^{-1}}$ corresponding to the Tz15 model with $z_{\rm re} = 15$. All the other models experience rapid reionisation at $z \leq 12$. As discussed earlier, this is because the thermal history at $z > 12$ does not significantly impact on the pressure smoothing scale of the gas in our simulations. This is illustrated by the filled circles in the right panel, which show u_0 computed at $z \leq 12$ only.

Finally, the open triangles in the bottom panel of Figure 4.4 display the correlation

[4]We have verified that the gas clumping factor, $C = \langle\rho^2\rangle/\bar{\rho}^2$, for gas with $\Delta < 10$ in the simulations is also tightly correlated with the gas density power spectrum averaged over the scales used in Figure 4.4. The clumping factor is $C \simeq 2$–3 in our models at $z = 4.9$.

between the average flux power spectrum on scales $0.03 \leq k/(\mathrm{km}^{-1}\,\mathrm{s}) \leq 0.13$ and u_0 at $z < 12$. Note again there is some degeneracy with thermal broadening when averaging on these scales; the filled circles show the same quantity once differences due to thermal broadening are removed. This simple analysis suggests that $u_0(z \lesssim 12)$ should serve as a convenient and useful parameterisation for the prior thermal history in our simulations. A more rigorous approach requires analysing the full Lyα forest power spectrum and correctly dealing with the parameter degeneracies in the model, which we turn to next.

4.4 Inferring the thermal history during reionisation

4.4.1 Markov Chain Monte Carlo analysis

We make forecasts for the constraints attainable on the thermal history using a Bayesian MCMC approach. Given a set of power spectrum measurements, $P_{\mathrm{F}}^{\mathrm{data}}$, we maximise the likelihood function, $\mathcal{L}$, with respect to the model parameters used in our hydrodynamical simulations, M, (e.g. Zaroubi *et al.*, 2006; Viel, Bolton & Haehnelt, 2009; Rorai, Hennawi & White, 2013)

$$\ln \mathcal{L}(P_{\mathrm{F}}^{\mathrm{data}}|M) \propto (P_{\mathrm{F}}^{\mathrm{data}} - P_{\mathrm{F}}^{\mathrm{model}})^T \Sigma_{\mathrm{data}}^{-1} (P_{\mathrm{F}}^{\mathrm{data}} - P_{\mathrm{F}}^{\mathrm{model}}). \tag{4.5}$$

Here $P_{\mathrm{F}}^{\mathrm{model}}$ is the simulated Lyα forest power spectrum for a given set of model parameters M, while Σ_{data} is the covariance matrix for the measured power spectrum.

We consider four parameters in our analysis – $\log T_0$, u_0 , γ and τ_{eff} – and vary these to construct grid of models based on our A15–G15 simulations. We obtain combinations of the three thermal parameters by imposing different T–Δ relations on the simulations, as described in Section 4.2.3. In this way we retain the gas density power spectrum associated with a given value of u_0 in our models while varying the instantaneous temperature. We consider seven values for for the cumulative energy deposited per proton over the range $u_0 = 3.1$–$20.9\,\mathrm{eV\,m_p^{-1}}$, following the parameter range covered by our hydrodynamical simulations[5]. The T–Δ relation is varied over

[5]For reference, the UVB synthesis models from Faucher-Giguère *et al.* (2009), Haardt & Madau

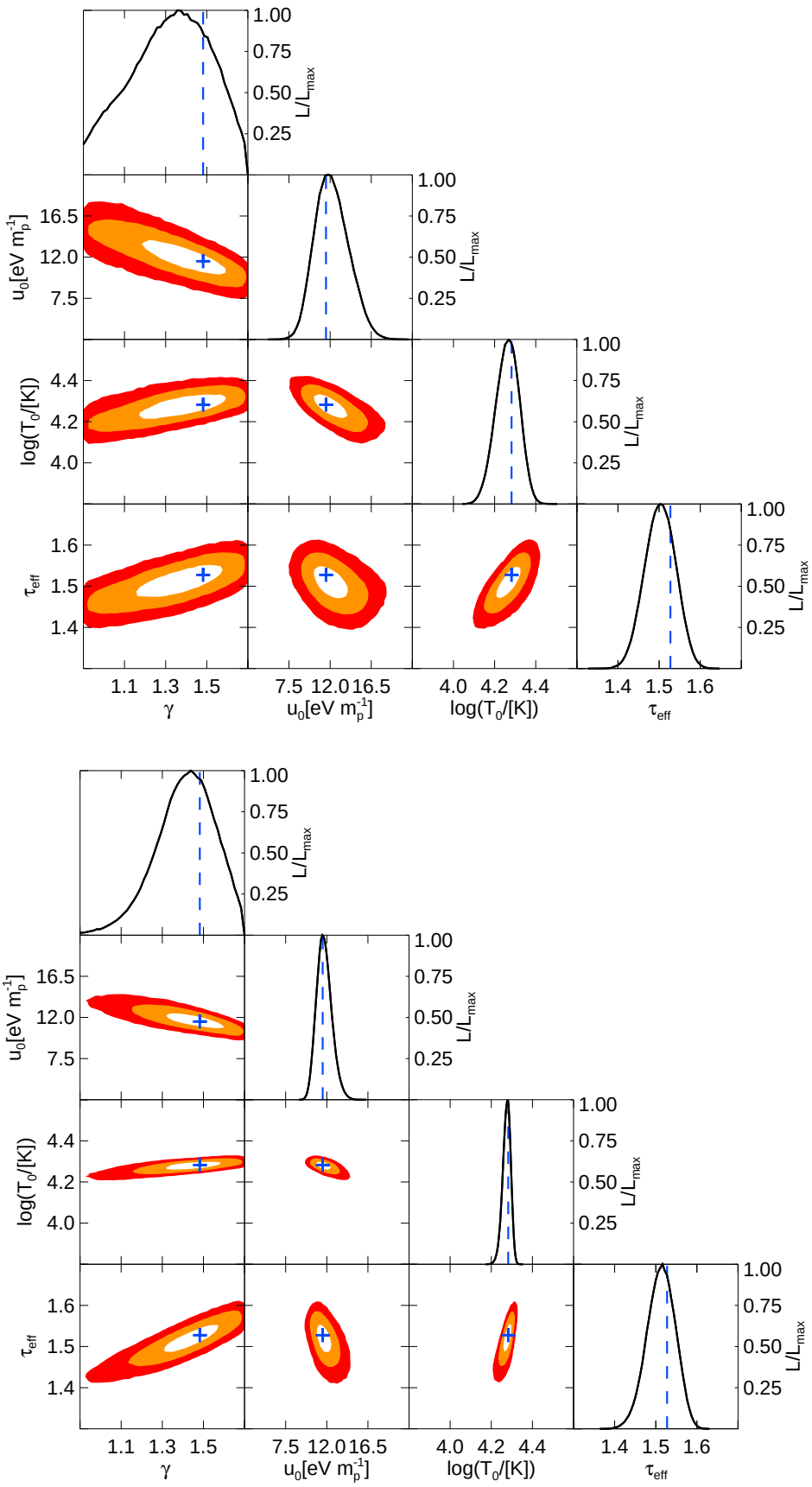


Figure 4.5: *Top:* The contours display the two dimensional probability distributions for the parameters $\log T_0$, u_0, γ and $\tau_{\rm eff}$ recovered from mock observations of the D15 Lyα forest power spectrum using the realistic data scenario. The joint 1σ, 2σ and 3σ contours are shown in white, orange and red, respectively. The black curves display the one dimensional marginalised posterior distributions for each parameter. The blue cross and blue vertical dashed line show the true model values (see Table 4.2). *Bottom:* As for the top panel, except now for the optimistic data scenario (see text for further details).

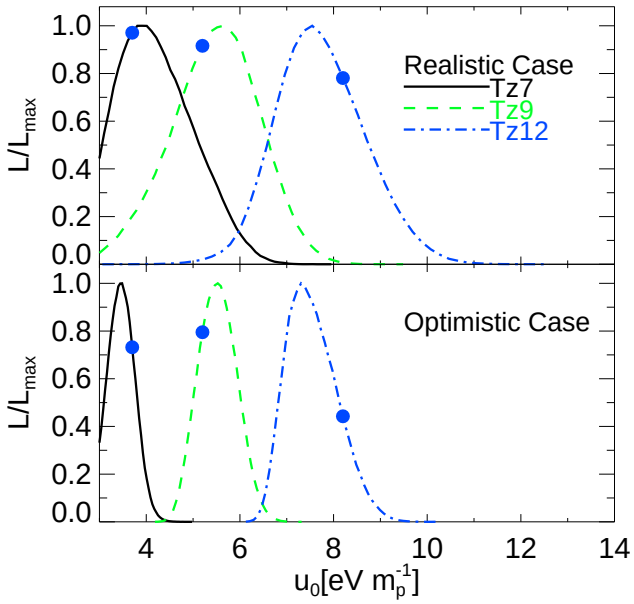


Figure 4.6: The one dimensional marginalised posterior distributions for u_0 obtained from mock observations of the Tz12 (solid black curve), Tz9 (dashed green curve) and Tz7 (dot-dashed blue curve) simulations. The upper (lower) panels display the realistic (optimistic) data scenario. The true u_0 values at $z < 11.5$ in the simulations are shown by the blue points. These models have very similar values for $\log(\mathrm{T}_0)$ and γ at $z \simeq 5$ (see Table 4.1).

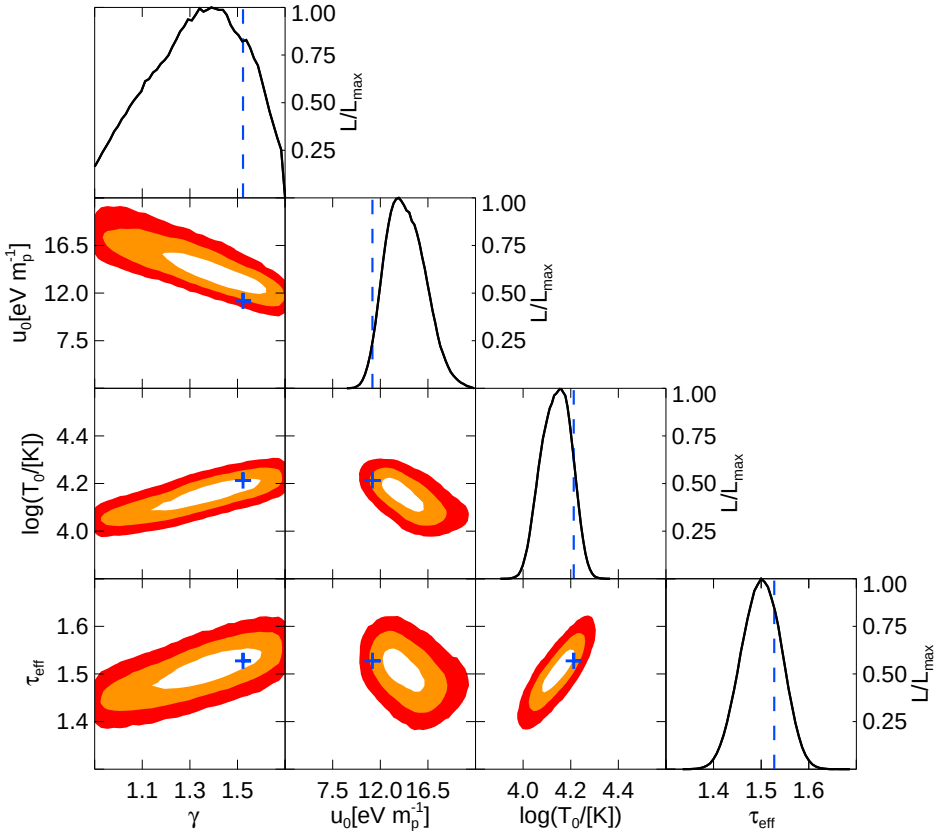


Figure 4.7: As for Figure 4.5, but now for the Tz9HOT model using the realistic data scenario.

$\log(T_0/\mathrm{K}) = 3.6$–$5.0$ and $\gamma = 0.6$–1.8. The former range is consistent with estimates of the IGM temperature at mean density at $z \simeq 5$, while the latter encompasses physically plausible values of γ (Becker *et al.*, 2011; McQuinn & Upton Sanderbeck, 2016). We apply flat priors for all the free parameters except for $\tau_{\rm eff}$, where we instead use a Gaussian prior with mean $\tau_{\rm eff} = 1.53$ and a 1σ uncertainty corresponding to 4 per cent of the mean, based on the observational measurement from Becker *et al.* (2011). The range of $\tau_{\rm eff}$ values on our grid of simulations are $0.7 - 1.3$ times the mean effective optical depth. If we use a flat rather than Gaussian prior, we find the recovery of the thermal parameters is degraded by the freedom to increase (decrease) the amplitude of the power spectrum on all scales as $\tau_{\rm eff}$ is increased (decreased). In total, we have $9 \times 13 \times 7 \times 7 = 5733$ grid points in our model parameter space. The mock spectra for each parameter combination on this grid of models are post-processed by convolving with a Gaussian instrumental profile of $\mathrm{FWHM} = 7\,\mathrm{km\,s^{-1}}$ and rebinning to $3\,\mathrm{km\,s^{-1}}$ per pixel. Gaussian distributed noise is added and $\tau_{\rm eff}$ is rescaled iteratively to match the required value. Once the model Lyα forest power spectrum parameters are selected, $P_{\rm F}^{\rm model}$ is obtained by performing a multi-linear interpolation on the grid of models.

We match the binning of the Lyα forest power spectrum to mock observations, $P_{\rm F}^{\rm data}$, that we extract from one of our simulations. These consist of 20 data points equally spaced in $\log(k/\mathrm{km^{-1}\,s})$. We consider two simple data scenarios, which we describe as "realistic" and "optimistic". The former is comparable to existing Lyα forest data sets at $z \simeq 5$ (Becker *et al.*, 2015), while the latter may be more appropriate for observations with high resolution spectrographs on 30 metre class telescopes in the forthcoming decade (e.g. Maiolino *et al.*, 2013). In the realistic case, we consider a total redshift path length of $\Delta z = 4$, a signal-to-noise ratio $\mathrm{S/N} = 15$ per pixel and bin the power spectrum over the range $-2.3 < \log(\mathrm{k/km^{-1}\,s}) < -0.7$. For the optimistic case, we instead adopt a redshift path length five times larger, $\Delta z = 20$, and a higher signal-to-noise per pixel, $\mathrm{S/N} = 50$. The significantly higher signal-to-noise allows the power spectrum to be measured to smaller scales, up to a maximum wavenumber of $\log(\mathrm{k/km^{-1}\,s}) = -0.5$. As demonstrated earlier in Figure 4.3, small scale information assists in breaking the degeneracy between thermal broadening and

(2001) and Haardt & Madau (2012) correspond to reionisation at $z_{\rm re}^{\rm FG09} = 10$, $z_{\rm re}^{\rm HM01} = 9$ and $z_{\rm re}^{\rm HM12} = 15$ with $u_0^{\rm FG09} = 7.5\,\mathrm{eV\,m_p^{-1}}$, $u_0^{\rm HM01} = 6.7\,\mathrm{eV\,m_p^{-1}}$ and $u_0^{\rm HM12} = 11.0\,\mathrm{eV\,m_p^{-1}}$ by $z = 4.9$.

pressure smoothing.

We compute the mean and the distribution for each mock data point by performing 5000 bootstrap samples with replacement. The covariance matrix, $\Sigma_{\rm data}$, is also determined from these distributions. As this matrix can be noisy for real data, following Lidz *et al.* (2006) and Viel *et al.* (2013a) we regularise the covariance matrix using the correlation coefficients obtained from all 1000 sight-lines drawn from each simulation. Finally, we increase the 1σ bootstrapped uncertainties by 30 per cent to account for a possible underestimate in the sample variance (Rollinde *et al.*, 2013) and invert the matrix using singular value decomposition. For each mock observation, $P_{\rm F}^{\rm data}$, we perform 10^6 Markov chain iterations and discard the first half of the chain as the burn-in. We verify all chains are converged by visual inspection.

4.4.2 Distinguishing between reionisation models with $P_{\rm F}({\rm k})$

Table 4.2 summarises the results of our MCMC analysis for the realistic and optimistic scenarios for a selection of our models (for $\log T_0$ and u_0 only), and Figure. 4.5 displays the predicted parameter constraints for the D15 model.

In general we find the model parameters are recovered accurately, with only a few exceptions that we shall discuss below. As was (qualitatively) apparent from Figure 4.3, we find the power spectrum is rather insensitive to the slope of the T–Δ relation. The parameter γ is recovered within the 68 per cent credible interval but with fairly broad bounds for most of our models, even for the optimistic data set. Figure 4.5 indicates it will be difficult to obtain precise constraints on this parameter from the Lyα power spectrum alone at $z \simeq 5$, although probing gas at somewhat higher densities with a joint analysis of the Lyβ forest may improve this situation (Dijkstra, Lidz & Hui, 2004; Furlanetto & Oh, 2009; Iršič & Viel, 2014; Boera *et al.*, 2016). On the other hand, in the absence of significant systematics it should be possible to jointly constrain T_0 and u_0 using existing Lyα forest data at $z \simeq 5$ when including the power spectrum on scales, $\log(k/{\rm km}^{-1}\,{\rm s}) > -1$. Our MCMC analysis indicates that with current data, the cumulative energy deposited per proton at mean density may be constrained to a statistical precision of around ~ 20 per cent, corresponding to the 68 per cent credible interval. The optimistic data scenario instead yields ~ 8 per cent, again at the 68 per

cent credible interval. However, as we discuss in the next section, systematic uncertainties from observational and numerical effects will also be important to consider.

The analysis also demonstrates that such a measurement should already be able to distinguish between some reionisation scenarios. The one dimensional posterior distributions for u_0 obtained from the Tz12, Tz9 and Tz7 models are displayed in Figure 4.6. Recall that these models have T–Δ relations which are almost identical at $z = 4.9$, but rather different integrated thermal histories. We do not consider the Tz15 model – as already discussed the power spectrum for this model is very similar to the Tz12 simulation. On performing the full MCMC analysis, we recover the cumulative energy input per proton from $4.9 \leq z \leq 11.5$ in the simulations to within 1σ, and at a precision comparable to the results in Figure 4.5. Note again, however, that the redshift above which the pressure smoothing scale no longer retains a memory of the thermal history will be model dependent (cf. Pawlik, Schaye & van Scherpenzeel, 2009). In addition, we find in this case the peaks of the posterior distributions do not match exactly to the true value of the parameters in the simulations. This is because only the A15–G15 models were used to construct the parameter grid in the MCMC analysis.

As a further demonstration of the model dependent nature of these predicted constraints, we also construct mock observations from the Tz9HOT model where the IGM is heated to around $T \simeq 20\,000\,\mathrm{K}$ following reionisation. In Figure 4.7, it is clear the recovered $\log T_0$ and u_0 are only consistent within the 95 per cent credible interval for the realistic scenario. The smaller statistical error bars obtained in the optimistic case are now inconsistent with the 95 per cent credible interval for u_0. Clearly, an accurate recovery of the thermal history relies on the grid of models used within the MCMC procedure. This suggests that developing a set of numerical models which sample the u_0–$\log T_0$ parameter space as widely and frequently as is practical will therefore be vital for measuring these parameters using observational data (see Chapter 5).

4.4.3 Systematic uncertainties

Observational and numerical systematics will also impact on the recovery of u_0 from the transmitted flux power spectrum. These have already been quantified in detail by Viel *et al.* (2013a) (hereafter V13) in the context of constraining the mass of a putative

Table 4.2: Predicted constraints on $\log(\mathrm{T}_0)$ and u_0 obtained from mock observations for the realistic and optimistic data scenarios (see text for details). From left to right, the columns list the simulation used to construct the mock observation, the parameters used in the simulation and the predicted constraints. The values correspond to the median of the marginalised posterior distribution for each parameter, along with the 68 and 95 per cent credible intervals. The final two rows correspond to the constraints from the mock data after an additional 20 per cent systematic uncertainty in the transmitted flux power spectrum at all scales is added in quadrature to the bootstrap error bars (see text for details).

	Model values		"Realistic" scenario		"Optimistic" scenario	
	$\log(\mathrm{T}_0/\mathrm{K})$	$u_0 \mathrm{eV\,m_p^{-1}}$	$\log(\mathrm{T}_0/\mathrm{K})$	$u_0 \mathrm{eV\,m_p^{-1}}$	$\log(\mathrm{T}_0/\mathrm{K})$	$u_0 \mathrm{eV\,m_p^{-1}}$
Model		$4.9 \leq z \leq 11.5$	68% (95%) C.I.	68% (95%) C.I.	68% (95%) C.I.	68% (95%) C.I.
B15	3.98	5.9	$3.96^{+0.08}_{-0.07}$ $(^{+0.15}_{-0.14})$	$6.1^{+1.0}_{-1.1}$ $(^{+1.9}_{-2.2})$	$3.97^{+0.03}_{-0.03}$ $(^{+0.05}_{-0.05})$	$6.1^{+0.4}_{-0.5}$ $(^{+0.9}_{-1.0})$
D15	4.28	11.5	$4.27^{+0.06}_{-0.06}$ $(^{+0.10}_{-0.12})$	$12.3^{+2.0}_{-1.7}$ $(^{+4.0}_{-3.2})$	$4.28^{+0.02}_{-0.02}$ $(^{+0.03}_{-0.04})$	$11.8^{+0.9}_{-0.8}$ $(^{+1.9}_{-1.4})$
F15	4.47	17.8	$4.47^{+0.04}_{-0.04}$ $(^{+0.07}_{-0.08})$	$18.2^{+1.7}_{-2.2}$ $(^{+2.5}_{-4.0})$	$4.47^{+0.02}_{-0.02}$ $(^{+0.03}_{-0.04})$	$18.0^{+1.3}_{-1.3}$ $(^{+2.4}_{-2.4})$
Tz12	3.93	8.2	$3.95^{+0.06}_{-0.07}$ $(^{+0.11}_{-0.13})$	$7.8^{+1.0}_{-0.9}$ $(^{+2.1}_{-1.7})$	$3.97^{+0.03}_{-0.04}$ $(^{+0.04}_{-0.08})$	$7.5^{+0.6}_{-0.5}$ $(^{+1.2}_{-0.9})$
Tz9	3.92	5.2	$3.90^{+0.09}_{-0.08}$ $(^{+0.16}_{-0.15})$	$5.6^{+0.9}_{-1.0}$ $(^{+1.7}_{-2.0})$	$3.90^{+0.03}_{-0.03}$ $(^{+0.05}_{-0.06})$	$5.6^{+0.4}_{-0.4}$ $(^{+0.8}_{-0.8})$
Tz7	3.93	3.7	$3.89^{+0.07}_{-0.09}$ $(^{+0.12}_{-0.18})$	$4.2^{+0.9}_{-0.7}$ $(^{+1.8}_{-1.1})$	$3.96^{+0.02}_{-0.02}$ $(^{+0.04}_{-0.04})$	$3.5^{+0.3}_{-0.3}$ $(^{+0.6}_{-0.5})$
Tz9HOT	4.21	11.3	$4.15^{+0.06}_{-0.07}$ $(^{+0.11}_{-0.12})$	$14.2^{+2.0}_{-1.7}$ $(^{+4.0}_{-3.0})$	$4.15^{+0.03}_{-0.04}$ $(^{+0.06}_{-0.08})$	$14.1^{+1.0}_{-0.9}$ $(^{+2.1}_{-1.6})$
D15+sys.	4.28	11.5	$4.28^{+0.10}_{-0.09}$ $(^{+0.19}_{-0.17})$	$12.4^{+3.3}_{-3.1}$ $(^{+6.5}_{-6.4})$	$4.27^{+0.05}_{-0.05}$ $(^{+0.11}_{-0.10})$	$12.9^{+3.0}_{-2.5}$ $(^{+6.1}_{-4.7})$
Tz9+sys.	3.92	5.2	$3.90^{+0.13}_{-0.12}$ $(^{+0.22}_{-0.20})$	$5.8^{+1.5}_{-1.5}$ $(^{+3.1}_{-2.5})$	$3.92^{+0.06}_{-0.06}$ $(^{+0.13}_{-0.12})$	$5.5^{+1.3}_{-1.1}$ $(^{+2.7}_{-2.1})$

warm dark matter particle at $z \simeq 5$. However, we also briefly outline these here for completeness and estimate their contribution to the total uncertainty budget.

There are four main sources of systematic uncertainty to consider. Following V13, in approximately ascending order of importance, these are (i) metal line contamination; (ii) the numerical convergence of the simulations; (iii) spatial fluctuations in the ionisation state of the IGM and (iv) continuum placement on the observational data. Note the impact of galactic outflows on the Lyα forest is expected to minimal by $z \gtrsim 4$ (Viel, Schaye & Booth, 2013b).

Narrow metal absorption lines at $z \simeq 5$ arising from C IV, Si IV and Mg II at lower redshifts have only a minimal effect (< 1 per cent) on scales $\log(k/\mathrm{km}^{-1}\,\mathrm{s}) < -1$ (V13). However, the contribution of metals to the power spectrum may become more important toward smaller scales. We find data at $\log(k/\mathrm{km}^{-1}\,\mathrm{s}) > -1$ is important for breaking the degeneracy between thermal broadening and pressure smoothing, and metals may impact here at the ~ 5 per cent level. Corrections to the numerical convergence of the simulations with mass resolution and box size must be applied to the simulations from the results of convergence tests. V13 estimate an additional systematic uncertainty of ~ 5 per cent in addition to this known correction. Spatial fluctuations in the background ionisation rate, particularly if the mean free path for Lyman continuum photons is small and/or the ionising sources are rare (Davies & Furlanetto, 2015; Chardin *et al.*, 2015), may have a ~ 10 per cent impact on the power spectrum on the scales of interest here. V13 include this as an additional parameter, f_{UV}, which is marginalised over in their MCMC analysis. Finally, the placement of the continuum on high resolution quasar spectra is uncertain at around 10–20 per cent at $z \simeq 5$, which translates to a comparable uncertainty on the amplitude of the power spectrum. In practice, this uncertainty can be forward modelled in the mock spectra (see e.g. V13 and Faucher-Giguère *et al.*, 2008).

We estimate the total systematic uncertainty by adding these contributions in quadrature, yielding $\sim$ 15–25 per cent for the Lyα forest power spectrum on the scales of interest. We estimate the effect on the precision of the measurements by adding in quadrature an additional 20 per cent uncertainty on $P_F(k)$ to our bootstrapped error bars before performing the MCMC analysis. The resulting parameter constraints for

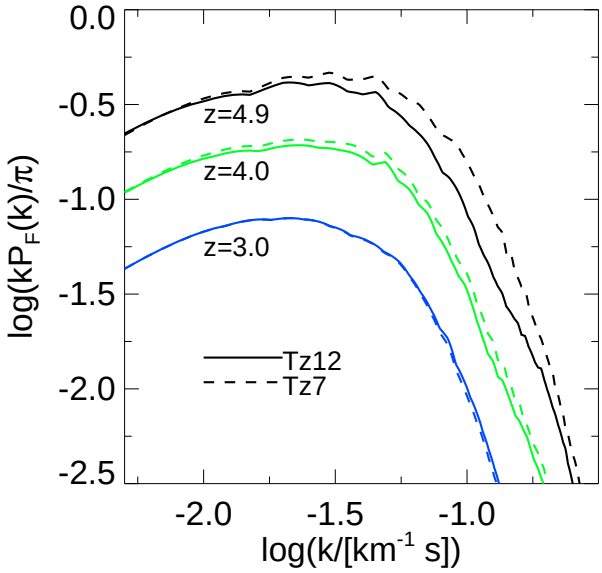


Figure 4.8: The Lyα forest transmitted flux power spectrum at $z = 4.9$ (black), $z = 4.0$ (green) and $z = 3.0$ (blue) for the Tz12 (solid) and Tz7 (dashed) models. All mock spectra are scaled to have $\tau_{\rm eff} = [1.53, 0.88, 0.39]$ at $z = [4.9, 4.0, 3.0]$ (Becker *et al.*, 2013) and have been convolved with a Gaussian with FWHM=7 $\rm km\,s^{-1}$.

the D15 and Tz9 models are displayed in the last two rows of Table 4.2. This suggests that measurements of u_0 with a total uncertainty of $\sim$ 28 (22) per cent are achievable with the the realistic (optimistic) data scenarios. Improving the precision of this measurement substantially will thus require both higher signal-to-noise data as well as careful forward modelling of the observational and numerical systematics.

4.5 Conclusions and discussion

In this work we examine the feasibility of constraining the integrated thermal history at $z > 5$ with the Lyα forest using the line of sight transmitted flux power spectrum. We suggest the cumulative energy deposited per proton, u_0, into a gas parcel at mean density at $5 \lesssim z \lesssim 12$ provides a useful parameterisation of the integrated thermal history in our simulations. We demonstrate this quantity correlates well with the underlying gas density power spectrum for $\Delta < 10$ over the scales where pressure smoothing acts in the low density IGM at $z \simeq 5$.

We also note that $z \simeq 5$ observations of the Lyα forest are well suited for this measurement, despite the fact that most of high quality data is available at lower redshifts. This is demonstrated in Figure 4.8, which displays the transmitted flux power spectrum for

the Tz12 and Tz7 models at $z \simeq 5,\ 4$ and 3. Recall that both models have very similar instantaneous temperatures at mean density, T_0, at $z < 6$ (see Figure 4.1). The differences associated with the thermal history at $z > 6$ are larger at higher redshift; the models are almost indistinguishable by $z = 3$ following the response of the low density gas to changes in the gas pressure and ongoing Hubble expansion. Furthermore, since He II reionisation is expected to heat the IGM at $z < 5$ (e.g. Becker *et al.*, 2011), higher redshift measurements that potentially avoid this additional heating are desirable for examining H I reionisation.

We next perform an MCMC analysis of the transmitted flux power spectrum using mock observations drawn from a suite of hydrodynamical simulations. Constraints on the slope of the temperature-density relation, γ, are generally weak at $z \simeq 5$. However, the degeneracy between thermal broadening and pressure smoothing can be broken at $z \simeq 5$ using the power spectrum at scales $\log(k/\mathrm{km^{-1}\,s}) > -1$. We estimate u_0 may be measured with a statistical uncertainty of ~ 20 (~ 8) per cent at $z \simeq 5$ with a redshift path length of $\Delta z = 4$ ($\Delta z = 20$) and a typical signal-to-noise per pixel of $\mathrm{S/N} = 15$ (50) using the power spectrum to scales $\log(k/\mathrm{km^{-1}\,s}) = -0.7$ (-0.5). We note, however, that the constraints are model dependent, and a larger grid of numerical models which explore the full range of the u_0–$\log T_0$ parameter space will be required for an in depth analysis of the observed power spectrum. Estimates for the expected systematic uncertainties ($\sim$ 15–25 per cent) are furthermore comparable to the statistical precision attainable with current data. Higher precision measurements are possible only if these systematic uncertainties are minimised in combination with improved signal-to-noise and increased path length.

Including systematic uncertainties, we conclude that currently available data alone should allow for a measurement of u_0 to within ~ 30 per cent at 68 per cent confidence. This corresponds to distinguishing between reionisation scenarios with similar instantaneous temperatures, T_0, at $z \simeq 5$, but an energy deposited per proton that varies by $\simeq$ 2–3 eV over the redshift interval $5 \leq z \leq 12$. For an initial $T \sim 10^4\,\mathrm{K}$ following reionisation, this corresponds to the difference between early ($z_{\mathrm{re}} = 12$) and late ($z_{\mathrm{re}} = 7$) reionisation in our models. When compared to predictions of models for the redshift evolution of the ionising background during reionisation – for which

u_0 should be straightforward to compute – this will provide an additional and novel constraint on the timing of the reionisation epoch.

Chapter 5

First constraints on the IGM integrated thermal history using Lyα forest power spectrum at $4.2 \leq z \leq 5.4$

5.1 Introduction

In Chapter 4, it was shown that measurements of the Lyα forest are an invaluable tool for inferring the timing, duration and nature of reionsation (Nasir *et al.*, 2017). The procedure involves comparing statistical properties of the Lyα forest to cosmological hydrodynamical simulations to deduce the thermal state of IGM. The Lyα flux power spectrum in particular is a powerful statistic, due to its sensitivity to both the instantaneous temperature and the integrated thermal history, as the rarefied IGM retains a memory of heating (Kulkarni *et al.*, 2015; Nasir, Bolton & Becker, 2016; Oñorbe, Hennawi & Lukić, 2017). Recently, Oñorbe *et al.* (2017) has independently performed a preliminary analysis of the integrated thermal history by utilizing the Lyα flux power spectrum measurements by Viel *et al.* (2013b) (hereafter V13) at $z = 5$–5.4. The authors have revisited the problem following the recent update to the Thomson scattering optical depth parameter, $\tau_{\rm e}$. The Planck Collaboration *et al.* (2016b) has reported

this parameter to be $\tau_{\rm e} = 0.058 \pm 0.012$, corresponding to a reionsation at redshift $z_{\rm re} = 8.8 \pm 0.9$. The analysis by Oñorbe *et al.* (2017) has found a consistent picture where galaxies drive reionsation, in agreement with the $\tau_{\rm e}$ reported by the Planck Collaboration *et al.* (2016b).

In this chapter, I present the first constraints on the IGM integrated thermal history using the flux power spectrum measurements by V13 and a new set of hydrodynamic simulations. These new runs self consistently model the thermal parameters (e.g $\log T_0$ and u_0) at $z = 4.2$–5.4, thus improving upon the previous method presented in Chapter 4.

5.2 Observational data

The observational data used in this analysis is from V13 and consists of 14 QSO spectra taken with the Keck High Resolution Echelle Spectrometer (HIRES) with a spectral resolution of $6.7\,{\rm km\,s^{-1}}$. Each spectrum has been split into two equal halves in pathlength and is normalised with a continuum which introduces systematic uncertainties in the mean flux up to 10-20%. The effective optical depth evolution, $\tau_{\rm eff}$, is taken from V13 (eq. 10), with $\tau_{\rm eff} = [1.01,\ 1.37,\ 1.92,\ 3.10]$ at $z = [4.2,\ 4.6,\ 5,\ 5.4]$, where the power spectrum measurements are provided at these median redshifts. The data points are given in 0.2 dex bins on the range $\log k/({\rm km^{-1}\,s}) = [-2.9, -1.1]$, although only 7 datapoints within the range $\log k/({\rm km^{-1}\,s}) = [-2.3, -1.1]$ are used for the analysis here. This corresponds to the scales probed by the hydrodynamic simulations which are performed with $10h^{-1}{\rm cMpc}$ boxes. To obtain the error estimates on the power spectrum the bootstrap technique was used by V13 with a 30% increment in the error bars to account for the cosmic variance (Rollinde *et al.*, 2013).

5.3 Methodology

5.3.1 Hydrodynamical simulations

In order to perform the analysis, a series of simulations with a variety of self-consistent thermal histories are used as summarised in Table 5.1. These simulations were per-

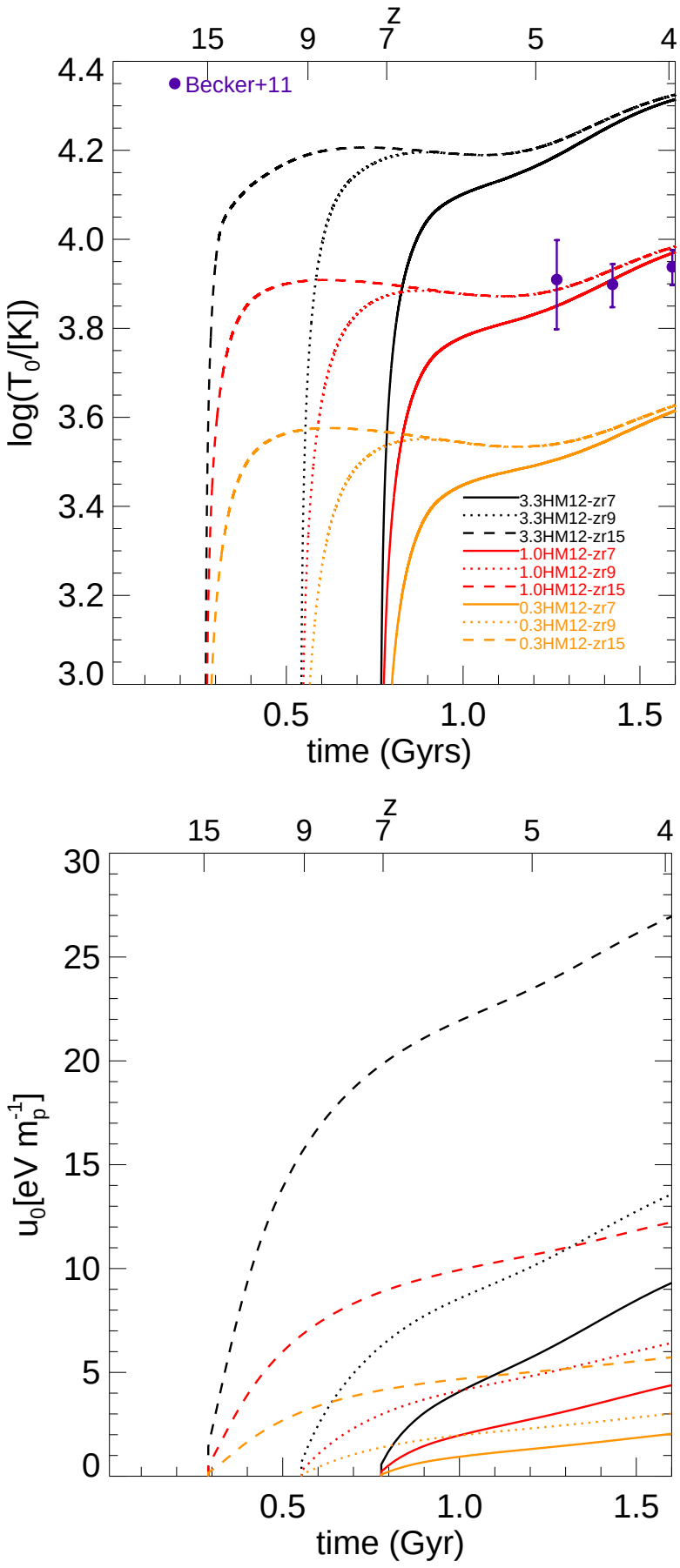


Figure 5.1: The thermal histories for the simulations listed in Table 5.1. *Top:* The logarithm of the temperature at mean density, T_0, as function of time, overlaid with the observational measurements from Becker *et al.* (2011), evaluated at their fiducial γ values along with 2σ errors. *Bottom:* The cumulative energy per proton deposited in a gas parcel at mean density as a function of time.

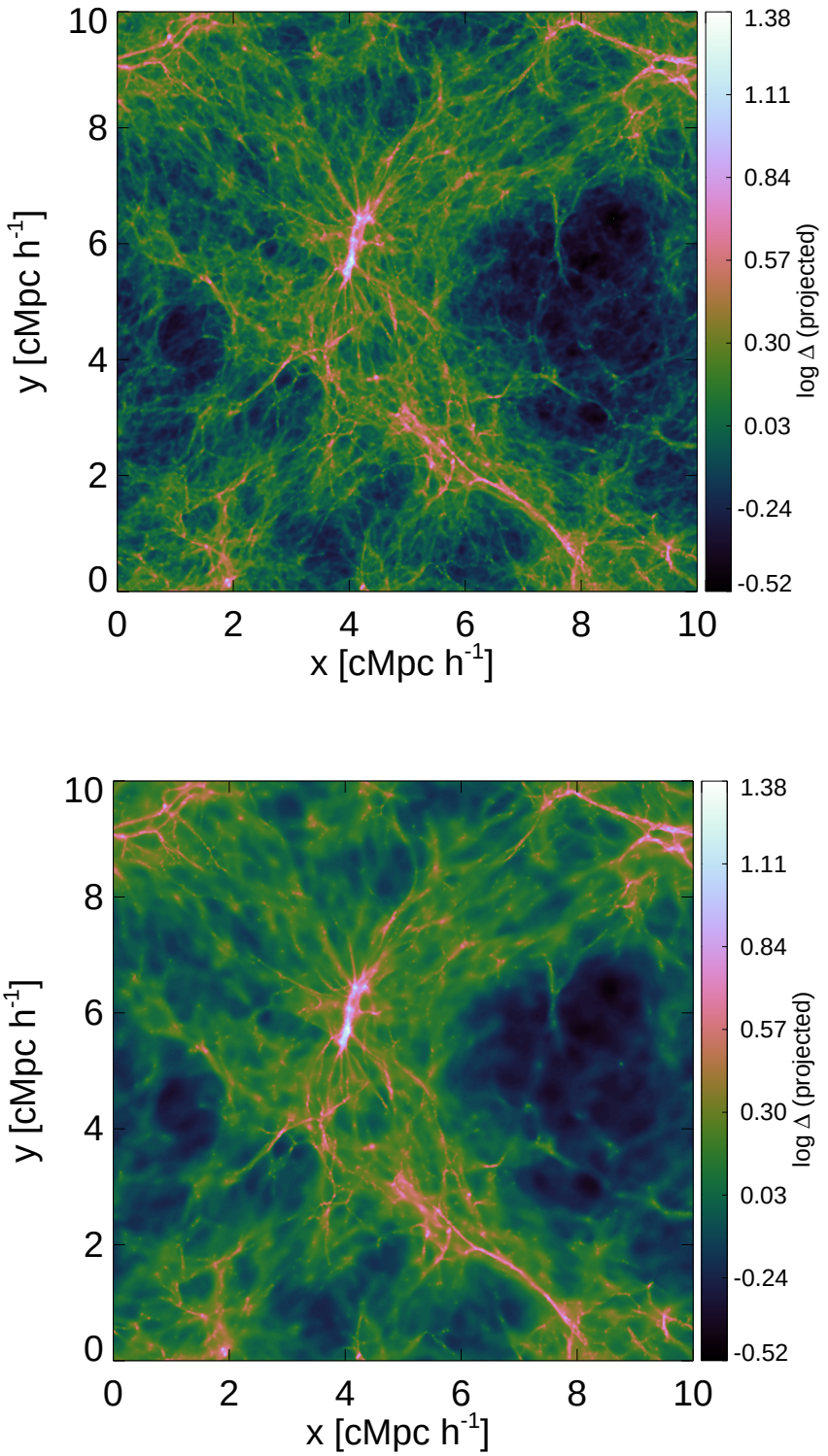


Figure 5.2: A comparison of logarithmic projected gas density relative to mean density between two models with extreme values of u_0 . The model 0.3HM12-zr7 with $u_0 = 1.2\mathrm{eV\,m_p^{-1}}$ (*top panel*) and 3.3HM12-zr15 with u_0 =23.2eV $\mathrm{m_p^{-1}}$ (*bottom panel*) are shown. The projection is performed along the z-axis over a scale of $5h^{-1}$Mpc. Note the smoother gas distribution in the model with larger u_0 .

Table 5.1: The hydrodynamical simulations used in this chapter. All models have a box size of $10h^{-1}\,\mathrm{cMpc}$, 512^3 gas and dark matter particles and a gas particle mass of $9.97 \times 10^4 h^{-1} M_\odot$. The columns in the table list the model name, redshift of reionisation, $z_{\rm re}$, scaling factor ξ for the photoheating rates, $\log T_0$, γ and u_0, at $z = 5$. The values are estimated as in Chapter 4.

Model	$z_{\rm re}$	ξ	$\log(\mathrm{T_0^{z=5}/K})$	$\gamma^{z=5}$	$u_0^{z=5}\,\mathrm{eV\,m_p^{-1}}$
1.0HM12-zr15	15	1	3.87	1.53	10.6
1.0HM12-zr9	9	1	3.87	1.51	4.7
1.0HM12-zr7	7	1	3.82	1.50	2.7
0.3HM12-zr15	15	0.3	3.53	1.51	5.0
0.3HM12-zr9	9	0.3	3.53	1.49	2.3
0.3HM12-zr7	7	0.3	3.50	1.52	1.3
3.3HM12-zr15	15	3.3	4.19	1.52	23.2
3.3HM12-zr9	9	3.3	4.19	1.50	9.9
3.3HM12-zr7	7	3.3	4.14	1.48	5.5

formed with the same code used for the Sherwood simulation suite (Bolton *et al.*, 2017), also described in Chapter 2 of this thesis. For this work the simulations implement the QUICKLYA method for star formation and evolve up to redshift $z_{\rm end} = 4$. Most of the runs are done in a $10h^{-1}\mathrm{cMpc}$ box and with 512^3 gas and dark matter particles. The exceptions are the runs 40-2048, 20-1024 and 10-512 which are used for box size and resolution convergence tests. Furthermore, two additional runs, 10-768 and 10-256 were used to investigate the effect of mass resolution on the power spectrum.

The UV background (UVB) in the simulations is based on the Haardt & Madau (2012) (hereafter HM12) synthesis model with contributions from star forming galaxies and quasars, resulting in reionsation at $z = 15$. However, to obtain thermal histories with different reionisation redshifts $z_{\rm re}$, a simple translation and rescaling of the UVB with redshift is performed to give reionsation at $z_{\rm re} = [7,\ 9,\ 15]$. Each model reaches similar temperatures at $z = 4$. This way the effect of u_0 is isolated from T_0 .

By contrast, to obtain thermal histories with the same $z_{\rm re}$, but reaching different temperatures at $z = 4$, the photoheating rates are scaled proportionally by a constant factor, ξ (listed in the Table 5.1). Figure 5.1 displays the evolution of the temperature at mean density, and the cumulative energy deposited per proton,u_0 , for the simulations summarised in Table 5.1. The T_0 is chosen at $z = 4$, such that the models bracket the observational data from Becker *et al.* (2011). The simulations encompass temperatures in the range $\log(T_0/K) = 3.5$–4.1 and a cumulative energy deposited per proton,

$u_0 = 2.3$–$23.3 \mathrm{eV\,m_p^{-1}}$ at $z = 5$. Note that there is positive a correlation between T_0 and u_0 , due to the upscaling of the photoheating rates.

The projected gas densities are shown for the models with the most extreme values of u_0 in Figure 5.2. The effect of the integrated heating is clearly visible, with the model with the highest u_0 showing less structure relative to the low u_0 model, due to increased pressure smoothing. These web like structures are traced by neutral hydrogen and correspond to absorption lines in the Lyα forest.

To calculate the flux power spectrum, 5000 random lines-of-sight were extracted parallel to the box boundaries, by analysing the snapshots at four different redshifts, $z = [4.2,\ 4.6,\ 5,\ 5.4]$. The mock spectra are rescaled to match the $\tau_{\rm eff}$ given by V13. Finally, the power spectrum for the fractional mean transmission $F/\langle F\rangle - 1$ is computed as in Chapter 4.

5.3.2 The MCMC

In order to predict the u_0 for observational data, a Bayesian MCMC approach is adopted as discussed in Chapter 4. The u_0 for the V13 power spectrum at $z = [4.2,\ 4.6,\ 5,\ 5.4]$, is obtained with a grid of models constructed from the hydrodynamical simulations. Initially, the four parameters $\log T_0$, u_0 , γ and $\tau_{\rm eff}$, are used to construct the grid of models in context to Chapter 4. The thermal histories for these simulations are chosen in such a way that no post-processing is required to construct the grid of models, as each simulation serves as a self-consistent unique data point in the $\log T_0$ -u_0 plane.

However, post-processing is used to obtain the models in the direction of other parameters. The slope of the $T - \Delta$ relationship is varied over the plausible range of values $\gamma = 1.7$–0.9 with 0.1 spacing. This is done by transforming the $T - \Delta$ plane as in Chapter 4. The $\tau_{\rm eff}$ is varied in the range 1.3-0.7 (with 0.1 spacing, where the central value is given by V13) times the effective optical depth. All together, there are $9 \times 9 \times 7 = 567$ grid points in the parameter space. Furthermore, the mock spectra extracted from a model at a given point in the grid are post-processed by convolving with an instrumental profile of FWHM=$7\,\mathrm{km\,s^{-1}}$ and rebinned to a pixel scale of $3\mathrm{km\,s^{-1}}$. Gaussian distributed noise of $\mathrm{S/N} = 20$ per pixel is added and the spec-

tra are iteratively rescaled to match $\tau_{\rm eff}$. For $\tau_{\rm eff}$, a Gaussian prior with mean given by V13 and with a 1σ uncertainty corresponding to 4 per cent of the mean is used. Further, a multi-linear interpolation is performed to obtain the power spectrum at any given point in the parameter space. Following V13, the power spectrum is binned on equally spaced intervals on the range $\log k/(\mathrm{km}^{-1}\,\mathrm{s}\,) = [-2.3, -1.1]$. Note that the box size of simulations limits the analysis to $\log k/(\mathrm{km}^{-1}\,\mathrm{s}\,) >= -2.3$. Finally, 10^4 accepted chains from the Markov chain iterations are obtained, with 1000 discarded as the burn-in phase.

Although not shown, it was verified that the marginalised one dimensional and two dimensional posterior distributions of parameters for 1.0HM12-zr15 are successfully recovered. As the model lies on the grid, this serves as a consistency check for the method. As in Chapter 4, the recovered distributions and constraints on parameters depends on the k-scales over which the mock data is constructed. Limiting the power spectrum to scales $\log k/(\mathrm{km}^{-1}\,\mathrm{s}\,) <= -1.1$ results in a broader $\log T_0$ distribution.

5.3.3 Improvements in the method

In this section, new additions to the methodology used in Chapter 4 are discussed. Errors due to the box size and mass resolution convergence of the simulations are corrected in the grid of models. In addition, a model for UV background fluctuations as implemented by Becker *et al.* (2015) is included. This incorporates spatial fluctuations in the UV background at high redshift due to rare sources such as quasars (e.g. Chardin, Puchwein & Haehnelt (2017)).

In Figure 5.3, the power spectrum for the 10-256 and 10-512 models relative to the 10-768 simulation is shown. These runs implement the HM12 UVB, resulting in reionisation at $z_{\rm re} = 15$. Note that increased mass resolution results in a small correction up to $\sim 5\%$ at the smallest scales considered by V13. To implement this correction, a scale factor, $P_{\mathrm{F},10-768}/P_{\mathrm{F},10-512}$, is introduced to the previous grid of models. The box size correction for 10-512 model is also $\sim 5\%$ as shown in Figure 5.4. For the box size correction the scale factor is $P_{\mathrm{F},40-2048}/P_{\mathrm{F},10-512}$.

In order to incorporate UV fluctuations expected due to the decreasing mean free path

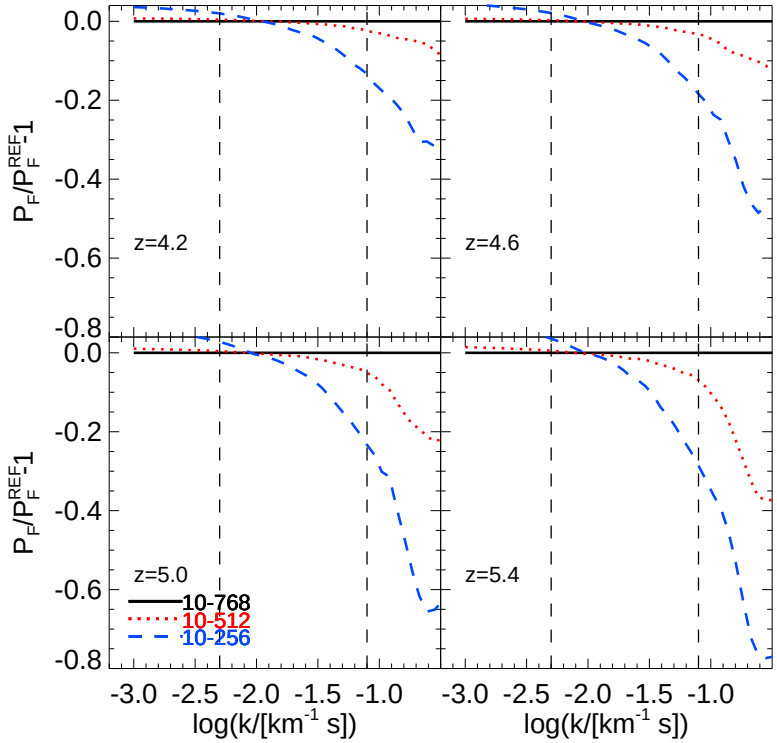


Figure 5.3: The transmitted Lyα flux power spectrum with respect to the reference model 10-768 at $z = [4.2, 4.6, 5, 5.4]$. Convergence with mass resolution for a fixed box size of $10h^{-1}\mathrm{cMpc}$ is displayed. The dashed lines mark the k-scales over which the V13 power spectrum is measured.

of ionizing photons towards higher redshifts and rare bright sources (like quasars), the approach of Becker *et al.* (2015, Section 4.2) is used. A similar approach was also adopted in Viel *et al.* (2013b). First, a large volume of $490h^{-1}\mathrm{cMpc}$ (several times the mean free path of H I ionising photons at $z > 4.2$) is obtained by tiling up the simulation box. All the haloes in the box are identified by using the friends-of-friends halo finder. Further, each halo is assigned a luminosity function by Monte Carlo sampling the Hopkins, Richards & Hernquist (2007) B-band quasar luminosity function at a given redshift. A rank ordering of halo mass and quasar luminosity ensures that the brightest quasars are assigned to massive haloes. The lowest B-band magnitude is chosen at $M_\mathrm{B} = -22$. The ionising luminosities are obtained from the B-band luminosities for the quasars by using the Madau, Haardt & Rees (1999) spectral energy distribution.

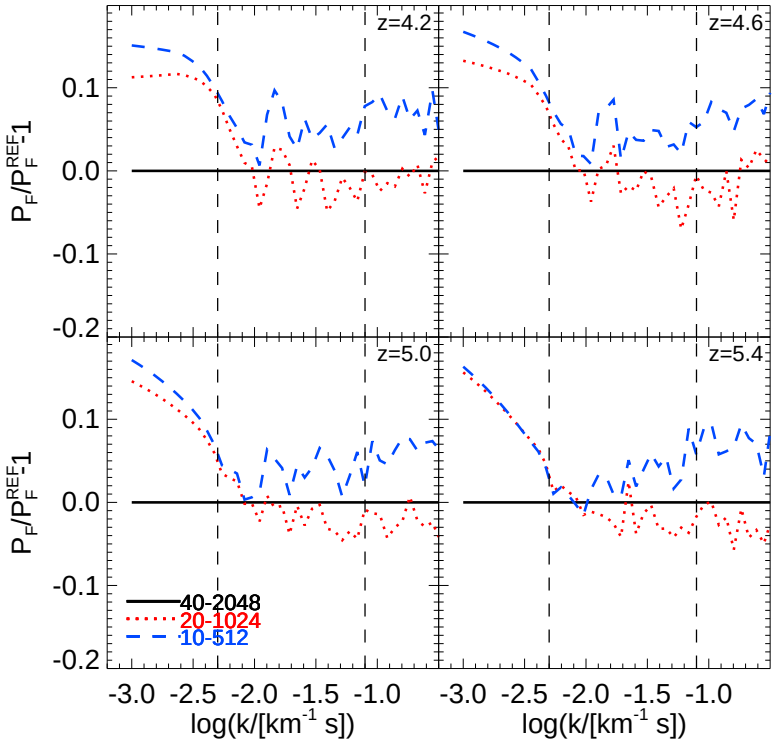


Figure 5.4: The transmitted Lyα flux power spectrum with respect to the reference 40-2048 run at $z = [4.2, 4.6, 5, 5.4]$. Convergence with box size for a fixed mass resolution of $M_{\rm gas} = 5.38 \times 10^5 h^{-1} M_\odot$ is displayed. The dashed lines show the k-scales over which the V13 power spectrum is measured.

$$L_\nu \propto \begin{cases} \nu^{-0.3} & (2500 < \lambda < 4600\,\text{Å}), \\ \nu^{-0.8} & (1050 < \lambda < 2500\,\text{Å}), \\ \nu^{-\alpha_{\rm s}} & (\lambda < 1050\,\text{Å}), \end{cases}$$

where $\alpha_{\rm s}$ is the extreme UV spectral index, chosen by Monte Carlo sampling a Gaussian with mean 1.7 and standard deviation of $\sigma = 0.61$ over the range $1.7 - 3\sigma \leq \alpha_{\rm s} \leq 1.7 + 3\sigma$ (Lusso *et al.*, 2014). Once all the luminosities of the quasars and their spectral energy distribution are specified, the specific intensity, $J(\mathbf{r}, \nu)$, of the UVB is computed using eq. (3) in Becker *et al.* (2015) at each spatial position along lines-of-sight for 1–4 Ryd photons.

$$J(\mathbf{r}, \nu) = \frac{1}{4\pi} \sum_{i=1}^{N} \frac{L_i(\mathbf{r}_i, \nu)}{4\pi |\mathbf{r}_i - \mathbf{r}|^2} e^{-\frac{|\mathbf{r_i}-\mathbf{r}|}{\lambda_{\rm HI}} \left(\frac{\nu}{\nu_{\rm HI}}\right)^{-3(\beta-1)}}, \tag{5.1}$$

where $\lambda_{\rm HI}$ is the mean free path for ionising photons, $\nu_{\rm HI}$ is the frequency of photons

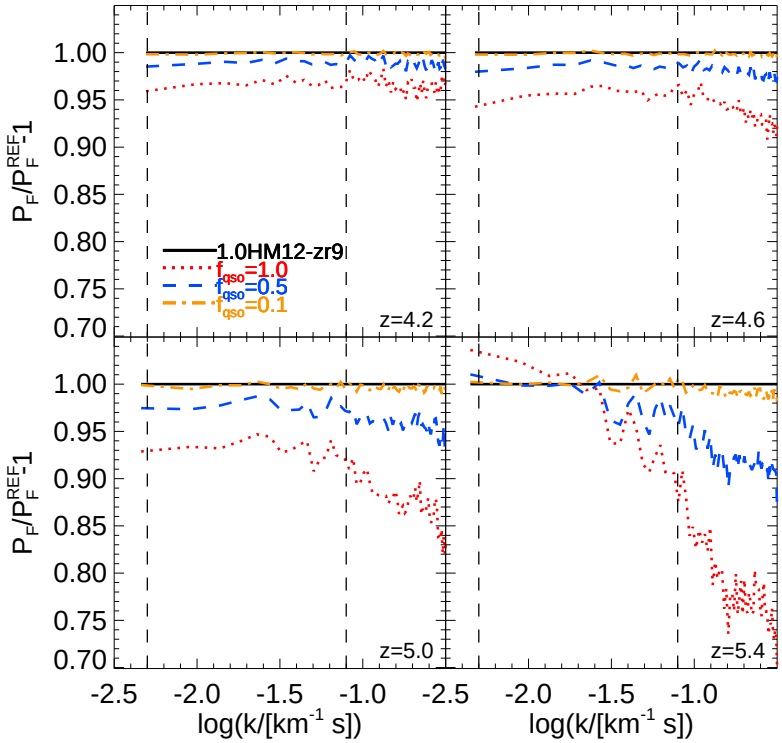


Figure 5.5: The transmitted Lyα flux power spectrum with respect to 1.0HM12-zr9 for different quasar contributions to the UVB at $z = [4.2,\ 4.6,\ 5,\ 5.4]$. The vertical dashed lines encompass the corresponding scales over which V13 power spectrum is measured. Note that $f_{\rm qso} = 1$ implies all the UVB is from quasars.

at the H I ionisation edge and $\beta = 1.3$ is the slope of H I column density distribution function. The above sum is made over all the sources with $|\mathbf{r}_i - \mathbf{r}| \leq L_{\rm box}/2$ within periodic boundaries, where $L_{\rm box} = 490h^{-1}{\rm cMpc}$. The mean free path to ionising photons is from Worseck *et al.* (2014)

$$\lambda_{\rm mfp}(z) = 130\left(\frac{1+z}{5}\right)^{-4.4} h^{-1}{\rm Mpc}, \tag{5.2}$$

where $\lambda_{\rm mfp} = 58h^{-1}$Mpc at $z = 5$. Therefore, this simple method provides a first order correction to the complex coupling between the density and ionising radiation field. The H I photoionisation rates, $\Gamma(\mathbf{r})$, are calculated using the photoionisation cross section $\sigma_{\rm HI}(\nu)$ as

$$\Gamma(\mathbf{r}) = 4\pi \int_{\nu_{912}}^{4\nu_{912}} \frac{d\nu}{h\nu} J(\mathbf{r},\nu)\sigma_{\rm HI}(\nu), \tag{5.3}$$

The total photoionisation rate is then given as $\Gamma_{\rm tot}(\mathbf{r}) = \Gamma(\mathbf{r}) + (1 - f_{\rm qso})\Gamma_{\rm HM12}$, where $f_{\rm qso}$ is the fraction of $\Gamma_{\rm tot}$ from quasars and $\Gamma_{\rm HM12}$ is the spatially uniform HM12 photoionisation rate. The H I number density, $n_{\rm HI}$, in the simulations is then rescaled as $n_{\rm HI}(\mathbf{r}) \propto 1/\Gamma_{\rm tot}(\mathbf{r})$. As the scaling is in physical space, the H I optical depths in redshift space are recalculated for the same line-of-sight with the updated H I number densities.

To incorporate the effect of UV fluctuations from quasars, the power spectrum is computed at three different values for the quasar fraction, $f_{\rm qso} = [0.1,\, 0.5,\, 1]$. The uniform model serves as the $f_{\rm qso} = 0$ case. In Figure 5.5, the power spectrum for these models relative to the native 1.0HM12-zr9 is shown. Note that $f_{\rm qso} = 1$ implies that all of the contribution to the UVB is from quasars. It is clear that for the most extreme case, $f_{\rm qso} = 1$, the correction is $\sim 5\%$ at $z = 4.2$, increasing up to $\sim 7\%$ at higher redshifts. The reduction in power is almost uniform on all scales (the k-scales where the power spectrum is measured by V13 are shown as vertical dashed lines), except at $z = 5.4$, due to the increased opacity of the IGM to ionising photons. We have implemented $f_{\rm qso}$ as a free parameter in the MCMC. A flat prior is chosen with end values at $f_{\rm qso} = [0,\, 1]$.

5.4 Results

The constraints on the integrated thermal history from the V13 observational data are shown in Table 5.2 for u_0 and $\log T_0$. The V13 data points (blue circles) and the MCMC best fits (red curves) at $z = [4.2,\, 4.6,\, 5,\, 5.4]$ are shown in Figure 5.6. Table 5.2 shows the constraints and individually lists the corrections for box size, mass resolution and the incorporation of fluctuations in UVB, parameterised as $f_{\rm qso}$.

The recovered one dimensional and two dimensional probability distributions of parameters for V13 data at $z = 5$ are shown in Figure 5.7. It is clear that the γ and $f_{\rm qso}$ have relatively flat distributions, implying the power spectrum is insensitive to these parameters. This is expected, as since the power spectrum is not very sensitive to $f_{\rm qso}$ on relevant the k-scales, as shown in Figure 5.5. The errors on the observational data are also quite large compared to box size and mass resolution corrections.

Table 5.2: Predicted constraints on $\log(\mathrm{T}_0)$ and u_0 obtained for the V13 power spectrum at $z = [4.2,\ 4.6,\ 5,\ 5.4]$. The values correspond to the median of the marginalised posterior distribution for each parameter, along with the 68 and 95 per cent credible intervals. From left to right, the columns gives the best MCMC fits, fits with box size corrections only, fits with mass resolution corrections only and fits with UV background corrections only (see the text for details).

	MCMC best fits		Box Size		Resolution		UV background	
z_o	$\log(\mathrm{T}_0/\mathrm{K})$	$u_0\mathrm{eV\,m_p^{-1}}$	$\log(\mathrm{T}_0/\mathrm{K})$	$u_0\mathrm{eV\,m_p^{-1}}$	$\log(\mathrm{T}_0/\mathrm{K})$	$u_0\mathrm{eV\,m_p^{-1}}$	$\log(\mathrm{T}_0/\mathrm{K})$	$u_0\mathrm{eV\,m_p^{-1}}$
		$z_\mathrm{o} \leq z \leq 12.0$						
4.2	$3.99^{+0.06}_{-0.07}\ (^{+0.13}_{-0.17})$	$7.3^{+1.7}_{-1.6}\ (^{+3.2}_{-2.5})$	$3.99^{+0.06}_{-0.08}\ (^{+0.12}_{-0.18})$	$7.3^{+1.6}_{-1.6}\ (^{+3.1}_{-2.6})$	$4.00^{+0.06}_{-0.07}\ (^{+0.13}_{-0.16})$	$7.5^{+1.7}_{-1.7}\ (^{+3.1}_{-2.8})$	$4.00^{+0.06}_{-0.07}\ (^{+0.12}_{-0.17})$	$7.3^{+1.7}_{-1.6}\ (^{+3.1}_{-2.5})$
4.6	$3.96^{+0.07}_{-0.06}\ (^{+0.13}_{-0.15})$	$6.6^{+1.1}_{-1.1}\ (^{+2.1}_{-1.8})$	$3.94^{+0.07}_{-0.07}\ (^{+0.13}_{-0.15})$	$6.4^{+1.1}_{-1.1}\ (^{+2.0}_{-1.8})$	$3.96^{+0.07}_{-0.07}\ (^{+0.13}_{-0.17})$	$6.5^{+1.2}_{-1.1}\ (^{+2.2}_{-1.8})$	$3.95^{+0.07}_{-0.07}\ (^{+0.13}_{-0.15})$	$6.5^{+1.1}_{-1.1}\ (^{+2.0}_{-2.4})$
5.0	$3.85^{+0.13}_{-0.13}\ (^{+0.23}_{-0.23})$	$5.0^{+0.9}_{-0.9}\ (^{+1.9}_{-1.6})$	$3.83^{+0.12}_{-0.12}\ (^{+0.22}_{-0.22})$	$4.8^{+0.9}_{-0.8}\ (^{+1.9}_{-1.6})$	$3.84^{+0.12}_{-0.12}\ (^{+0.23}_{-0.22})$	$5.0^{+0.8}_{-0.8}\ (^{+1.8}_{-1.6})$	$3.81^{+0.11}_{-0.12}\ (^{+0.23}_{-0.21})$	$4.7^{+0.8}_{-0.8}\ (^{+1.8}_{-1.6})$
5.4	$3.87^{+0.16}_{-0.16}\ (^{+0.25}_{-0.29})$	$4.7^{+1.4}_{-1.1}\ (^{+2.9}_{-2.1})$	$3.87^{+0.16}_{-0.16}\ (^{+0.25}_{-0.28})$	$4.8^{+1.3}_{-1.2}\ (^{+2.9}_{-2.2})$	$3.90^{+0.15}_{-0.16}\ (^{+0.22}_{-0.29})$	$5.1^{+1.3}_{-1.0}\ (^{+3.0}_{-2.1})$	$3.86^{+0.16}_{-0.16}\ (^{+0.26}_{-0.28})$	$4.5^{+1.3}_{-1.2}\ (^{+2.9}_{-2.2})$

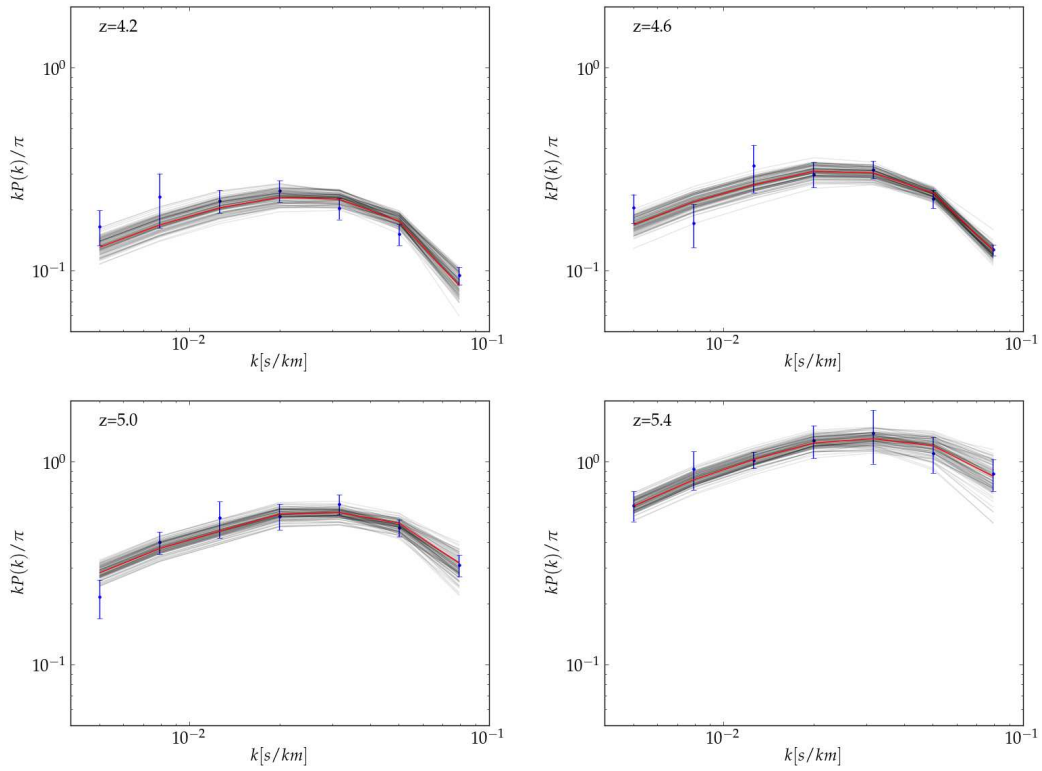


Figure 5.6: The MCMC best fits for the V13 flux power spectrum data points at $z = [4.2, 4.6, 5, 5.4]$. The observational data points are shown as blue circles along with 1σ uncertainties. The red curves shows the MCMC best fit overlaid with the corresponding power spectrum for 100 random samples selected from the accepted chains, shown in grey.

The constraints on $\log T_0$ from the V13 observations at $z = [4.2, 4.6, 5, 5.4]$ are consistent with the Becker *et al.* (2011) data points (violet circles) shown in Figure 5.1. In addition to $\log T_0$, the constraints on u_0 are bracketed at $u_0 = 4.7$–$7.3\mathrm{eV\,m_p^{-1}}$ at $z = 5.4$–4.2. Broadly, three models, namely 3.3HM12-zr7, 0.3HM12-zr15 and 1.0HM12-zr9 (see Table 5.1 for corresponding u_0 at $z = 5$) are consistent with these values. However, the combined constraints from $\log T_0$ and u_0 suggests a thermal history (1.0HM12-zr9) with HM12 rates and reionsation at $z = 9$, provides a best fit. The results are in agreement with the previous findings by Oñorbe *et al.* (2017), who suggest a model with a reionsation starting at a redshift of $z \sim 9$ and duration of $\Delta z = 2.59$ is consistent with the V13 flux power spectrum at $z = [5 - 5.4]$. This reionsation model has $u_0 = 4.24\mathrm{eV\,m_p^{-1}}$ at $z \sim 5$, in agreement with the estimates here, $u_0 = 5.0^{+0.9}_{-0.9}\mathrm{eV\,m_p^{-1}}$ (see Table 5.2). This result also indicates that reionsation is less likely to be dominated by AGN (Madau & Haardt, 2015) and disfavours such models, as these predict more heat injection into the IGM and higher values for u_0 (see also D'Aloisio *et al.* (2017)). For reference, the u_0 for the Haardt & Madau (2001)

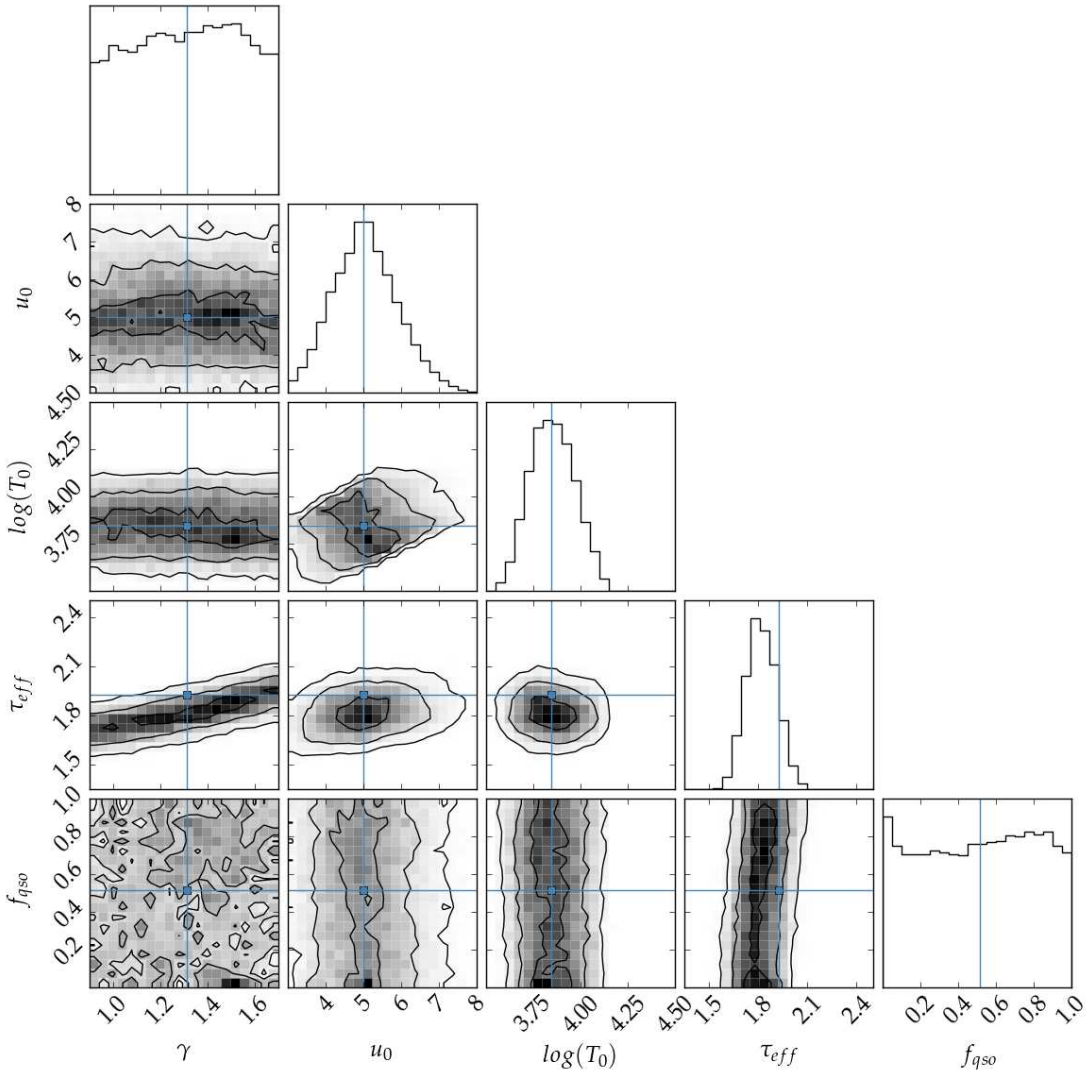


Figure 5.7: The contours display the two dimensional probability distributions for the parameters $\log T_0$, u_0, γ, $\tau_{\rm eff}$ and $f_{\rm qso}$ recovered from the V13 flux power spectrum at $z = 5$, once corrected for resolution and box size. The joint 1σ, 2σ and 3σ contours are shown in black with the number density of points shown as shades of grey. The black curves display the one dimensional marginalised posterior distributions for each parameter. The blue lines show the MCMC best fit for each parameter.

galaxies and quasars and quasars only UVB models are $u_0 = 5.8 - 7.7 \mathrm{eV\,m_p^{-1}}$ and $u_0 = 9.4 - 11.4 \mathrm{eV\,m_p^{-1}}$, respectively at $z = [5.4 - 4.2]$. Clearly, the heat injection by the quasar model is less favoured by the u_0 estimates from the V13 data. Further, the galaxies and quasars model is consistent with the u_0 estimates from the V17, within 1σ.

This analysis further suggests an optimistic picture where useful constraints on u_0 and T_0 can already be obtained from the existing data at wavenumbers $\log k/(\mathrm{km^{-1}\,s}) < -1$. Pushing the observational measurements to smaller scales in combination with simulations with self-consistent thermal histories, should improve constraints further

(Nasir, Bolton & Becker, 2016).

5.5 Conclusions

In this chapter, the initial constraints on the integrated thermal history using the Lyα forest flux power spectrum measurements and a new set of hydrodynamical simulations, which allow self-consistent exploration of the parameter-space in $\log T_0$ and u_0 are obtained. The results are in agreement with recent Planck Collaboration *et al.* (2016b), $\tau_{\rm e}$ measurements and the preliminary study by Oñorbe *et al.* (2017). The constraints favour a reionsation model with reionsation at $z = 9$. The integrated heating is bracketed by $u_0 = 4.7 - 7.3\,{\rm eV\,m_p^{-1}}$ at $z = 5.4$–4.2. These low values for u_0 favour a more conventional reionsation scenario dominated by galaxies rather then quasars.

In the MCMC analysis, the uncertainties due to box size, mass resolution and spatial fluctuations in the UV background are also corrected for. Including these systematics introduced small additional uncertainties on the $\log T_0$ and u_0 constraints. In conclusion, the u_0 is a useful parameterisation for the integrated heating during reionsation and can distinguish among various reionisation models, providing insight into the nature of the sources responsible for it. In future, high resolution measurements have the potential to improve on estimates by reaching small scales ($\log(k/{\rm km^{-1}\,s}) > -1$), due to the sensitivity of the integrated heating on the small-scale cut-off in the power spectrum (Nasir, Bolton & Becker, 2016; Oñorbe *et al.*, 2017).

Chapter 6

Summary & future work

In this thesis, the properties and the thermal state of IGM are examined using cosmological simulations of the Lyα forest. In Chapter 1, I emphasized that the IGM is a rich repository for studying reionsation, the evolution of metagalactic UV background and the impact of galactic feedback from AGN and supernovae. However, I also highlighted the challenges faced by current hydrodynamical simulations to accurately model the properties of the Lyα forest at low ($z \lesssim 2$) and high ($z \gtrsim 5$) redshifts.

In Chapter 2-3, the impact of feedback on the statistical properties of the low redshift Lyα forest are examined. I presented results which highlighted the apparent discrepancies with current observations. At high redshift (see Chapter 4-5), I focussed on the constraints on the timing of reionsation and the integrated thermal history of IGM and I presented the first constraints on the integrated thermal history. In this chapter, I will summarise these key results and discuss the possible extensions of this work. I will highlight current and potential future developments in both observations and cosmological simulations, which will progress the field in the coming decade.

6.1 The impact of feedback on the low redshift Lyα forest

In Chapter 2, statistical quantities estimated from low redshift Lyα forest simulations with various feedback prescriptions are presented and compared with recent observa-

tions. The Lyα CDDF and the velocity line widths distribution predicted by the simulations are in disagreement with observations. The simulations predict a shallower slope for CDDF with too few high column density systems ($N_{\rm HI} > 10^{14}\,{\rm cm}^{-2}$). Further, the velocity line widths are too narrow compared to observations and the disagreement is larger for simulations performed with higher mass resolution. The impact of galactic feedback in the simulations does not fully resolve this disagreement. Improving the agreement might involve a more efficient ejection of gas into the IGM, that keeps the temperatures low enough to enable contribution to the Lyα forest.

In Chapter 3, the numerical convergence with box size and mass resolution of quantities derived from the low redshift Lyα forest simulations are discussed. The Lyα CDDF is well converged for the absorbers at $N_{\rm HI} = 10^{13} - 10^{14}\,{\rm cm}^{-2}$, but the velocity line widths are significantly overestimated for simulations performed with lower mass resolution. The $\tau_{\rm eff}$ shows excellent convergence, to within $\sim 2\%$ with box size and $\sim 5\%$ with mass resolution. The flux PDF is converged to within 20% for mass resolution, 5% for box size, the flux power spectrum is converged within $\sim 5\%$ with box size and within 30% with mass resolution.

6.2 Constraints on the integrated thermal history of IGM with the high redshift Lyα forest

In Chapter 4-5, I carefully laid out the key steps involved in posing the first constraints on the integrated thermal history of the IGM using cosmological hydrodynamical simulations. In Chapter 4, the correlation of the integrated thermal history with the line of sight transmitted flux power spectrum at $z \simeq 5$ is established. By utilizing this fact, the integrated thermal history of the IGM was modelled by using a set of hydrodynamical simulations with a variety of thermal histories. Finally, the predicted constraints on the integrated thermal history are presented. This can be measured with a statistical uncertainty of $\sim$20 per cent utilizing mock observations at $z \simeq 5$.

In Chapter 5, I expand on this work by using a new set of hydrodynamical simulations which allow a self-consistent exploration of $\log T_0$ -u_0 parameter-space. Being aware

of systematics at these redshifts, I also correct the grid of models for the box size and mass resolution of the simulations, and incorporate a model to account for fluctuations in the UV background due to quasars. The integrated thermal history constraints for the recent flux power spectrum measurements by Viel *et al.* (2013b) are bracketed by $u_0 = 4.7 - 7.3\mathrm{eV\,m_p^{-1}}$ at $z = 5.4$–4.2. These estimates favor a galaxy driven reionsation scenario, in agreement with a redshift of reionsation at $z = 9$.

Future measurements have the potential to improve the constraints by probing on to smaller scales in the power spectrum (Nasir, Bolton & Becker, 2016; Oñorbe *et al.*, 2017).

6.3 Outlook

There has been a remarkable success, in reproducing the properties of H I Lyα forest for low density gas in the IGM at intermediate redshifts (McDonald *et al.*, 2000; Croft, 2004; Altay *et al.*, 2011; Palanque-Delabrouille *et al.*, 2013; Rollinde *et al.*, 2013; Viel *et al.*, 2013b; Bolton *et al.*, 2017). However, there is still room for additional precision at these epochs. Extending our understanding of the IGM would require developments at both the observational and simulation fronts. The future prospects for the field are excellent. Here, I will highlight these prospects and mention the key science questions which can be addressed.

6.3.1 High redshift quasars

The high redshift quasars, $z \gtrsim 6$ are a powerful probe for establishing the H I reionsation history of the IGM (for review Mortlock (2016)). About 17 years ago, the first quasar at $z \simeq 5.8$ was discovered by the Sloan Digital Sky Survey (SDSS) (Fan *et al.*, 2000). Since then, there has been a significant increase in the number count of these objects, pioneered by SDSS (Fan *et al.*, 2006b; Jiang *et al.*, 2015) and followed by the Canada France High redshift Quasar Survey (CFHQS) (Willott *et al.*, 2010) and the UKIRT Infrared Deep Sky Survey (UKIDSS), including the only quasar at $z = 7.1$ (Mortlock *et al.*, 2011). More recently, the Panoramic Survey Telescope & Rapid Response

System 1 (Pan-STARRS1) (Bañados *et al.*, 2014, 2016), the VISTA Kilo-Degree Infrared Galaxy (VIKING) survey (Venemans *et al.*, 2013, 2015), the Dark Energy Survey (DES) (Reed *et al.*, 2015), and the Subaru High-z Exploration of Low-Luminosity Quasars (SHELLQ) are making their contributions (Matsuoka *et al.*, 2016). Finding these high redshift quasars will prove a useful tool for reionsation if it is possible to obtain moderate to high resolution spectra. In the coming years, there will be a remarkable upgrade in this regard, due to the large collecting area of the Thirty Meter Telescope (TMT), the Giant Magnellan Telescope (GMT) and the European Extremely Large Telescope (EELT), improving not only the number counts but also sensitivity (Becker, Bolton & Lidz, 2015). In conjunction, with the James Webb Space Telescope (JWST), observing the high redshifts galaxy population up to redshift $z \sim 10$–15 (Yan *et al.*, 2016), this would provide powerful constraints on the cosmic reionsation.

6.3.2 21 cm radiation

The 21 cm radiation arises from a "spin-flip" line in hydrogen, which accounts for 76% of the baryons in the Universe by mass. This transition is the target for low-frequency radio telescopes across the globe. The instruments, such as the Precision Array for Probing the Epoch of Reionization (PAPER) in South Africa, Murchison Widefield Array (MWA) in Australia, the Low Frequency Array (LOFAR) in Netherlands, the Giant Meterwave Radio Telescope (GMRT) in India and second generation radio telescopes, such as the Hydrogen Epoch of Reionization Array (HERA) and the international Square Kilometre Array (SKA) are aiming to detect the first signal of redshifted 21 cm radiation (Paciga *et al.*, 2013; Parsons *et al.*, 2014; Liu & Parsons, 2016; Patil *et al.*, 2017). The plan for the observations is to map the neutral hydrogen from the end of reionsation up to $z = 10$ or beyond, providing a direct probe on the process of reionsation. These observations would fill the gap in our understanding of Universe after the CMB, when the first ionising sources appear (for a review see Pritchard & Loeb (2012)). Together with the Lyα forest observations, 21 cm would provide detailed constraints on the timing, duration, structure and sources of reionsation (Pritchard, Loeb & Wyithe, 2010; Becker, Bolton & Lidz, 2015; Kulkarni *et al.*, 2017).

6.3.3 Ultraviolet spectroscopy

The Large aperture UV/Optical/IR (LUVOIR) is a concept, multiple-wavelength space observatory. The primary mirror would be from 8 up to 16 meters, made into several segments (Thronson *et al.*, 2016). The ultraviolet imaging and spectrograph are one of the key capabilities for this 21st century space telescope. With 10 times more collecting area then HST and far more sensitivity, this would be huge leap in order to study the kinematics of intergalactic gas through galactic feedback, made accessible through highly resolved quasar spectra (Dalcanton *et al.*, 2015).

6.3.4 Radiative transfer in hydrodynamical simulations

From a theoretical perspective, the modelling of the IGM at higher redshifts is quite challenging due to the interplay between the ionising sources and the intergalactic gas. The detailed radiative transfer is a daunting computational task due to high dimentionality of the problem and the range of scales that need to be resolved. In principle, one has to resolve the spatial scales from stars, or accreting black holes up to volumes which are representative of large ionised regions in the Universe (comoving megaparsec scales). A straight forward but expensive approach is to perform ray tracing for each source individually (Trac & Gnedin, 2011). An alternative less expensive method is momentum based radiative transfer (Rosdahl *et al.*, 2013). Despite the challenges, the simulations are already providing insight on the morphology of reionsation and ionising sources (Pawlik, Schaye & Vecchia, 2015; Ocvirk *et al.*, 2016). The cosmological simulations are paving the way for 21 cm observations by modelling the impact of quasars and galaxies on the IGM (Datta *et al.*, 2012; Iliev *et al.*, 2014). The simulations are also helping to understand the signature ionised regions formed around high redshift quasars during reionsation (Kakiichi *et al.*, 2017).

6.3.5 The ionising background at low redshifts

The UVB is well characterised at $z \gtrsim 1.6$ due to the availability of high resolution spectra from ground based telescopes (Haardt & Madau, 2001; Faucher-Giguère *et al.*, 2009; Haardt & Madau, 2012). At $z \lesssim 0.5$, the HST/COS provides the necessary

coverage to infer the UVB using the Lyα forest in quasar spectra (Kollmeier *et al.*, 2014; Shull *et al.*, 2015; Viel *et al.*, 2013b; Nasir *et al.*, 2017). However, due to lack of spectra at intermediate redshifts, the UVB is poorly constrained. Future, observations can therefore fill the gap in our understanding of the properties of the IGM and constraining the UVB at these redshifts. Once combined with current observations this can provide a more consistent picture of the evolution of the UVB.

6.3.6 Interplay between circumgalactic medium and IGM

Our understanding of the low redshift IGM is far from complete. The key challenge is to determine the exact mechanism for galactic feedback, pinpointing the contributions from AGN and supernovae and how they influence galaxy evolution and formation. The key measurements are statistics of H I , O VI and other metal absorbers, more specifically the CDDF, obtained from quasar spectra (Danforth *et al.*, 2016). As the high column density systems owe their existence to the dense gas residing in the vicinity of galaxies, this makes CDDF at high column density sensitive to any feedback processes, which potentially redistributes the gas and metals. The recent measurements from HST/COS spectra are already providing new insight into this complex interplay between circumgalactic and IGM gas (Werk *et al.*, 2014; Keeney *et al.*, 2017; Viel *et al.*, 2017a; Pratt *et al.*, 2017). The future space telescope, LUVOIR, with its groundbreaking UV spectroscopy capabilities would provide an huge leap in terms of pinpointing the role of various processes in this regard. The bright quasars at low redshift would provide the opportunity to obtain high resolution spectroscopy, in order to understand the gas dynamics in the CGM through galactic feedback (Dalcanton *et al.*, 2015).

6.3.7 Warm dark matter models

The warm dark matter model was introduced, to alleviate the problems in matter power spectrum at small scales around few Mpc or less. As the Lyα flux power spectrum measurements probe structure formation at these scales, they provide invaluable constraint on the warm dark matter (WDM) properties. The observations can provide constraints

on the models and potentially limits on the masses of WDM particles (e.g. Viel *et al.* (2013b); Iršič *et al.* (2017c,b)). Future improvements on the integrated thermal history measurements (see Chapter 5) and IGM temperature measurements would certainly enhance the constraining power of these models, as the IGM temperature is a key astrophysical systematic in these measurements.

6.3.8 Future Work

In the previous section, I have highlighted the key observational developments which help to further extend my current work. I have mentioned the recent surge to find high redshift quasars and how this will be further improved by new telescopes. The possibility to obtain spectra for these high redshift quasars would help to probe the ionisation state of high redshift IGM and possibly also constrain the integrated heating during reionsation. An increasing number of quasar sights-lines with better signal-to-noise would provide new and improved line-of-sight flux power spectrum measurements. This would significantly improve the constraints on the integrated thermal history of IGM obtained in Chapter 5. The effect on the flux power spectrum due to the bright and rarer sources relative contribution to UVB is incorporated in my method using parameter $f_{\rm qso}$. However, the parameter remain unconstrained in the current analysis as the data is limited to relatively larger scales with large errors bars (please see Figure 5.5 and 5.6 in Chapter 5). The future measurements, specifically reaching towards small scales will aid constrains on the relative contribution of high redshift quasars to UVB. This will help to distinguish between the galaxies and AGN driven reionsation scenarios.

The addition of high resolution quasar spectra at $z > 5.5$, would also help to further extend our models employing a varying mean free path, a fluctuating UVB and temperature fluctuations to explain the observations, such as opacity variations (Becker *et al.*, 2015). This would better establish the structure of patchy reionsation, with the aid of hydrodynamical simulations, that employ radiative transfer to better constrain the models during reionsation.

The intensity and shape of the UV background is the one of the key elements to model the diffuse IGM. One method of determining the UVB involves comparing the

H I column densities from quasar absorption lines with hydrodynamical simulations (see Chapter 2). As the intensity of the UVB is proportional to the normalisation of CDDF, where it can be altered by scaling the optical depths in post-processing within simulations. This in turn determines the UVB once compared with the CDDF from the observed quasar absorption lines. A possible extension to my work would be to do this analysis at redshifts where UVB is poorly constraint, at $z \lesssim 1.6$, thus inferring the intensity of UVB at lower redshifts.

I address the affects of supernovae and AGN feedback and its implications on the IGM properties using the Lyα forest in Chapter 2. The method used the Lyα CDDF and velocity width distribution, due to their sensitivity to such processes. I found that the feedback prescriptions used in our simulations had only a modest effect, and it is very little to alleviate the disagreement with the COS observations. The simulations used the energy-driven outflow model by Puchwein & Springel (2013), where the velocity of winds are proportional to the escape velocity of galaxy, chosen such that its able to reproduce the observed galaxy stellar mass function at the low mass end. The future work might explore the various versions of such a feedback model, which can eject the overdense gas in to the IGM. In addition, the publically available EAGLE (Schaye *et al.*, 2015) and ILLUSTRIS (Vogelsberger *et al.*, 2014a) simulations could be compared to data, as they have different feedback prescriptions. Potential detailed observations of gas flow in the galaxies made possible by UV spectroscopy in future, would prove very useful in detail modelling of such galactic feedback processes. In turn, the properties of the Lyα forest, in particular CDDF and velocity widths obtained from these set of simulations, using these feedback prescriptions, can be compared with observations by HST/COS, and in future with LUVIOR.

In conclusion, the future of the Lyα forest as a probe to study the IGM at cosmic time would be shaped by both state of the art cosmological simulations and potential future observations. The key questions for future work will be the process of reionsation at high redshifts and the impact of galactic feedback at low redshifts. The promised observations will provide a detailed picture of reionsation and an avenue to study various mechanisms for galactic feedback. Future simulations will be able to constrain the models of reionsation and pin-point the role of various processes in feedback. In short,

the future prospects of the field are quite optimistic.

Bibliography

Adams J. J., Uson J. M., Hill G. J., MacQueen P. J., 2011. ApJ, **728**, 107. *A New z = 0 Metagalactic Ultraviolet Background Limit*.

Altay G., Theuns T., Schaye J., Crighton N. H. M., Dalla Vecchia C., 2011. ApJ, **737**, L37. *Through Thick and Thin - HI Absorption in Cosmological Simulations*.

Aracil B., Tripp T. M., Bowen D. V., Prochaska J. X., Chen H.-W., Frye B. L., 2006. MNRAS, **367**, 139. *High-metallicity, photoionized gas in intergalactic large-scale filaments*.

Astier P., Guy J., Regnault N., Pain R., Aubourg E., Balam D., Basa S., Carlberg R. G., Fabbro S., Fouchez D., Hook I. M., Howell D. A., Lafoux H., Neill J. D., Palanque-Delabrouille N., Perrett K., Pritchet C. J., Rich J., Sullivan M., Taillet R., Aldering G., Antilogus P., Arsenijevic V., Balland C., Baumont S., Bronder J., Courtois H., Ellis R. S., Filiol M., Gonçalves A. C., Goobar A., Guide D., Hardin D., Lusset V., Lidman C., McMahon R., Mouchet M., Mourao A., Perlmutter S., Ripoche P., Tao C., Walton N., 2006. A&A, **447**, 31. *The Supernova Legacy Survey: measurement of Ω_M, Ω and w from the first year data set*.

Bañados E., Venemans B. P., Morganson E., Decarli R., Walter F., Chambers K. C., Rix H.-W., Farina E. P., Fan X., Jiang L., McGreer I., De Rosa G., Simcoe R., Weiß A., Price P. A., Morgan J. S., Burgett W. S., Greiner J., Kaiser N., Kudritzki R.-P., Magnier E. A., Metcalfe N., Stubbs C. W., Sweeney W., Tonry J. L., Wainscoat R. J., Waters C., 2014. AJ, **148**, 14. *Discovery of Eight $z \sim 6$ Quasars from Pan-STARRS1*.

Bañados E., Venemans B. P., Decarli R., Farina E. P., Mazzucchelli C., Walter F., Fan X., Stern D., Schlafly E., Chambers K. C., Rix H.-W., Jiang L., McGreer I., Simcoe

R., Wang F., Yang J., Morganson E., De Rosa G., Greiner J., Baloković M., Burgett W. S., Cooper T., Draper P. W., Flewelling H., Hodapp K. W., Jun H. D., Kaiser N., Kudritzki R.-P., Magnier E. A., Metcalfe N., Miller D., Schindler J.-T., Tonry J. L., Wainscoat R. J., Waters C., Yang Q., 2016. ApJS, **227**, 11. *The Pan-STARRS1 Distant* $z > 5.6$ *Quasar Survey: More than 100 Quasars within the First Gyr of the Universe*.

Bahcall J. N., Bergeron J., Boksenberg A., Hartig G. F., Jannuzi B. T., Kirhakos S., Sargent W. L. W., Savage B. D., Schneider D. P., Turnshek D. A., Weymann R. J., Wolfe A. M., 1993. ApJS, **87**, 1. *The Hubble Space Telescope quasar absorption line key project. I - First observational results, including Lyman-alpha and Lyman-limit systems*.

Becker G. D., Bolton J. S., 2013. MNRAS, **436**, 1023. *New measurements of the ionizing ultraviolet background over* $2 < z < 5$ *and implications for hydrogen reionization*.

Becker G. D., Bolton J. S., Lidz A., 2015. *PASA*, **32**, e045. *Reionisation and High-Redshift Galaxies: The View from Quasar Absorption Lines*.

Becker R. H., Fan X., White R. L., Strauss M. A., Narayanan V. K., Lupton R. H., Gunn J. E., Annis J., Bahcall N. A., Brinkmann J., Connolly A. J., Csabai I., Czarapata P. C., Doi M., Heckman T. M., Hennessy G. S., Ivezić Ž., Knapp G. R., Lamb D. Q., McKay T. A., Munn J. A., Nash T., Nichol R., Pier J. R., Richards G. T., Schneider D. P., Stoughton C., Szalay A. S., Thakar A. R., York D. G., 2001. AJ, **122**, 2850. *Evidence for Reionization at* $z \sim 6$*: Detection of a Gunn-Peterson Trough in a z=6.28 Quasar*.

Becker G. D., Bolton J. S., Haehnelt M. G., Sargent W. L. W., 2011. MNRAS, **410**, 1096. *Detection of extended He II reionization in the temperature evolution of the intergalactic medium*.

Becker G. D., Hewett P. C., Worseck G., Prochaska J. X., 2013. MNRAS, **430**, 2067. *A refined measurement of the mean transmitted flux in the Ly*α *forest over* $2 < z < 5$ *using composite quasar spectra*.

Becker G. D., Bolton J. S., Madau P., Pettini M., Ryan-Weber E. V., Venemans B. P., 2015. MNRAS, **447**, 3402. *Evidence of patchy hydrogen reionization from an extreme Lyα trough below redshift six*.

Bennett C. L., Larson D., Weiland J. L., Jarosik N., Hinshaw G., Odegard N., Smith K. M., Hill R. S., Gold B., Halpern M., Komatsu E., Nolta M. R., Page L., Spergel D. N., Wollack E., Dunkley J., Kogut A., Limon M., Meyer S. S., Tucker G. S., Wright E. L., 2013. ApJS, **208**, 20. *Nine-year Wilkinson Microwave Anisotropy Probe (WMAP) Observations: Final Maps and Results*.

Bi H. G., Boerner G., Chu Y., 1992. A&A, **266**, 1. *An alternative model for the Ly-alpha absorption forest*.

Boera E., Murphy M. T., Becker G. D., Bolton J. S., 2014. MNRAS, **441**, 1916. *The thermal history of the intergalactic medium down to redshift z = 1.5: a new curvature measurement*.

Boera E., Murphy M. T., Becker G. D., Bolton J. S., 2016. MNRAS, **456**, L79. *Constraining the temperature-density relation of the intergalactic medium with the Lyman α and β forests*.

Bolton J. S., Becker G. D., 2009. MNRAS, **398**, L26. *Resolving the high redshift Lyα forest in smoothed particle hydrodynamics simulations*.

Bolton J. S., Haehnelt M. G., 2007. MNRAS, **374**, 493. *The nature and evolution of the highly ionized near-zones in the absorption spectra of $z = 6$ quasars*.

Bolton J. S., Haehnelt M. G., Viel M., Springel V., 2005. MNRAS, **357**, 1178. *The Lyman α forest opacity and the metagalactic hydrogen ionization rate at $z \sim 2 - 4$*.

Bolton J. S., Viel M., Kim T.-S., Haehnelt M. G., Carswell R. F., 2008. MNRAS, **386**, 1131. *Possible evidence for an inverted temperature-density relation in the intergalactic medium from the flux distribution of the Lyα forest*.

Bolton J. S., Becker G. D., Raskutti S., Wyithe J. S. B., Haehnelt M. G., Sargent W. L. W., 2012. MNRAS, **419**, 2880. *Improved measurements of the intergalactic medium temperature around quasars: possible evidence for the initial stages of He II reionization at $z\sim6$*.

Bolton J. S., Becker G. D., Haehnelt M. G., Viel M., 2014. MNRAS, **438**, 2499. *A consistent determination of the temperature of the intergalactic medium at redshift* $z = 2.4$.

Bolton J. S., Puchwein E., Sijacki D., Haehnelt M. G., Kim T.-S., Meiksin A., Regan J. A., Viel M., 2017. MNRAS, **464**, 897. *The Sherwood simulation suite: overview and data comparisons with the Lyman* α *forest at redshifts* $2 < z < 5$.

Bouwens R. J., Illingworth G. D., Oesch P. A., Caruana J., Holwerda B., Smit R., Wilkins S., 2015. ApJ, **811**, 140. *Reionization After Planck: The Derived Growth of the Cosmic Ionizing Emissivity Now Matches the Growth of the Galaxy UV Luminosity Density*.

Calura F., Tescari E., D'Odorico V., Viel M., Cristiani S., Kim T.-S., Bolton J. S., 2012. MNRAS, **422**, 3019. *The Lyman* α *forest flux probability distribution at z>3*.

Carswell R. F., Webb J. K., 2014. *VPFIT: Voigt profile fitting program*, Astrophysics Source Code Library.

Cen R., Ostriker J. P., 1999. ApJ, **514**, 1. *Where Are the Baryons?*

Cen R., Ostriker J. P., 2006. ApJ, **650**, 560. *Where Are the Baryons? II. Feedback Effects*.

Cen R., Miralda-Escudé J., Ostriker J. P., Rauch M., 1994. ApJ, **437**, L9. *Gravitational collapse of small-scale structure as the origin of the Lyman-alpha forest*.

Cen R., McDonald P., Trac H., Loeb A., 2009. ApJ, **706**, L164. *Probing the Epoch of Reionization with the Ly*α *Forest at* $z \sim 4 - 5$.

Chardin J., Haehnelt M. G., Aubert D., Puchwein E., 2015. MNRAS, **453**, 2943. *Calibrating cosmological radiative transfer simulations with Ly* α *forest data: evidence for large spatial UV background fluctuations at z* $\sim$ *5.6-5.8 due to rare bright sources*.

Chardin J., Puchwein E., Haehnelt M. G., 2017. MNRAS, **465**, 3429. *Large-scale opacity fluctuations in the Ly*α *forest: evidence for QSOs dominating the ionizing UV background at z 5.5-6?*

Compostella M., Cantalupo S., Porciani C., 2014. MNRAS, **445**, 4186. *AGN-driven helium reionization and the incidence of extended He III regions at redshift $z > 3$.*

Crain R. A., Theuns T., Dalla Vecchia C., Eke V. R., Frenk C. S., Jenkins A., Kay S. T., Peacock J. A., Pearce F. R., Schaye J., Springel V., Thomas P. A., White S. D. M., Wiersma R. P. C., 2009. MNRAS, **399**, 1773. *Galaxies-intergalactic medium interaction calculation - I. Galaxy formation as a function of large-scale environment.*

Croft R. A. C., Weinberg D. H., Katz N., Hernquist L., 1998. ApJ, **495**, 44. *Recovery of the Power Spectrum of Mass Fluctuations from Observations of the Lyα Forest.*

Croft R. A. C., Weinberg D. H., Bolte M., Burles S., Hernquist L., Katz N., Kirkman D., Tytler D., 2002. ApJ, **581**, 20. *Toward a Precise Measurement of Matter Clustering: Lyα Forest Data at Redshifts 2-4.*

Croft R. A. C., 2004. ApJ, **610**, 642. *Ionizing Radiation Fluctuations and Large-Scale Structure in the Lyα Forest.*

D' Aloisio A., McQuinn M., Trac H., 2015. ApJ, **813**, L38. *Large Opacity Variations in the High-redshift Lyα Forest: The Signature of Relic Temperature Fluctuations from Patchy Reionization.*

Dalcanton J., Seager S., Aigrain S., Battel S., Brandt N., Conroy C., Feinberg L., Gezari S., Guyon O., Harris W., Hirata C., Mather J., Postman M., Redding D., Schiminovich D., Stahl H. P., Tumlinson J., 2015. *ArXiv e-prints*. *From Cosmic Birth to Living Earths: The Future of UVOIR Space Astronomy*.

D'Aloisio A., Upton Sanderbeck P. R., McQuinn M., Trac H., Shapiro P. R., 2017. MNRAS, **468**, 4691. *On the contribution of active galactic nuclei to the high-redshift metagalactic ionizing background.*

Danforth C. W., Keeney B. A., Tilton E. M., Shull J. M., Stocke J. T., Stevans M., Pieri M. M., Savage B. D., France K., Syphers D., Smith B. D., Green J. C., Froning C., Penton S. V., Osterman S. N., 2016. ApJ, **817**, 111. *An HST/COS Survey of the Low-redshift Intergalactic Medium. I. Survey, Methodology, and Overall Results.*

Datta K. K., Mellema G., Mao Y., Iliev I. T., Shapiro P. R., Ahn K., 2012. MNRAS, **424**, 1877. *Light-cone effect on the reionization 21-cm power spectrum*.

Davé R., Hernquist L., Weinberg D. H., Katz N., 1997. ApJ, **477**, 21. *Voigt-Profile Analysis of the Lyα Forest in a Cold Dark Matter Universe*.

Davé R., Hernquist L., Katz N., Weinberg D. H., 1999. ApJ, **511**, 521. *The Low-Redshift Lyα Forest in Cold Dark Matter Cosmologies*.

Davé R., Cen R., Ostriker J. P., Bryan G. L., Hernquist L., Katz N., Weinberg D. H., Norman M. L., O'Shea B., 2001. ApJ, **552**, 473. *Baryons in the Warm-Hot Intergalactic Medium*.

Davé R., Oppenheimer B. D., Katz N., Kollmeier J. A., Weinberg D. H., 2010. MNRAS, **408**, 2051. *The intergalactic medium over the last 10 billion years - I. Lyα absorption and physical conditions*.

Davies F. B., Furlanetto S. R., 2015. *ArXiv e-prints*. *Large fluctuations in the hydrogen-ionizing background and mean free path following the epoch of reionization*.

Desjacques V., Nusser A., Haehnelt M. G., Stoehr F., 2004. MNRAS, **350**, 879. *Galactic winds and the Lyα forest*.

Dijkstra M., Lidz A., Hui L., 2004. ApJ, **605**, 7. *Beyond Lyα: Constraints and Consistency Tests from the Lyβ Forest*.

Eisenstein D. J., Hu W., 1999. ApJ, **511**, 5. *Power Spectra for Cold Dark Matter and Its Variants*.

Fan X., White R. L., Davis M., Becker R. H., Strauss M. A., Haiman Z., Schneider D. P., Gregg M. D., Gunn J. E., Knapp G. R., Lupton R. H., Anderson, Jr. J. E., Anderson S. F., Annis J., Bahcall N. A., Boroski W. N., Brunner R. J., Chen B., Connolly A. J., Csabai I., Doi M., Fukugita M., Hennessy G. S., Hindsley R. B., Ichikawa T., Ivezić Ž., Loveday J., Meiksin A., McKay T. A., Munn J. A., Newberg H. J., Nichol R., Okamura S., Pier J. R., Sekiguchi M., Shimasaku K., Stoughton C., Szalay A. S., Szokoly G. P., Thakar A. R., Vogeley M. S., York D. G., 2000. AJ,

120, 1167. *The Discovery of a Luminous Z=5.80 Quasar from the Sloan Digital Sky Survey*.

Fan X., Strauss M. A., Becker R. H., White R. L., Gunn J. E., Knapp G. R., Richards G. T., Schneider D. P., Brinkmann J., Fukugita M., 2006a. AJ, **132**, 117. *Constraining the Evolution of the Ionizing Background and the Epoch of Reionization with $z \sim 6$ Quasars. II. A Sample of 19 Quasars*.

Fan X., Strauss M. A., Becker R. H., White R. L., Gunn J. E., Knapp G. R., Richards G. T., Schneider D. P., Brinkmann J., Fukugita M., 2006b. AJ, **132**, 117. *Constraining the Evolution of the Ionizing Background and the Epoch of Reionization with $z \sim 6$ Quasars. II. A Sample of 19 Quasars*.

Faucher-Giguère C.-A., Prochaska J. X., Lidz A., Hernquist L., Zaldarriaga M., 2008. ApJ, **681**, 831. *A Direct Precision Measurement of the Intergalactic Lyα Opacity at $2 \leq z \leq 4.2$*.

Faucher-Giguère C., Lidz A., Zaldarriaga M., Hernquist L., 2009. ApJ, **703**, 1416. *A New Calculation of the Ionizing Background Spectrum and the Effects of He II Reionization*.

Finlator K., Oh S. P., Özel F., Davé R., 2012. MNRAS, **427**, 2464. *Gas clumping in self-consistent reionization models*.

Fixsen D. J., 2009. ApJ, **707**, 916. *The Temperature of the Cosmic Microwave Background*.

Frank S., Rasera Y., Vibert D., Milliard B., Popping A., Blaizot J., Courty S., Deharveng J.-M., Péroux C., Teyssier R., Martin C. D., 2012. MNRAS, **420**, 1731. *Observable signatures of the low-z circumgalactic and intergalactic media: ultraviolet line emission in simulations*.

Fumagalli M., Haardt F., Theuns T., Morris S. L., Cantalupo S., Madau P., Fossati M., 2017. MNRAS, **467**, 4802. *A measurement of the z = 0 UV background from Hα fluorescence*.

Furlanetto S. R., Oh S. P., 2005. MNRAS, **363**, 1031. *Taxing the rich: recombinations and bubble growth during reionization*.

Furlanetto S. R., Oh S. P., 2009. ApJ, **701**, 94. *The Temperature-Density Relation of the Intergalactic Medium after Hydrogen Reionization*.

Furlanetto S. R., McQuinn M., Hernquist L., 2006. MNRAS, **365**, 115. *Characteristic scales during reionization*.

Furlanetto S. R., Zaldarriaga M., Hernquist L., 2004. ApJ, **613**, 1. *The Growth of H II Regions During Reionization*.

Gaikwad P., Khaire V., Choudhury T. R., Srianand R., 2017a. MNRAS, **466**, 838. *Intergalactic Lyman continuum photon budget in the past 5 billion years*.

Gaikwad P., Srianand R., Choudhury T. R., Khaire V., 2017b. MNRAS, **467**, 3172. *VoIgt profile Parameter Estimation Routine (viper): H I photoionization rate at $z < 0.5$*.

Garzilli A., Bolton J. S., Kim T.-S., Leach S., Viel M., 2012. MNRAS, **424**, 1723. *The intergalactic medium thermal history at redshift z = 1.7-3.2 from the Lyα forest: a comparison of measurements using wavelets and the flux distribution*.

Garzilli A., Theuns T., Schaye J., 2015. MNRAS, **450**, 1465. *The broadening of Lyman-α forest absorption lines*.

Giallongo E., Menci N., Fiore F., Castellano M., Fontana A., Grazian A., Pentericci L., 2012. ApJ, **755**, 124. *Active Galactic Nuclei as Main Contributors to the Ultraviolet Ionizing Emissivity at High Redshifts: Predictions from a Λ-CDM Model with Linked AGN/Galaxy Evolution*.

Gnedin N. Y., Hui L., 1998. MNRAS, **296**, 44. *Probing the Universe with the Lyalpha forest - I. Hydrodynamics of the low-density intergalactic medium*.

Gnedin N. Y., Kravtsov A. V., Chen H.-W., 2008. ApJ, **672**, 765. *Escape of Ionizing Radiation from High-Redshift Galaxies*.

Gnedin N. Y., 2014. ApJ, **793**, 29. *Cosmic Reionization on Computers. I. Design and Calibration of Simulations*.

Green J. C., Froning C. S., Osterman S., Ebbets D., Heap S. H., Leitherer C., Linsky J. L., Savage B. D., Sembach K., Shull J. M., Siegmund O. H. W., Snow T. P., Spencer J., Stern S. A., Stocke J., Welsh B., Béland S., Burgh E. B., Danforth C., France K., Keeney B., McPhate J., Penton S. V., Andrews J., Brownsberger K., Morse J., Wilkinson E., 2012. ApJ, **744**, 60. *The Cosmic Origins Spectrograph*.

Greig B., Bolton J. S., Wyithe J. S. B., 2015. MNRAS, **447**, 2503. *The impact of temperature fluctuations on the large-scale clustering of the Lyα forest*.

Gunn J. E., Peterson B. A., 1965. ApJ, **142**, 1633. *On the Density of Neutral Hydrogen in Intergalactic Space.*

Gurvich A., Burkhart B., Bird S., 2017. ApJ, **835**, 175. *The Effect of AGN Heating on the Low-redshift Lyα Forest*.

Guth A. H., 1981. Phys. Rev. D, **23**, 347. *Inflationary universe: A possible solution to the horizon and flatness problems*.

Haardt F., Madau P., 2001. *Modelling the UV/X-ray cosmic background with CUBA*, In: *Clusters of Galaxies and the High Redshift Universe Observed in X-rays, Neumann, D. M. & Tran, J. T. V. ed., astro-ph/0106018*.

Haardt F., Madau P., 2012. ApJ, **746**, 125. *Radiative Transfer in a Clumpy Universe. IV. New Synthesis Models of the Cosmic UV/X-Ray Background*.

Haehnelt M. G., Steinmetz M., 1998. MNRAS, **298**, L21. *Probing the thermal history of the intergalactic medium with Lyalpha absorption lines*.

Hassan S., Davé R., Mitra S., Finlator K., Ciardi B., Santos M. G., 2017. *ArXiv e-prints*. *Constraining the contribution of active galactic nuclei to reionisation*.

Hernquist L., Katz N., Weinberg D. H., Miralda-Escudé J., 1996. ApJ, **457**, L51. *The Lyman-Alpha Forest in the Cold Dark Matter Model*.

Hopkins P. F., Richards G. T., Hernquist L., 2007. ApJ, **654**, 731. *An Observational Determination of the Bolometric Quasar Luminosity Function*.

Hu E. M., Kim T.-S., Cowie L. L., Songaila A., Rauch M., 1995. AJ, **110**, 1526. *The Distribution of Column Densities and B Values in the Lyman-Alpha Forest*.

Hui L., Gnedin N. Y., 1997. MNRAS, **292**, 27. *Equation of state of the photoionized intergalactic medium*.

Hui L., Haiman Z., 2003. ApJ, **596**, 9. *The Thermal Memory of Reionization History*.

Hui L., Rutledge R. E., 1999. ApJ, **517**, 541. *The b Distribution and the Velocity Structure of Absorption Peaks in the Lyα Forest*.

Hui L., Gnedin N. Y., Zhang Y., 1997. ApJ, **486**, 599. *The Statistics of Density Peaks and the Column Density Distribution of the Lyα Forest*.

Iapichino L., Viel M., Borgani S., 2013. MNRAS, **432**, 2529. *Turbulence driven by structure formation in the circumgalactic medium*.

Iliev I. T., Mellema G., Ahn K., Shapiro P. R., Mao Y., Pen U.-L., 2014. MNRAS, **439**, 725. *Simulating cosmic reionization: how large a volume is large enough?*

Iršič V., Viel M., 2014. *JCAP*, **12**, 024. *The Lyman β forest as a cosmic thermometer*.

Iršič V., Viel M., Berg T. A. M., D'Odorico V., Haehnelt M. G., Cristiani S., Cupani G., Kim T.-S., López S., Ellison S., Becker G. D., Christensen L., Denney K. D., Worseck G., Bolton J. S., 2017a. MNRAS, **466**, 4332. *The Lyman α forest power spectrum from the XQ-100 Legacy Survey*.

Iršič V., Viel M., Haehnelt M. G., Bolton J. S., Becker G. D., 2017b. *ArXiv e-prints*. *First constraints on fuzzy dark matter from Lyman-α forest data and hydrodynamical simulations*.

Iršič V., Viel M., Haehnelt M. G., Bolton J. S., Cristiani S., Becker G. D., D'Odorico V., Cupani G., Kim T.-S., Berg T. A. M., López S., Ellison S., Christensen L., Denney K. D., Worseck G., 2017c. Phys. Rev. D, **96(2)**, 023522. *New constraints on the free-streaming of warm dark matter from intermediate and small scale Lyman-α forest data*.

Janknecht E., Reimers D., Lopez S., Tytler D., 2006. A&A, **458**, 427. *The evolution of Lyman α absorbers in the redshift range* $0.5 < z < 1.9$.

Jiang L., McGreer I. D., Fan X., Bian F., Cai Z., Clément B., Wang R., Fan Z., 2015. AJ, **149**, 188. *Discovery of Eight $z \sim 6$ Quasars in the Sloan Digital Sky Survey Overlap Regions*.

Johnson A., Blake C., Koda J., Ma Y.-Z., Colless M., Crocce M., Davis T. M., Jones H., Magoulas C., Lucey J. R., Mould J., Scrimgeour M. I., Springob C. M., 2014. MNRAS, **444**, 3926. *The 6dF Galaxy Survey: cosmological constraints from the velocity power spectrum*.

Kakiichi K., Graziani L., Ciardi B., Meiksin A., Compostella M., Eide M. B., Zaroubi S., 2017. MNRAS, **468**, 3718. *The concerted impact of galaxies and QSOs on the ionization and thermal state of the intergalactic medium*.

Katz N., Weinberg D. H., Hernquist L., 1996. ApJS, **105**, 19. *Cosmological Simulations with TreeSPH*.

Keeney B. A., Stocke J. T., Danforth C. W., Shull J. M., Pratt C. T., Froning C. S., Green J. C., Penton S. V., Savage B. D., 2017. ApJS, **230**, 6. *Characterizing the Circumgalactic Medium of Nearby Galaxies with HST/COS and HST/STIS Absorption-line Spectroscopy. II. Methods and Models*.

Khaire V., Srianand R., 2015. MNRAS, **451**, L30. *Photon underproduction crisis: Are QSOs sufficient to resolve it?*

Khaire V., Srianand R., Choudhury T. R., Gaikwad P., 2016. MNRAS, **457**, 4051. *The redshift evolution of escape fraction of hydrogen ionizing photons from galaxies*.

Kim T.-S., Cristiani S., D'Odorico S., 2001. A&A, **373**, 757. *The Lyalpha forest at $1.5 < z < 4$*.

Kim T.-S., Hu E. M., Cowie L. L., Songaila A., 1997. AJ, **114**, 1. *The Redshift Evolution of the Ly alpha Forest*.

Kim T.-S., Bolton J. S., Viel M., Haehnelt M. G., Carswell R. F., 2007. MNRAS, **382**, 1657. *An improved measurement of the flux distribution of the Lyα forest in QSO absorption spectra: the effect of continuum fitting, metal contamination and noise properties*.

Kim T.-S., Partl A. M., Carswell R. F., Müller V., 2013. A&A, **552**, A77. *The evolution of H I and C IV quasar absorption line systems at* $1.9 < z < 3.2$.

Kirkman D., Tytler D., 1997. ApJ, **484**, 672. *Intrinsic Properties of the* $z \geq 2.7$ *Ly*α *Forest from Keck Spectra of Quasar HS 1946+7658*.

Kirkman D., Tytler D., Lubin D., Charlton J., 2007. MNRAS, **376**, 1227. *Continuous statistics of the Ly*α *forest at* $0 < z < 1.6$*: the mean flux, flux distribution and autocorrelation from HST FOS spectra*.

Kollmeier J. A., Weinberg D. H., Oppenheimer B. D., Haardt F., Katz N., Davé R., Fardal M., Madau P., Danforth C., Ford A. B., Peeples M. S., McEwen J., 2014. ApJ, **789**, L32. *The Photon Underproduction Crisis*.

Kulkarni G., Hennawi J. F., Oñorbe J., Rorai A., Springel V., 2015. ApJ, **812**, 30. *Characterizing the Pressure Smoothing Scale of the Intergalactic Medium*.

Kulkarni G., Choudhury T. R., Puchwein E., Haehnelt M. G., 2017. MNRAS, **469**, 4283. *Large 21-cm signals from AGN-dominated reionization*.

Lai K., Lidz A., Hernquist L., Zaldarriaga M., 2006. ApJ, **644**, 61. *The Impact of Temperature Fluctuations on the Ly*α *Forest Power Spectrum*.

Lee K.-G., Hennawi J. F., Spergel D. N., Weinberg D. H., Hogg D. W., Viel M., Bolton J. S., Bailey S., Pieri M. M., Carithers W., Schlegel D. J., Lundgren B., Palanque-Delabrouille N., Suzuki N., Schneider D. P., Yèche C., 2015. ApJ, **799**, 196. *IGM Constraints from the SDSS-III/BOSS DR9 Ly*α *Forest Transmission Probability Distribution Function*.

Lee K.-G., 2012. ApJ, **753**, 136. *Systematic Continuum Errors in the Ly*α *Forest and the Measured Temperature-Density Relation*.

Lehner N., Savage B. D., Richter P., Sembach K. R., Tripp T. M., Wakker B. P., 2007. ApJ, **658**, 680. *Physical Properties, Baryon Content, and Evolution of the Ly*α *Forest: New Insights from High-Resolution Observations at* $z < 0.4$.

Lehner N., Savage B. D., Richter P., Sembach K. R., Tripp T. M., Wakker B. P., 2008. ApJ, **674**, 613. *Erratum: "Physical Properties, Baryon Content, and Evolution of the*

Lyα Forest: New Insights from High-Resolution Observations at z lesssim 0.4" (ApJ, 658, 680 [2007]).

Lewis A., Challinor A., Lasenby A., 2000. ApJ, **538**, 473. *Efficient Computation of Cosmic Microwave Background Anisotropies in Closed Friedmann-Robertson-Walker Models*.

Lidz A., Malloy M., 2014. ApJ, **788**, 175. *On Modeling and Measuring the Temperature of the $z \sim$5 Intergalactic Medium*.

Lidz A., Heitmann K., Hui L., Habib S., Rauch M., Sargent W. L. W., 2006. ApJ, **638**, 27. *Tightening Constraints from the Lyα Forest with the Flux Probability Distribution Function*.

Lidz A., Faucher-Giguère C.-A., Dall'Aglio A., McQuinn M., Fechner C., Zaldarriaga M., Hernquist L., Dutta S., 2010. ApJ, **718**, 199. *A Measurement of Small-scale Structure in the $2.2 \leq z \leq 4.2$ Lyα Forest*.

Lidz A., 2016. *Understanding the Epoch of Cosmic Reionization: Challenges and Progress*, **423**, 23. *Physics of the Intergalactic Medium During the Epoch of Reionization*.

Liu A., Parsons A. R., 2016. MNRAS, **457**, 1864. *Constraining cosmology and ionization history with combined 21 cm power spectrum and global signal measurements*.

Lu L., Sargent W. L. W., Womble D. S., Takada-Hidai M., 1996. ApJ, **472**, 509. *The Lyman-Alpha Forest at Z approximately 4: Keck HIRES Observations of Q0000-26*.

Lukić Z., Stark C. W., Nugent P., White M., Meiksin A. A., Almgren A., 2015. MNRAS, **446**, 3697. *The Lyman α forest in optically thin hydrodynamical simulations*.

Lusso E., Decarli R., Dotti M., Montuori C., Hogg D. W., Tsalmantza P., Fumagalli M., Prochaska J. X., 2014. MNRAS, **441**, 316. *The nature of massive black hole binary candidates - II. Spectral energy distribution atlas*.

Lynden-Bell D., 1969. Nature, **223**, 690. *Galactic Nuclei as Collapsed Old Quasars*.

Ma X., Kasen D., Hopkins P. F., Faucher-Giguère C.-A., Quataert E., Kereš D., Murray N., 2015. MNRAS, **453**, 960. *The difficulty of getting high escape fractions of ionizing photons from high-redshift galaxies: a view from the FIRE cosmological simulations*.

Madau P., Haardt F., 2015. ApJ, **813**, L8. *Cosmic Reionization after Planck: Could Quasars Do It All?*

Madau P., Haardt F., Rees M. J., 1999. ApJ, **514**, 648. *Radiative Transfer in a Clumpy Universe. III. The Nature of Cosmological Ionizing Sources*.

Maiolino R., Haehnelt M., Murphy M. T., Queloz D., Origlia L., Alcala J., Alibert Y., Amado P. J., Allende Prieto C., Ammler-von Eiff M., Asplund M., Barstow M., Becker G., Bonfils X., Bouchy F., Bragaglia A., Burleigh M. R., Chiavassa A., Cimatti D. A., Cirasuolo M., Cristiani S., D'Odorico V., Dravins D., Emsellem E., Farihi J., Figueira P., Fynbo J., Gansicke B. T., Gillon M., Gustafsson B., Hill V., Israelyan G., Korn A., Larsen S., De Laverny P., Liske J., Lovis C., Marconi A., Martins C., Molaro P., Nisini B., Oliva E., Petitjean P., Pettini M., Recio Blanco A., Rebolo R., Reiners A., Rodriguez-Lopez C., Ryde N., Santos N. C., Savaglio S., Snellen I., Strassmeier K., Tanvir N., Testi L., Tolstoy E., Triaud A., Vanzi L., Viel M., Volonteri M., 2013. *ArXiv e-prints*. *A Community Science Case for E-ELT HIRES*.

Matsuoka Y., Onoue M., Kashikawa N., Iwasawa K., Strauss M. A., Nagao T., Imanishi M., Niida M., Toba Y., Akiyama M., Asami N., Bosch J., Foucaud S., Furusawa H., Goto T., Gunn J. E., Harikane Y., Ikeda H., Kawaguchi T., Kikuta S., Komiyama Y., Lupton R. H., Minezaki T., Miyazaki S., Morokuma T., Murayama H., Nishizawa A. J., Ono Y., Ouchi M., Price P. A., Sameshima H., Silverman J. D., Sugiyama N., Tait P. J., Takada M., Takata T., Tanaka M., Tang J.-J., Utsumi Y., 2016. ApJ, **828**, 26. *Subaru High-z Exploration of Low-luminosity Quasars (SHELLQs). I. Discovery of 15 Quasars and Bright Galaxies at 5.7* $< z <$ 6.9.

McDonald P., Miralda-Escudé J., Rauch M., Sargent W. L. W., Barlow T. A., Cen R., Ostriker J. P., 2000. ApJ, **543**, 1. *The Observed Probability Distribution Function, Power Spectrum, and Correlation Function of the Transmitted Flux in the Ly*α *Forest*.

McDonald P., Miralda-Escudé J., Rauch M., Sargent W. L. W., Barlow T. A., Cen R., 2001. ApJ, **562**, 52. *A Measurement of the Temperature-Density Relation in the Intergalactic Medium Using a New Lyα Absorption-Line Fitting Method*.

McDonald P., Seljak U., Cen R., Bode P., Ostriker J. P., 2005. MNRAS, **360**, 1471. *Physical effects on the Lyα forest flux power spectrum: damping wings, ionizing radiation fluctuations and galactic winds*.

McDonald P., Seljak U., Burles S., Schlegel D. J., Weinberg D. H., Cen R., Shih D., Schaye J., Schneider D. P., Bahcall N. A., Briggs J. W., Brinkmann J., Brunner R. J., Fukugita M., Gunn J. E., Ivezić Ž., Kent S., Lupton R. H., Vanden Berk D. E., 2006. ApJS, **163**, 80. *The Lyα Forest Power Spectrum from the Sloan Digital Sky Survey*.

McQuinn M., Upton Sanderbeck P. R., 2016. MNRAS, **456**, 47. *On the intergalactic temperature-density relation*.

McQuinn M., Lidz A., Zaldarriaga M., Hernquist L., Hopkins P. F., Dutta S., Faucher-Giguère C.-A., 2009. ApJ, **694**, 842. *He II Reionization and its Effect on the Intergalactic Medium*.

McQuinn M., Hernquist L., Lidz A., Zaldarriaga M., 2011. MNRAS, **415**, 977. *The signatures of large-scale temperature and intensity fluctuations in the Lyman α forest*.

McQuinn M., 2016. ARA&A, **54**, 313. *The Evolution of the Intergalactic Medium*.

Meiksin A., Bolton J. S., Tittley E. R., 2015. MNRAS, **453**, 899. *Gas around galaxy haloes - II. Hydrogen absorption signatures from the environments of galaxies at redshifts* $2 < z < 3$.

Meiksin A., Bryan G., Machacek M., 2001. MNRAS, **327**, 296. *Hydrodynamical simulations of the Lyα forest: data comparisons*.

Meiksin A., 2000. MNRAS, **314**, 566. *Spectral analysis of the Lyα forest using wavelets*.

Meiksin A. A., 2009. *Reviews of Modern Physics*, **81**, 1405. *The physics of the intergalactic medium*.

Miralda-Escudé J., Rees M. J., 1994. MNRAS, **266**, 343. *Reionization and thermal evolution of a photoionized intergalactic medium.*

Miralda-Escudé J., Cen R., Ostriker J. P., Rauch M., 1996. ApJ, **471**, 582. *The Ly alpha Forest from Gravitational Collapse in the Cold Dark Matter + Lambda Model*.

Mitra S., Choudhury T. R., Ferrara A., 2015. MNRAS, **454**, L76. *Cosmic reionization after Planck.*

Mortlock D. J., Warren S. J., Venemans B. P., Patel M., Hewett P. C., McMahon R. G., Simpson C., Theuns T., Gonzáles-Solares E. A., Adamson A., Dye S., Hambly N. C., Hirst P., Irwin M. J., Kuiper E., Lawrence A., Röttgering H. J. A., 2011. Nature, **474**, 616. *A luminous quasar at a redshift of z = 7.085*.

Mortlock D., 2016. *Understanding the Epoch of Cosmic Reionization: Challenges and Progress*, **423**, 187. *Quasars as Probes of Cosmological Reionization*.

Nasir F., Bolton J. S., Becker G. D., 2016. MNRAS, **463**, 2335. *Inferring the IGM thermal history during reionization with the Lyman α forest power spectrum at redshift z 5*.

Nasir F., Bolton J. S., Viel M., Kim T.-S., Haehnelt M. G., Puchwein E., Sijacki D., 2017. MNRAS, **471**, 1056. *The effect of stellar and AGN feedback on the low-redshift Lyman α forest in the Sherwood simulation suite*.

Norman M. L., Reynolds D. R., So G. C., Harkness R. P., Wise J. H., 2015. ApJS, **216**, 16. *Fully Coupled Simulation of Cosmic Reionization. I. Numerical Methods and Tests*.

Oñorbe J., Hennawi J. F., Lukić Z., Walther M., 2017. *ArXiv e-prints. Constraining Reionization with the z 5 $-$ 6 Lyman-α Forest Power Spectrum: the Outlook after Planck.*

Oñorbe J., Hennawi J. F., Lukić Z., 2017. ApJ, **837**, 106. *Self-consistent Modeling of Reionization in Cosmological Hydrodynamical Simulations*.

Ocvirk P., Gillet N., Shapiro P. R., Aubert D., Iliev I. T., Teyssier R., Yepes G., Choi J.-H., Sullivan D., Knebe A., Gottlöber S., D'Aloisio A., Park H., Hoffman Y.,

Stranex T., 2016. MNRAS, **463**, 1462. *Cosmic Dawn (CoDa): the First Radiation-Hydrodynamics Simulation of Reionization and Galaxy Formation in the Local Universe*.

Olive K. A., Skillman E. D., 2004. ApJ, **617**, 29. *A Realistic Determination of the Error on the Primordial Helium Abundance: Steps toward Nonparametric Nebular Helium Abundances*.

Oppenheimer B. D., Davé R., 2009. MNRAS, **395**, 1875. *The nature and origin of low-redshift OVI absorbers*.

Oppenheimer B. D., Davé R., Kereš D., Fardal M., Katz N., Kollmeier J. A., Weinberg D. H., 2010. MNRAS, **406**, 2325. *Feedback and recycled wind accretion: assembling the z = 0 galaxy mass function*.

Pachat S., Narayanan A., Muzahid S., Khaire V., Srianand R., Wakker B. P., Savage B. D., 2016. MNRAS, **458**, 733. *A pair of O VI and broad Ly α absorbers probing warm gas in a galaxy group environment at z $\sim$ 0.4*.

Paciga G., Albert J. G., Bandura K., Chang T.-C., Gupta Y., Hirata C., Odegova J., Pen U.-L., Peterson J. B., Roy J., Shaw J. R., Sigurdson K., Voytek T., 2013. MNRAS, **433**, 639. *A simulation-calibrated limit on the H I power spectrum from the GMRT Epoch of Reionization experiment*.

Palanque-Delabrouille N., Yèche C., Borde A., Le Goff J.-M., Rossi G., Viel M., Aubourg É., Bailey S., Bautista J., Blomqvist M., Bolton A., Bolton J. S., Busca N. G., Carithers B., Croft R. A. C., Dawson K. S., Delubac T., Font-Ribera A., Ho S., Kirkby D., Lee K.-G., Margala D., Miralda-Escudé J., Muna D., Myers A. D., Noterdaeme P., Pâris I., Petitjean P., Pieri M. M., Rich J., Rollinde E., Ross N. P., Schlegel D. J., Schneider D. P., Slosar A., Weinberg D. H., 2013. A&A, **559**, A85. *The one-dimensional Lyα forest power spectrum from BOSS*.

Palanque-Delabrouille N., Yèche C., Baur J., Magneville C., Rossi G., Lesgourgues J., Borde A., Burtin E., LeGoff J.-M., Rich J., Viel M., Weinberg D., 2015. *JCAP*, **11**, 011. *Neutrino masses and cosmology with Lyman-alpha forest power spectrum*.

Park H., Shapiro P. R., Choi J.-h., Yoshida N., Hirano S., Ahn K., 2016. *ArXiv e-prints*. *The Hydrodynamic Feedback of Cosmic Reionization on Small-Scale Structures and Its Impact on Photon Consumption during the Epoch of Reionization*.

Parsons A. R., Liu A., Aguirre J. E., Ali Z. S., Bradley R. F., Carilli C. L., DeBoer D. R., Dexter M. R., Gugliucci N. E., Jacobs D. C., Klima P., MacMahon D. H. E., Manley J. R., Moore D. F., Pober J. C., Stefan I. I., Walbrugh W. P., 2014. ApJ, **788**, 106. *New Limits on 21 cm Epoch of Reionization from PAPER-32 Consistent with an X-Ray Heated Intergalactic Medium at z = 7.7*.

Paschos P., Jena T., Tytler D., Kirkman D., Norman M. L., 2009. MNRAS, **399**, 1934. *The Lyα forest at redshifts 0.1-1.6: good agreement between a large hydrodynamic simulation and HST spectra*.

Patil A. H., Yatawatta S., Koopmans L. V. E., de Bruyn A. G., Brentjens M. A., Zaroubi S., Asad K. M. B., Hatef M., Jelić V., Mevius M., Offringa A. R., Pandey V. N., Vedantham H., Abdalla F. B., Brouw W. N., Chapman E., Ciardi B., Gehlot B. K., Ghosh A., Harker G., Iliev I. T., Kakiichi K., Majumdar S., Mellema G., Silva M. B., Schaye J., Vrbanec D., Wijnholds S. J., 2017. ApJ, **838**, 65. *Upper Limits on the 21 cm Epoch of Reionization Power Spectrum from One Night with LOFAR*.

Pawlik A. H., Schaye J., van Scherpenzeel E., 2009. MNRAS, **394**, 1812. *Keeping the Universe ionized: photoheating and the clumping factor of the high-redshift intergalactic medium*.

Pawlik A. H., Schaye J., Vecchia C. D., 2015. MNRAS, **451**, 1586. *Spatially adaptive radiation-hydrodynamical simulations of galaxy formation during cosmological reionization*.

Peeples M. S., Weinberg D. H., Davé R., Fardal M. A., Katz N., 2010. MNRAS, **404**, 1281. *Pressure support versus thermal broadening in the Lyman α forest - I. Effects of the equation of state on longitudinal structure*.

Perlmutter S., Aldering G., Goldhaber G., Knop R. A., Nugent P., Castro P. G., Deustua S., Fabbro S., Goobar A., Groom D. E., Hook I. M., Kim A. G., Kim M. Y., Lee J. C., Nunes N. J., Pain R., Pennypacker C. R., Quimby R., Lidman C., Ellis

R. S., Irwin M., McMahon R. G., Ruiz-Lapuente P., Walton N., Schaefer B., Boyle B. J., Filippenko A. V., Matheson T., Fruchter A. S., Panagia N., Newberg H. J. M., Couch W. J., Project T. S. C., 1999. ApJ, **517**, 565. *Measurements of* Ω *and* Λ *from 42 High-Redshift Supernovae*.

Planck Collaboration, Ade P. A. R., Arnaud M., Ashdown M., Aumont J., Baccigalupi C., Banday A. J., Barreiro R. B., Battaner E., Benabed K., Benoit-Lévy A., Bernard J.-P., Bersanelli M., Bielewicz P., Bond J. R., Borrill J., Bouchet F. R., Burigana C., Cardoso J.-F., Catalano A., Challinor A., Chamballu A., Chiang H. C., Christensen P. R., Clements D. L., Colombi S., Colombo L. P. L., Couchot F., Coulais A., Crill B. P., Curto A., Cuttaia F., Danese L., Davies R. D., Davis R. J., de Bernardis P., de Rosa A., de Zotti G., Delabrouille J., Désert F.-X., Dickinson C., Diego J. M., Dole H., Donzelli S., Doré O., Douspis M., Dupac X., Enßlin T. A., Eriksen H. K., Finelli F., Forni O., Frailis M., Fraisse A. A., Franceschi E., Galeotta S., Ganga K., Giard M., González-Nuevo J., Górski K. M., Gratton S., Gregorio A., Gruppuso A., Gudmundsson J. E., Hansen F. K., Hanson D., Harrison D. L., Henrot-Versillé S., Herranz D., Hildebrandt S. R., Hivon E., Hobson M., Holmes W. A., Hornstrup A., Hovest W., Huffenberger K. M., Jaffe A. H., Jaffe T. R., Jones W. C., Keihänen E., Keskitalo R., Knoche J., Kunz M., Kurki-Suonio H., Lagache G., Lähteenmäki A., Lamarre J.-M., Lasenby A., Lawrence C. R., Leonardi R., León-Tavares J., Lesgourgues J., Liguori M., Lilje P. B., Linden-Vørnle M., López-Caniego M., Lubin P. M., Macías-Pérez J. F., Maino D., Mandolesi N., Maris M., Martin P. G., Martínez-González E., Masi S., Matarrese S., Mazzotta P., Meinhold P. R., Melchiorri A., Mendes L., Mennella A., Migliaccio M., Mitra S., Miville-Deschênes M.-A., Moneti A., Montier L., Morgante G., Mortlock D., Moss A., Munshi D., Murphy J. A., Naselsky P., Nati F., Natoli P., Nørgaard-Nielsen H. U., Noviello F., Novikov D., Novikov I., Oxborrow C. A., Pagano L., Pajot F., Paoletti D., Partridge B., Pasian F., Patanchon G., Pearson D., Pearson T. J., Perdereau O., Perrotta F., Piacentini F., Piat M., Pierpaoli E., Pietrobon D., Plaszczynski S., Pointecouteau E., Polenta G., Ponthieu N., Popa L., Pratt G. W., Prunet S., Puget J.-L., Rachen J. P., Reinecke M., Remazeilles M., Renault C., Ricciardi S., Ristorcelli I., Rocha G., Roudier G., Rubiño-Martín J. A., Rusholme B., Sandri M., Scott D., Stolyarov V., Sudiwala R., Sutton D., Suur-Uski A.-S., Sygnet J.-F., Tauber J. A., Terenzi L., Toffolatti L., Tomasi M., Tristram M.,

Tucci M., Valenziano L., Valiviita J., Van Tent B., Vielva P., Villa F., Wade L. A., Wandelt B. D., Wehus I. K., White S. D. M., Yvon D., Zacchei A., Zonca A., 2014. A&A, **571**, A31. *Planck 2013 results. XXXI. Consistency of the Planck data*.

Planck Collaboration, Ade P. A. R., Aghanim N., Arnaud M., Ashdown M., Aumont J., Baccigalupi C., Banday A. J., Barreiro R. B., Bartlett J. G., et al., 2015. *ArXiv e-prints*. *Planck 2015 results. XIII. Cosmological parameters*.

Planck Collaboration, Adam R., Ade P. A. R., Aghanim N., Akrami Y., Alves M. I. R., Argüeso F., Arnaud M., Arroja F., Ashdown M., et al., 2016a. A&A, **594**, A1. *Planck 2015 results. I. Overview of products and scientific results*.

Planck Collaboration, Adam R., Aghanim N., Ashdown M., Aumont J., Baccigalupi C., Ballardini M., Banday A. J., Barreiro R. B., Bartolo N., Basak S., Battye R., Benabed K., Bernard J.-P., Bersanelli M., Bielewicz P., Bock J. J., Bonaldi A., Bonavera L., Bond J. R., Borrill J., Bouchet F. R., Bucher M., Burigana C., Calabrese E., Cardoso J.-F., Carron J., Chiang H. C., Colombo L. P. L., Combet C., Comis B., Coulais A., Crill B. P., Curto A., Cuttaia F., Davis R. J., de Bernardis P., de Rosa A., de Zotti G., Delabrouille J., Di Valentino E., Dickinson C., Diego J. M., Doré O., Douspis M., Ducout A., Dupac X., Elsner F., Enßlin T. A., Eriksen H. K., Falgarone E., Fantaye Y., Finelli F., Forastieri F., Frailis M., Fraisse A. A., Franceschi E., Frolov A., Galeotta S., Galli S., Ganga K., Génova-Santos R. T., Gerbino M., Ghosh T., González-Nuevo J., Górski K. M., Gruppuso A., Gudmundsson J. E., Hansen F. K., Helou G., Henrot-Versillé S., Herranz D., Hivon E., Huang Z., Ili S., Jaffe A. H., Jones W. C., Keihänen E., Keskitalo R., Kisner T. S., Knox L., Krachmalnicoff N., Kunz M., Kurki-Suonio H., Lagache G., Lähteenmäki A., Lamarre J.-M., Langer M., Lasenby A., Lattanzi M., Lawrence C. R., Le Jeune M., Levrier F., Lewis A., Liguori M., Lilje P. B., López-Caniego M., Ma Y.-Z., Macías-Pérez J. F., Maggio G., Mangilli A., Maris M., Martin P. G., Martínez-González E., Matarrese S., Mauri N., McEwen J. D., Meinhold P. R., Melchiorri A., Mennella A., Migliaccio M., Miville-Deschênes M.-A., Molinari D., Moneti A., Montier L., Morgante G., Moss A., Naselsky P., Natoli P., Oxborrow C. A., Pagano L., Paoletti D., Partridge B., Patanchon G., Patrizii L., Perdereau O., Perotto L., Pettorino V., Piacentini F., Plaszczynski S., Polastri L., Polenta G., Puget J.-L., Rachen J. P., Racine B., Reinecke M., Remazeilles M., Renzi

A., Rocha G., Rossetti M., Roudier G., Rubiño-Martín J. A., Ruiz-Granados B., Salvati L., Sandri M., Savelainen M., Scott D., Sirri G., Sunyaev R., Suur-Uski A.-S., Tauber J. A., Tenti M., Toffolatti L., Tomasi M., Tristram M., Trombetti T., Valiviita J., Van Tent F., Vielva P., Villa F., Vittorio N., Wandelt B. D., Wehus I. K., White M., Zacchei A., Zonca A., 2016b. *ArXiv e-prints*. *Planck intermediate results. XLVII. Planck constraints on reionization history*.

Pratt C. T., Stocke J. T., Keeney B. A., Danforth C. W., 2017. *ArXiv e-prints*. *The Spread of Metals into the Low-Redshift Intergalactic Medium*.

Pritchard J. R., Loeb A., 2012. *Reports on Progress in Physics*, **75(8)**, 086901. *21 cm cosmology in the 21st century*.

Pritchard J. R., Loeb A., Wyithe J. S. B., 2010. MNRAS, **408**, 57. *Constraining reionization using 21-cm observations in combination with CMB and Lyα forest data*.

Puchwein E., Springel V., 2013. MNRAS, **428**, 2966. *Shaping the galaxy stellar mass function with supernova- and AGN-driven winds*.

Puchwein E., Pfrommer C., Springel V., Broderick A. E., Chang P., 2012. MNRAS, **423**, 149. *The Lyman α forest in a blazar-heated Universe*.

Puchwein E., Bolton J. S., Haehnelt M. G., Madau P., Becker G. D., Haardt F., 2015. MNRAS, **450**, 4081. *The photoheating of the intergalactic medium in synthesis models of the UV background*.

Rahmati A., Pawlik A. H., Raicevic M., Schaye J., 2013. MNRAS, **430**, 2427. *On the evolution of the H I column density distribution in cosmological simulations*.

Raskutti S., Bolton J. S., Wyithe J. S. B., Becker G. D., 2012. MNRAS, **421**, 1969. *Thermal constraints on the reionization of hydrogen by Population II stellar sources*.

Rauch M., Miralda-Escudé J., Sargent W. L. W., Barlow T. A., Weinberg D. H., Hernquist L., Katz N., Cen R., Ostriker J. P., 1997. ApJ, **489**, 7. *The Opacity of the Lyα Forest and Implications for Ω_b and the Ionizing Background*.

Reed S. L., McMahon R. G., Banerji M., Becker G. D., Gonzalez-Solares E., Martini P., Ostrovski F., Rauch M., Abbott T., Abdalla F. B., Allam S., Benoit-Levy A., Bertin

E., Buckley-Geer E., Burke D., Carnero Rosell A., da Costa L. N., D'Andrea C., DePoy D. L., Desai S., Diehl H. T., Doel P., Cunha C. E., Estrada J., Evrard A. E., Fausti Neto A., Finley D. A., Fosalba P., Frieman J., Gruen D., Honscheid K., James D., Kent S., Kuehn K., Kuropatkin N., Lahav O., Maia M. A. G., Makler M., Marshall J., Merritt K., Miquel R., Mohr J., Nord B., Ogando R., Plazas A., Romer K., Roodman A., Rykoff E., Sako M., Sanchez E., Santiago B., Schubnell M., Sevilla I., Smith C., Soares-Santos M., Suchyta E., Swanson M. E. C., Tarle G., Thomas D., Tucker D., Walker A., Wechsler R. H., 2015. MNRAS, **454**, 3952. *DES J0454-4448: discovery of the first luminous z ¿ 6 quasar from the Dark Energy Survey*.

Rees M. J., 2000. Phys. Rep., **333**, 203. *'First light' in the universe: what ended the 'dark age'?*

Richter P., Fang T., Bryan G. L., 2006. A&A, **451**, 767. *Simulations of thermally broadened H I Ly α absorption arising in the warm-hot intergalactic medium*.

Ricotti M., Gnedin N. Y., Shull J. M., 2000. ApJ, **534**, 41. *The Evolution of the Effective Equation of State of the Intergalactic Medium*.

Riess A. G., Strolger L.-G., Tonry J., Casertano S., Ferguson H. C., Mobasher B., Challis P., Filippenko A. V., Jha S., Li W., Chornock R., Kirshner R. P., Leibundgut B., Dickinson M., Livio M., Giavalisco M., Steidel C. C., Benítez T., Tsvetanov Z., 2004. ApJ, **607**, 665. *Type Ia Supernova Discoveries at z ¿ 1 from the Hubble Space Telescope: Evidence for Past Deceleration and Constraints on Dark Energy Evolution*.

Robertson B. E., Ellis R. S., Furlanetto S. R., Dunlop J. S., 2015. ApJ, **802**, L19. *Cosmic Reionization and Early Star-forming Galaxies: A Joint Analysis of New Constraints from Planck and the Hubble Space Telescope*.

Rollinde E., Theuns T., Schaye J., Pâris I., Petitjean P., 2013. MNRAS, **428**, 540. *Sample variance and Lyman α forest transmission statistics*.

Rorai A., Hennawi J. F., White M., 2013. ApJ, **775**, 81. *A New Method to Directly Measure the Jeans Scale of the Intergalactic Medium Using Close Quasar Pairs*.

Rosdahl J., Blaizot J., Aubert D., Stranex T., Teyssier R., 2013. MNRAS, **436**, 2188. *RAMSES-RT: radiation hydrodynamics in the cosmological context*.

Rudie G. C., Steidel C. C., Pettini M., 2012. ApJ, **757**, L30. *The Temperature-Density Relation in the Intergalactic Medium at Redshift* $< z >= 2.4$.

Savaglio S., Ferguson H. C., Brown T. M., Espey B. R., Sahu K. C., Baum S. A., Carollo C. M., Kaiser M. E., Stiavelli M., Williams R. E., Wilson J., 1999. ApJ, **515**, L5. *The Lyα Forest of the Quasar in the Hubble Deep Field South*.

Schaye J., Theuns T., Leonard A., Efstathiou G., 1999. MNRAS, **310**, 57. *Measuring the equation of state of the intergalactic medium*.

Schaye J., Theuns T., Rauch M., Efstathiou G., Sargent W. L. W., 2000. MNRAS, **318**, 817. *The thermal history of the intergalactic medium**.

Schaye J., Dalla Vecchia C., Booth C. M., Wiersma R. P. C., Theuns T., Haas M. R., Bertone S., Duffy A. R., McCarthy I. G., van de Voort F., 2010. MNRAS, **402**, 1536. *The physics driving the cosmic star formation history*.

Schaye J., Crain R. A., Bower R. G., Furlong M., Schaller M., Theuns T., Dalla Vecchia C., Frenk C. S., McCarthy I. G., Helly J. C., Jenkins A., Rosas-Guevara Y. M., White S. D. M., Baes M., Booth C. M., Camps P., Navarro J. F., Qu Y., Rahmati A., Sawala T., Thomas P. A., Trayford J., 2015. MNRAS, **446**, 521. *The EAGLE project: simulating the evolution and assembly of galaxies and their environments*.

Schaye J., 2001. ApJ, **559**, 507. *Model-independent Insights into the Nature of the Lyα Forest and the Distribution of Matter in the Universe*.

Schmidt M., 1965. ApJ, **141**, 1295. *Large Redshifts of Five Quasi-Stellar Sources.*

Scott J., Bechtold J., Morita M., Dobrzycki A., Kulkarni V. P., 2002. ApJ, **571**, 665. *A Uniform Analysis of the Lyα Forest at $z = 0 - 5$. V. The Extragalactic Ionizing Background at Low Redshift*.

Seljak U., Makarov A., McDonald P., Anderson S. F., Bahcall N. A., Brinkmann J., Burles S., Cen R., Doi M., Gunn J. E., Ivezić Ž., Kent S., Loveday J., Lupton R. H., Munn J. A., Nichol R. C., Ostriker J. P., Schlegel D. J., Schneider D. P., Tegmark M.,

Berk D. E., Weinberg D. H., York D. G., 2005. Phys. Rev. D, **71(10)**, 103515. *Cosmological parameter analysis including SDSS Lyα forest and galaxy bias: Constraints on the primordial spectrum of fluctuations, neutrino mass, and dark energy*.

Sembach K. R., Tripp T. M., Savage B. D., Richter P., 2004. ApJS, **155**, 351. *Physical Properties and Baryonic Content of Low-Redshift Intergalactic Lyα and O VI Absorption Line Systems: The PG 1116+215 Sight Line*.

Shull J. M., Danforth C. W., Tilton E. M., 2014. ApJ, **796**, 49. *Tracing the Cosmic Metal Evolution in the Low-redshift Intergalactic Medium*.

Shull J. M., Moloney J., Danforth C. W., Tilton E. M., 2015. ApJ, **811**, 3. *The Metagalactic Ionizing Background: A Crisis in UV Photon Production or Incorrect Galaxy Escape Fractions?*

Shull J. M., Smith B. D., Danforth C. W., 2012. ApJ, **759**, 23. *The Baryon Census in a Multiphase Intergalactic Medium: 30% of the Baryons May Still be Missing*.

Sijacki D., Springel V., Di Matteo T., Hernquist L., 2007. MNRAS, **380**, 877. *A unified model for AGN feedback in cosmological simulations of structure formation*.

Smoot G. F., Bennett C. L., Kogut A., Wright E. L., Aymon J., Boggess N. W., Cheng E. S., de Amici G., Gulkis S., Hauser M. G., Hinshaw G., Jackson P. D., Janssen M., Kaita E., Kelsall T., Keegstra P., Lineweaver C., Loewenstein K., Lubin P., Mather J., Meyer S. S., Moseley S. H., Murdock T., Rokke L., Silverberg R. F., Tenorio L., Weiss R., Wilkinson D. T., 1992. ApJ, **396**, L1. *Structure in the COBE differential microwave radiometer first-year maps*.

Songaila A., 2004. AJ, **127**, 2598. *The Evolution of the Intergalactic Medium Transmission to Redshift 6*.

Springel V., Hernquist L., 2003. MNRAS, **339**, 289. *Cosmological smoothed particle hydrodynamics simulations: a hybrid multiphase model for star formation*.

Springel V., White S. D. M., Jenkins A., Frenk C. S., Yoshida N., Gao L., Navarro J., Thacker R., Croton D., Helly J., Peacock J. A., Cole S., Thomas P., Couchman H., Evrard A., Colberg J., Pearce F., 2005a. Nature, **435**, 629. *Simulations of the formation, evolution and clustering of galaxies and quasars*.

Springel V., White S. D. M., Jenkins A., Frenk C. S., Yoshida N., Gao L., Navarro J., Thacker R., Croton D., Helly J., Peacock J. A., Cole S., Thomas P., Couchman H., Evrard A., Colberg J., Pearce F., 2005b. Nature, **435**, 629. *Simulations of the formation, evolution and clustering of galaxies and quasars*.

Springel V., Frenk C. S., White S. D. M., 2006. Nature, **440**, 1137. *The large-scale structure of the Universe*.

Springel V., 2005. MNRAS, **364**, 1105. *The cosmological simulation code GADGET-2*.

Tegmark M., Strauss M. A., Blanton M. R., Abazajian K., Dodelson S., Sandvik H., Wang X., Weinberg D. H., Zehavi I., Bahcall N. A., Hoyle F., Schlegel D., Scoccimarro R., Vogeley M. S., Berlind A., Budavari T., Connolly A., Eisenstein D. J., Finkbeiner D., Frieman J. A., Gunn J. E., Hui L., Jain B., Johnston D., Kent S., Lin H., Nakajima R., Nichol R. C., Ostriker J. P., Pope A., Scranton R., Seljak U., Sheth R. K., Stebbins A., Szalay A. S., Szapudi I., Xu Y., Annis J., Brinkmann J., Burles S., Castander F. J., Csabai I., Loveday J., Doi M., Fukugita M., Gillespie B., Hennessy G., Hogg D. W., Ivezić Ž., Knapp G. R., Lamb D. Q., Lee B. C., Lupton R. H., McKay T. A., Kunszt P., Munn J. A., O'Connell L., Peoples J., Pier J. R., Richmond M., Rockosi C., Schneider D. P., Stoughton C., Tucker D. L., vanden Berk D. E., Yanny B., York D. G., 2004. Phys. Rev. D, **69(10)**, 103501. *Cosmological parameters from SDSS and WMAP*.

Tepper-García T., Richter P., Schaye J., Booth C. M., Dalla Vecchia C., Theuns T., 2012. MNRAS, **425**, 1640. *Absorption signatures of warm-hot gas at low redshift: broad H I Lyα absorbers*.

Tepper-García T., 2006. MNRAS, **369**, 2025. *Voigt profile fitting to quasar absorption lines: an analytic approximation to the Voigt-Hjerting function*.

Theuns T., Zaroubi S., 2000. MNRAS, **317**, 989. *A wavelet analysis of the spectra of quasi-stellar objects*.

Theuns T., Leonard A., Efstathiou G., Pearce F. R., Thomas P. A., 1998. MNRAS, **301**, 478. *P^3M-SPH simulations of the Lyalpha forest*.

Theuns T., Viel M., Kay S., Schaye J., Carswell R. F., Tzanavaris P., 2002a. ApJ, **578**, L5. *Galactic Winds in the Intergalactic Medium*.

Theuns T., Viel M., Kay S., Schaye J., Carswell R. F., Tzanavaris P., 2002b. ApJ, **578**, L5. *Galactic Winds in the Intergalactic Medium*.

Theuns T., Leonard A., Efstathiou G., 1998. MNRAS, **297**, L49. *The low-redshift evolution of the Lyman-alpha forest*.

Theuns T., Schaye J., Haehnelt M. G., 2000. MNRAS, **315**, 600. *Broadening of QSO Lyα forest absorbers*.

Thronson H. A., Bolcar M. R., Clampin M., Crooke J. A., Redding D., Rioux N., Stahl H. P., 2016. *An Engineering Design Reference Mission for a Future Large-Aperture UVOIR Space Observatory*, In: *American Astronomical Society Meeting Abstracts*, 147.23.

Tilton E. M., Danforth C. W., Shull J. M., Ross T. L., 2012. ApJ, **759**, 112. *The Low-redshift Intergalactic Medium as Seen in Archival Legacy HST/STIS and FUSE Data*.

Trac H. Y., Gnedin N. Y., 2011. *Advanced Science Letters*, **4**, 228. *Computer Simulations of Cosmic Reionization*.

Trac H., Cen R., Loeb A., 2008. ApJ, **689**, L81. *Imprint of Inhomogeneous Hydrogen Reionization on the Temperature Distribution of the Intergalactic Medium*.

Trenti M., Stiavelli M., 2009. ApJ, **694**, 879. *Formation Rates of Population III Stars and Chemical Enrichment of Halos during the Reionization Era*.

Tytler D., Paschos P., Kirkman D., Norman M. L., Jena T., 2009. MNRAS, **393**, 723. *The effect of large-scale power on simulated spectra of the Lyα forest*.

Upton Sanderbeck P. R., D'Aloisio A., McQuinn M. J., 2016. MNRAS, **460**, 1885. *Models of the thermal evolution of the intergalactic medium after reionization*.

van Uitert E., Joachimi B., Joudaki S., Heymans C., Köhlinger F., Asgari M., Blake C., Choi A., Erben T., Farrow D. J., Harnois-Déraps J., Hildebrandt H., Hoekstra H.,

Kitching T. D., Klaes D., Kuijken K., Merten J., Miller L., Nakajima R., Schneider P., Valentijn E., Viola M., 2017. *ArXiv e-prints*. *KiDS+GAMA: Cosmology constraints from a joint analysis of cosmic shear, galaxy-galaxy lensing and angular clustering*.

Venemans B. P., Findlay J. R., Sutherland W. J., De Rosa G., McMahon R. G., Simcoe R., González-Solares E. A., Kuijken K., Lewis J. R., 2013. ApJ, **779**, 24. *Discovery of Three z ¿ 6.5 Quasars in the VISTA Kilo-Degree Infrared Galaxy (VIKING) Survey*.

Venemans B. P., Verdoes Kleijn G. A., Mwebaze J., Valentijn E. A., Bañados E., Decarli R., de Jong J. T. A., Findlay J. R., Kuijken K. H., Barbera F. L., McFarland J. P., McMahon R. G., Napolitano N., Sikkema G., Sutherland W. J., 2015. MNRAS, **453**, 2259. *First discoveries of z 6 quasars with the Kilo-Degree Survey and VISTA Kilo-Degree Infrared Galaxy survey*.

Verner D. A., Ferland G. J., 1996. ApJS, **103**, 467. *Atomic Data for Astrophysics. I. Radiative Recombination Rates for H-like, He-like, Li-like, and Na-like Ions over a Broad Range of Temperature*.

Viel M., Bolton J. S., Haehnelt M. G., 2009. MNRAS, **399**, L39. *Cosmological and astrophysical constraints from the Lyman α forest flux probability distribution function*.

Viel M., Matarrese S., Mo H. J., Theuns T., Haehnelt M. G., 2002. MNRAS, **336**, 685. *Modelling the IGM and the Ly α forest at high redshift from the dark matter distribution*.

Viel M., Becker G. D., Bolton J. S., Haehnelt M. G., 2013a. Phys. Rev. D, **88(4)**, 043502. *Warm dark matter as a solution to the small scale crisis: New constraints from high redshift Lyman-α forest data*.

Viel M., Becker G. D., Bolton J. S., Haehnelt M. G., 2013b. Phys. Rev. D, **88(4)**, 043502. *Warm dark matter as a solution to the small scale crisis: New constraints from high redshift Lyman-α forest data*.

Viel M., Haehnelt M. G., Bolton J. S., Kim T.-S., Puchwein E., Nasir F., Wakker B. P., 2017a. MNRAS, **467**, L86. *Diagnosing galactic feedback with line broadening in the low-redshift Lyα forest*.

Viel M., Haehnelt M. G., Bolton J. S., Kim T.-S., Puchwein E., Nasir F., Wakker B. P., 2017b. MNRAS, **467**, L86. *Diagnosing galactic feedback with line broadening in the low-redshift Lyα forest*.

Viel M., Haehnelt M. G., Springel V., 2004a. MNRAS, **354**, 684. *Inferring the dark matter power spectrum from the Lyman α forest in high-resolution QSO absorption spectra*.

Viel M., Haehnelt M. G., Springel V., 2004b. MNRAS, **354**, 684. *Inferring the dark matter power spectrum from the Lyman α forest in high-resolution QSO absorption spectra*.

Viel M., Schaye J., Booth C. M., 2013a. MNRAS, **429**, 1734. *The impact of feedback from galaxy formation on the Lyman α transmitted flux*.

Viel M., Schaye J., Booth C. M., 2013b. MNRAS, **429**, 1734. *The impact of feedback from galaxy formation on the Lyman α transmitted flux*.

Vogelsberger M., Genel S., Springel V., Torrey P., Sijacki D., Xu D., Snyder G., Nelson D., Hernquist L., 2014a. MNRAS, **444**, 1518. *Introducing the Illustris Project: simulating the coevolution of dark and visible matter in the Universe*.

Vogelsberger M., Genel S., Springel V., Torrey P., Sijacki D., Xu D., Snyder G., Nelson D., Hernquist L., 2014b. MNRAS, **444**, 1518. *Introducing the Illustris Project: simulating the coevolution of dark and visible matter in the Universe*.

Wakker B. P., Hernandez A. K., French D. M., Kim T.-S., Oppenheimer B. D., Savage B. D., 2015. ApJ, **814**, 40. *Nearby Galaxy Filaments and the Ly-alpha Forest: Confronting Simulations and the UV Background with Observations*.

Weinberg D. H., Miralda-Escudé J., Hernquist L., Katz N., 1997. ApJ, **490**, 564. *A Lower Bound on the Cosmic Baryon Density*.

Weinberg D. H., Davé R., Katz N., Kollmeier J. A., 2003. *The Lyman-α Forest as a Cosmological Tool*, In: *The Emergence of Cosmic Structure*, p. 157, eds Holt S. H., Reynolds C. S.

Werk J. K., Prochaska J. X., Tumlinson J., Peeples M. S., Tripp T. M., Fox A. J., Lehner N., Thom C., O'Meara J. M., Ford A. B., Bordoloi R., Katz N., Tejos N., Oppenheimer B. D., Davé R., Weinberg D. H., 2014. ApJ, **792**, 8. *The COS-Halos Survey: Physical Conditions and Baryonic Mass in the Low-redshift Circumgalactic Medium*.

Weymann R. J., Jannuzi B. T., Lu L., Bahcall J. N., Bergeron J., Boksenberg A., Hartig G. F., Kirhakos S., Sargent W. L. W., Savage B. D., Schneider D. P., Turnshek D. A., Wolfe A. M., 1998. ApJ, **506**, 1. *The Hubble Space Telescope Quasar Absorption Line Key Project. XIV. The Evolution of Lyα Absorption Lines in the Redshift Interval $z = 0 - 1.5$.*

White S. D. M., Rees M. J., 1978. MNRAS, **183**, 341. *Core condensation in heavy halos - A two-stage theory for galaxy formation and clustering*.

Williger G. M., Heap S. R., Weymann R. J., Davé R., Ellingson E., Carswell R. F., Tripp T. M., Jenkins E. B., 2006. ApJ, **636**, 631. *The Low-Redshift Lyα Forest toward PKS 0405-123*.

Williger G. M., Carswell R. F., Weymann R. J., Jenkins E. B., Sembach K. R., Tripp T. M., Davé R., Haberzettl L., Heap S. R., 2010. MNRAS, **405**, 1736. *The low-redshift Lyα forest towards 3C 273*.

Willott C. J., Delorme P., Reylé C., Albert L., Bergeron J., Crampton D., Delfosse X., Forveille T., Hutchings J. B., McLure R. J., Omont A., Schade D., 2010. AJ, **139**, 906. *The Canada-France High-z Quasar Survey: Nine New Quasars and the Luminosity Function at Redshift 6*.

Worseck G., Prochaska J. X., O'Meara J. M., Becker G. D., Ellison S. L., Lopez S., Meiksin A., Ménard B., Murphy M. T., Fumagalli M., 2014. MNRAS, **445**, 1745. *The Giant Gemini GMOS survey of z_{em} ¿ 4.4 quasars - I. Measuring the mean free path across cosmic time*.

Wyithe J. S. B., Loeb A., 2004. Nature, **432**, 194. *A characteristic size of $\sim$ 10Mpc for the ionized bubbles at the end of cosmic reionization*.

Yan H., Conselice C., Windhorst R., Cohen S., Alpaslan M., Zitrin A., Broadhurst T., Frye B., Driver S., Robotham A., Hopkins A., Wyithe S., Jansen R., Hathi N., Mechtley M., Ryan R., Rutkowski M., Finkelstein S., Koekemoer A., 2016. *Deep IRAC Imaging Lensing Galaxy Clusters for JWST 'First Light' Search*, Spitzer Proposal.

Zaldarriaga M., Hui L., Tegmark M., 2001. ApJ, **557**, 519. *Constraints from the Lyα Forest Power Spectrum*.

Zaldarriaga M., 2002. ApJ, **564**, 153. *Searching for Fluctuations in the Intergalactic Medium Temperature Using the Lyα Forest*.

Zaroubi S., Viel M., Nusser A., Haehnelt M., Kim T.-S., 2006. MNRAS, **369**, 734. *The matter power spectrum from the Lyα forest: an optical depth estimate*.

Zel'dovich Y. B., 1970. A&A, **5**, 84. *Gravitational instability: An approximate theory for large density perturbations.*

Zhang Y., Meiksin A., Anninos P., Norman M. L., 1998. ApJ, **495**, 63. *Physical Properties of the Lyα Forest in a Cold Dark Matter Cosmology*.